

**A fundamental study on materials for  
Li-ion batteries**



The research described in this thesis was performed in the Department of Neutron Scattering and Mössbauer spectroscopy of the Interfacultair Reactor Instituut, Delft University of Technology, Mekelweg 15, 2629 JB Delft, The Netherlands.

# A fundamental study on materials for Li-ion batteries

PROEFSCHRIFT

ter verkrijging van de graad van doctor  
aan de Technische Universiteit Delft,  
op gezag van de Rector Magnificus prof. ir. K.F. Wakker,  
voorzitter van het College voor Promoties  
in het openbaar te verdedigen op maandag 12 november 2001 om 10.30 uur

door

Vincent Wilhelmus Johannes VERHOEVEN

natuurkundig ingenieur  
geboren te Breda

Dit proefschrift is goedgekeurd door de promotoren:

Prof. dr. I.M. de Schepper

Prof. dr. J. Schoonman

Samenstelling promotiecommissie:

Rector Magnificus                      voorzitter

Prof. dr. I.M. de Schepper      Technische Universiteit Delft, promotor

Prof. dr. J. Schoonman            Technische Universiteit Delft, promotor

Prof. dr. G.J. Kearley            Technische Universiteit Delft

Prof. dr. S.W. de Leeuw        Technische Universiteit Delft

Dr. F.M. Mulder                  Technische Universiteit Delft

Dr. P.C.M. Gubbens              Technische Universiteit Delft

Prof. dr. A.P.M. Kentgens      Katholieke Universiteit Nijmegen

*Published and distributed by:* DUP Science

DUP Science is an imprint of

Delft University Press

P.O. Box 98

2600 MG Delft

The Netherlands

Telephone: +31 15 27 85 678

Fax: +31 15 27 85 706

E-mail: DUP@Library.TUdelft.nl

ISBN 90-407-2244-7

Keywords: Li-ion batteries, Neutron scattering, NMR

Copyright ©2001 by V.W.J. Verhoeven

All rights reserved. No part of the material protected by this copyright notice may be reproduced or utilized in any form or by any means, electronic or mechanical, including photocopying, recording or by any information storage and retrieval system, without permission from the publisher: Delft University Press.

Printed in the Netherlands

# Contents

<b>1</b>	<b>Introduction</b>	<b>1</b>
<b>2</b>	<b>Theory of Neutron Diffraction</b>	<b>7</b>
2.1	Definitions . . . . .	7
2.2	Elastic scattering by a single nucleus . . . . .	8
2.3	Inelastic scattering by a collection of atoms . . . . .	11
2.4	Nuclear scattering . . . . .	12
2.5	Coherent nuclear scattering by a crystal . . . . .	13
2.6	Coherent scattering by a powder . . . . .	15
2.7	Magnetic Diffraction . . . . .	17
2.8	Neutron powder diffractometers . . . . .	18
<b>3</b>	<b>Neutron Diffraction on <math>\text{BPO}_4 + z\% \text{Li}_2\text{O}</math></b>	<b>21</b>
3.1	Li-doped $\text{BPO}_4$ . . . . .	21
3.1.1	Sample . . . . .	22
3.2	POLARIS . . . . .	23
3.3	Sample container . . . . .	23
3.4	Absorption correction . . . . .	24
3.5	Rietveld refinement . . . . .	24
3.6	Conclusions . . . . .	27
<b>4</b>	<b>Neutron Diffraction on <math>\text{Li}_x\text{Mn}_2\text{O}_4</math></b>	<b>29</b>
4.1	$\text{Li}_x\text{Mn}_2\text{O}_4$ . . . . .	29
4.1.1	Jahn-Teller effect . . . . .	29
4.1.2	Recyclability . . . . .	31
4.1.3	Sample . . . . .	31
4.2	HB5 . . . . .	32
4.3	Sample environment . . . . .	32
4.4	Absorption correction . . . . .	33
4.5	$\text{Li}[\text{Mn}_{1.96}\text{Li}_{0.04}]\text{O}_4$ . . . . .	33
4.6	$\text{Li}_{0.2}[\text{Mn}_{1.96}\text{Li}_{0.04}]\text{O}_4$ . . . . .	34

---

4.7	Conclusions . . . . .	39
<b>5</b>	<b>One Dimensional NMR</b>	<b>41</b>
5.1	theory . . . . .	41
5.1.1	Relaxation . . . . .	43
5.1.2	Pulses . . . . .	48
5.1.3	Chemical Shift . . . . .	49
5.1.4	Direct dipole-dipole interaction and Magic Angle Spin- ning (MAS) NMR . . . . .	50
5.1.5	Quadrupole interaction . . . . .	51
5.1.6	Line width . . . . .	53
5.2	Experiment . . . . .	53
5.2.1	Data analysis . . . . .	54
5.2.2	$\text{Li}_x[\text{Mn}_{1.95}\text{Li}_{0.05}]\text{O}_4$ . . . . .	54
5.3	Results and Discussion . . . . .	60
<b>6</b>	<b>Quasi Elastic Neutron Scattering</b>	<b>63</b>
6.1	Theory . . . . .	63
6.1.1	Intermediate and scattering functions . . . . .	65
6.1.2	The harmonic oscillator . . . . .	66
6.1.3	Magnetic scattering . . . . .	71
6.2	Magnetic properties . . . . .	73
6.2.1	Anti-ferromagnetic interaction . . . . .	73
6.2.2	Magnetic frustration . . . . .	74
6.3	Experiments . . . . .	76
6.3.1	RKSII . . . . .	76
6.3.2	IN6 . . . . .	78
6.3.3	Data processing . . . . .	80
6.4	Results and Discussion . . . . .	81
6.4.1	Corrected data . . . . .	81
6.4.2	Fit procedure . . . . .	82
6.4.3	Results . . . . .	91
6.4.4	Discussion . . . . .	98
6.4.5	Time-scales of magnetic excitations . . . . .	100
6.5	Conclusions . . . . .	102
<b>7</b>	<b>Two Dimensional NMR</b>	<b>103</b>
7.1	Theory . . . . .	103
7.1.1	Pulse sequence . . . . .	103
7.2	Experiments . . . . .	107
7.2.1	Data analysis . . . . .	108

---

7.2.2	Temperature calibration . . . . .	108
7.3	Results and Discussion . . . . .	110
7.3.1	Crosspeaks . . . . .	110
7.3.2	Jump model . . . . .	111
7.3.3	Activation energy . . . . .	117
7.3.4	Self diffusion coefficient . . . . .	119
7.4	Comparison with electron diffraction and QENS . . . . .	120
7.5	Conclusions . . . . .	121
<b>8</b>	<b>General Conclusions</b>	<b>123</b>
	<b>Summary</b>	<b>129</b>
	<b>Samenvatting</b>	<b>131</b>
	<b>Dankwoord</b>	<b>133</b>
	<b>Curriculum Vitae</b>	<b>135</b>
	<b>List of Publications</b>	<b>137</b>





# Chapter 1

## Introduction

The utilization of renewable energy sources is attracting increasing attention on a global scale. The effects of the increase in the consumption of energy, generated from fossil fuels, caused by the growing world population and the global economic growth, is having a constant increasing importance on the world wide political agenda since it may accelerate global warming and cause serious damage to the worldwide environment. Cleaner energies including renewables are thus targeted fields of research and development for securing our energy supply and protecting the environment.

In April 1997 the program "Decentralized Production and Storage for Large-Scale Application of Renewable Energy" of the Delft Interfaculty Research Center (DIOC) was launched. In this program various groups from several Faculties of the Delft University of Technology studied the feasibility of large scale application of renewable energy. The program was divided into three subjects, i.e. production, storage and distribution of renewable energy. In this thesis we will focus on the subject of energy storage. The work was performed in the period of July 1997 till July 2001. The goal of the project was to obtain fundamental knowledge (e.g. crystal structure, lithium dynamics) of materials usable in an all solid-state Li-ion battery. Hereby we focused on two materials, the ceramic electrolyte  $\text{BPO}_4 + z\% \text{Li}_2\text{O}$  and the cathode  $\text{LiMn}_2\text{O}_4$ .

The energy produced by a renewable source will not only be produced at moments that it is needed (as is the case with the conventionally produced energy) but also at moments that it is barely needed. Therefore one will have to store this energy to make it available at all times. Energy can be stored in many ways, e.g. converting water into hydrogen and oxygen and back again when the energy is needed. One of the most convenient and easiest ways is to store electrical energy in rechargeable batteries, e.g. lithium-ion batteries. Favorable characteristics of lithium-ion batteries include a high

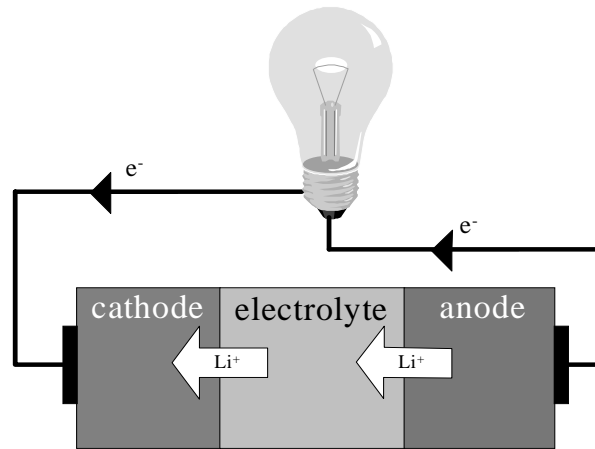


Figure 1.1: A schematic view of a Li-ion battery.

energy density, a high voltage and a low weight. Figure 1.1 shows a schematic view of a lithium-ion battery. The battery consists of 2 electrodes, cathode and anode, and an electrolyte. When a battery is being used (discharged), Li-ions are moving out of the anode and into the cathode. The driving force is the difference in the electro-chemical potential experienced by the lithium ion in the anode and the cathode material. Since the electrolyte is an ion-conductor but not an electronic-conductor the electrons are forced to travel from anode to cathode externally. Finally the electrons and  $\text{Li}^+$ -ions meet again in the cathode. Charging the battery is the reverse of this procedure. The driving force results from an applied voltage that more than compensates the difference in electro-chemical potential between anode and cathode.

The characteristics of several existing batteries systems are given in table 1.1 [1], figure 1.2 [2] and figure 1.3 [3]. As one may conclude from table 1.1, figure 1.2 and figure 1.3, Li-ion batteries are very promising compared to other existing battery systems when comparing energy densities as well as the presents of heavy metals. Furthermore, the expected improvements and price reduction in the near future are promising (figure 1.4) according to [3]. We note that Li-based batteries are relatively expensive at present, see figure 1.4. However, using cheaper materials, further development and mass production will reduce the price. This price reduction will also stimulate the use of lithium-ion batteries in electric cars, notebooks, cellular phones and all other sorts of electronic equipment.

In the last few years the ceramic compound  $\text{LiMn}_2\text{O}_4$  has gained a lot of interest since it is a very promising candidate as cathode material in advanced Li-ion batteries. The material is light, has a high energy capacity per unit

Table 1.1: Characteristics of several rechargeable battery systems [1]. First values reflect the 1995 specifications, second values are the expected specifications.

	nominal voltage (V)	energy density (Wh/kg)	energy density (Wh/l)	power density (W/kg)	temperature (°C)
lead-acid	2.0	15-35	60-90	150-300	-20-50
NiCd	1.2	27-55	45-110	260	-40-60
NiMH	1.2	35-50	80-175	180-220	-10-40
Li-ion	3.6	60-90	155-200	200-300	-20-45
ZnBr	1.6	65-75	60-70	60	25-50
Na/NiCl <sub>2</sub>	2.4	88-98	95-113	70-130	230-280
NaS	2.0	90-110	135-155	110-130	310-350

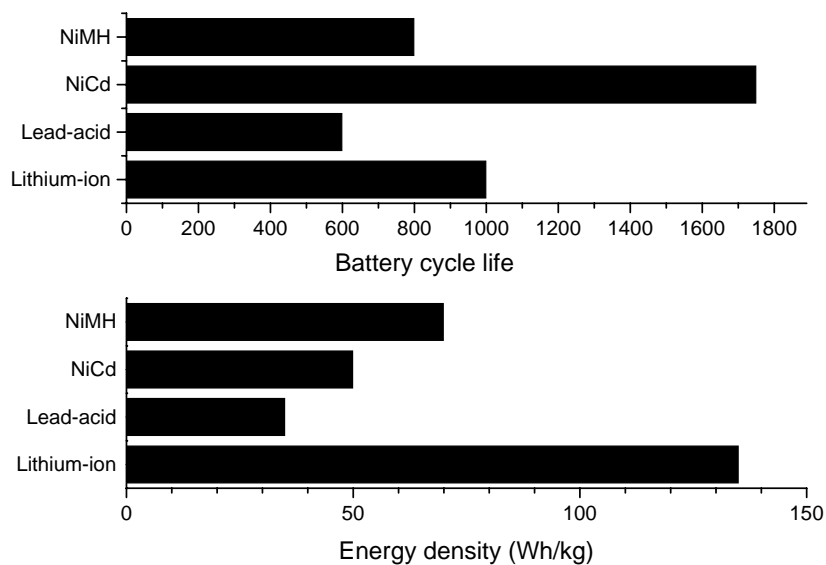


Figure 1.2: Energy density and cycle life of various rechargeable battery systems (1999) [2]. The cycle life is defined as that number of cycles at which the battery capacity is reduced to 80 % of its original value.

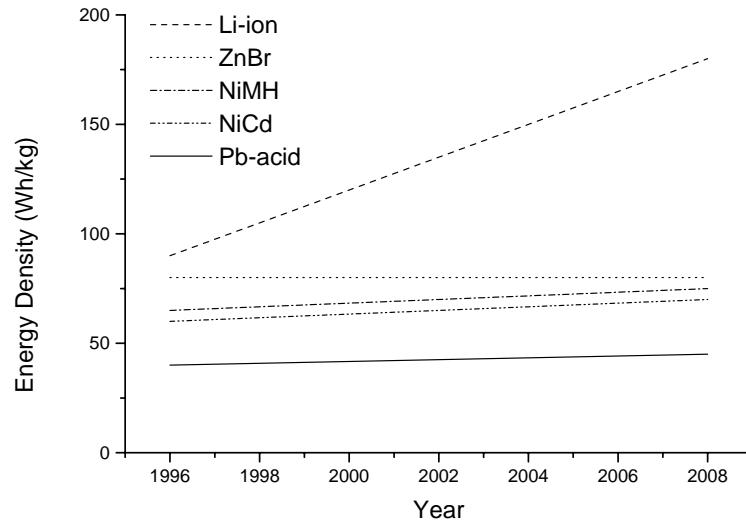


Figure 1.3: Expected development of energy density for various battery types [3].

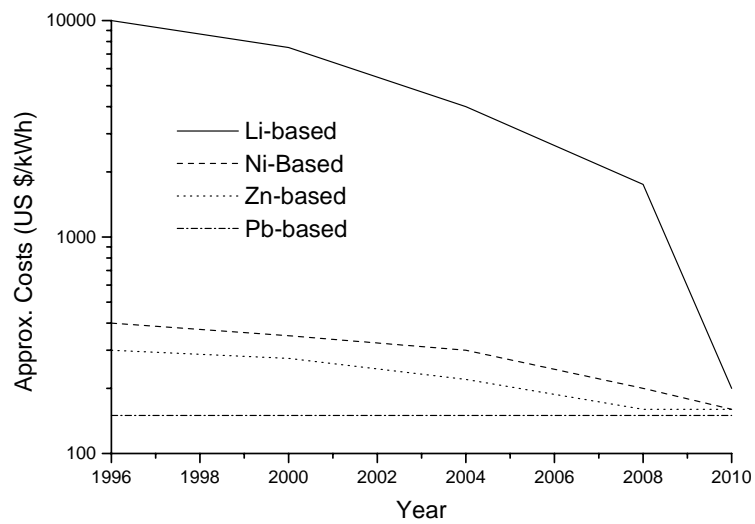


Figure 1.4: Estimated costs expectations of various rechargeable batteries [3].

weight, contains no heavy metals, is not poisonous and it is cheap. In the Li-ion batteries, which are commercially available at the moment, mainly  $\text{LiCo}_2\text{O}_4$  is being used as a cathode. However cobalt is poisonous and quite expensive. Therefore, it is very well possible that  $\text{LiMn}_2\text{O}_4$  is going to replace  $\text{LiCo}_2\text{O}_4$  in the near future.

The majority of studies on Li-ion batteries deal with battery systems based on intercalation compounds for both anode and cathode separated by a liquid or polymer-based electrolyte. The instability of the electrolytes, caused by high battery voltages and/or temperatures exceeding  $50^\circ\text{C}$ , results in capacity fading and reduction of the cycle life. Decomposition of the electrolyte often results in gas evolution leading to irreversible processes and high internal pressures which may damage the battery and cause safety problems. [4, 5]. The poor safety properties of Li-ion batteries caused by the instability of the electrolyte, represent a key problem to large-scale introduction.

Problems concerning the instability of the electrolyte can be solved by using a ceramic electrolyte, because the stability of the electrolyte versus the electrodes is higher, leading to a longer cycle life. Furthermore, the decomposition potential of ceramic electrolytes is higher, reducing the risk on pressure build-up in the battery. Drawbacks of ceramic electrolytes are their relatively low ionic conductivity [6] and the poor interfacial contacts between the battery components. To overcome these poor interfacial contacts the whole battery can be compacted by Magnetic Pulse Compaction resulting in a drastically decreased internal resistance of the battery [7]. We studied lithium-doped  $\text{BPO}_4$  as a ceramic electrolyte, since it is easy and cheap to synthesize and it does not contain any exotic or expensive metallic species, this in contrast with most of the studied ceramic electrolytes [7].

After this first chapter with an introduction the basics of neutron diffraction are described in chapter 2. Chapter 3 and 4 deal with the neutron diffraction experiments on  $\text{BPO}_4 + z\% \text{Li}_2\text{O}$  and  $\text{LiMn}_2\text{O}_4$  respectively, yielding information on their crystalline structures. In chapter 5 we give an introduction to nuclear magnetic resonance (NMR) and describe NMR experiments on structural features of  $\text{LiMn}_2\text{O}_4$ . In chapter 6 an introduction to the theory of Quasi Elastic Neutron Scattering is given and the experiments on the electronic and magnetic structure of  $\text{LiMn}_2\text{O}_4$  together with the results are described. In chapter 7 we introduce the two-dimensional NMR technique and describe the experiments on the dynamics of Li-ions in  $\text{LiMn}_2\text{O}_4$ . We end with conclusions in chapter 8.



# Chapter 2

## Theory of Neutron Diffraction

From neutron diffraction (ND) one determines the spatial ordering of atoms, molecules or magnetic moments. In this chapter we will describe the theory.

### 2.1 Definitions

Consider a highly collimated, mono-energetic incident neutron beam, so that every neutron has the same energy  $E_0$ , wavelength  $\lambda_0$  and wavevector  $\mathbf{k}_0$ , parallel to the beam direction with length  $k_0 = 2\pi/\lambda_0$ , while  $E_0 = \frac{\hbar k_0^2}{2m_n}$  with  $m_n$  the mass of the neutron. In a scattering experiment with energy analysis one measures the intensity  $I$  of the scattered neutrons as a function of the energy  $E_1$  in the range  $E_1, E_1 + dE_1$ , within the solid angle  $d\Omega$  centered around the wave vector  $\mathbf{k}_1$  of the scattered neutrons. Since the chance of being scattered is small, the intensity will be proportional to the incoming neutron flux  $\Phi(E_0)$ . Then the double-differential cross-section is defined by

$$\frac{d^2\sigma}{d\Omega dE} = \frac{I}{\Phi(E_0)dE_1 d\Omega} \quad (2.1)$$

The momentum transferred to the neutron is:

$$\hbar\mathbf{k} = \hbar(\mathbf{k}_1 - \mathbf{k}_0) \quad (2.2)$$

and the transferred energy is:

$$\hbar\omega = E_1 - E_0 = \frac{\hbar^2}{2m_n}(k_1^2 - k_0^2) \quad (2.3)$$

As a result of the inelastic process the state of the sample is changed: an excitation is created or annihilated.

In case of elastic scattering the lengths of  $\mathbf{k}_0$  and  $\mathbf{k}_1$  are the same and the momentum transfer  $\hbar\mathbf{k}$  to the sample when the neutron is scattered over an angle of  $2\theta$  is given by:

$$k = 2k_0 \sin\theta \quad (2.4)$$

Now the double differential cross section simplifies to the (single) differential cross section, given by:

$$\frac{d\sigma}{d\Omega} = \int_0^\infty \left( \frac{d^2\sigma}{d\Omega dE_1} \right) dE_1 = \frac{I}{\Phi(E_0)d\Omega} \quad (2.5)$$

In the same way one can define the total cross section as:

$$\sigma = \int \left( \frac{d\sigma}{d\Omega} \right) d\Omega \quad (2.6)$$

## 2.2 Elastic scattering by a single nucleus

Nuclear scattering of a neutron on a single, fixed atom is fully described by the total cross section  $\sigma$ . The nucleus can be considered as a point scatterer, since the interaction between a nucleus and an neutron is active over a range in the order of the nucleus diameter ( $10^{-15} - 10^{-14}\text{m}$ ). The scattering will be elastic (since the nucleus is fixed) and isotropic.  $d\sigma/d\Omega = \sigma/4\pi$  can be characterized by one parameter, which can depend on the incoming neutron energy  $E_0$ .

The quantum-mechanical calculation of  $d\sigma/d\Omega$  goes as follows. We place the scattering atom in a cube with a volume of  $L^3$ . The wave function of the incident neutron with wave vector  $\mathbf{k}_0$  is

$$\Psi_i = L^{-\frac{3}{2}} e^{-i\mathbf{k}_0 \cdot \mathbf{r}} \quad (2.7)$$

Using the normalizing constant the neutron density becomes  $\frac{1}{L^3}$  resulting in an incoming flux (neutron speed  $\nu_0$  times density) given by

$$\Phi(E_0) = \frac{\nu_0}{L^3} = \frac{\hbar k_0}{m_n L^3} \quad (2.8)$$

Regarding the symmetry of the process we choose the center of the nucleus as the origin of vector  $\mathbf{r}$ . The isotropic elastic scattering should be described by a spherical wave function

$$\Psi_f = - \left( \frac{b}{r} \right) L^{-\frac{3}{2}} e^{-ik_0 r} \quad (2.9)$$



The (complex) constant  $b$  is called the scattering length. By putting a minus in front of the expression one achieves that  $b$  is positive and real for scattering by an hard nucleus. The total wave function should be zero at the surface of an impenetrable sphere with radius  $r_N$ .

$$\Psi_i(r_N) + \Psi_f(r_N) = 0 \quad (2.10)$$

Substitution of (2.7) and (2.9) in (2.10), together with the property that  $e^{-i\mathbf{k}_0 \cdot \mathbf{r}}$  is almost constant over the nucleus surface  $|\mathbf{r}| = r_N$ , results in

$$b = r_N \approx (1.2 \pm 0.1)A^{\frac{1}{3}} \text{ fm} \quad (2.11)$$

where  $A$  is the mass number of the scattering atom, i.e. the sum of the number of protons ( $Z$ ) and neutrons ( $N$ ) in the nucleus. The relation between  $r_N$  and  $A$  is determined by extensive nuclear physical studies [8].

One finally gets the total cross section  $\sigma$  by dividing the number of scattered neutrons per second

$$I_f = |\Psi_f|^2 4\pi r^2 \nu_0 = 4\pi |b|^2 \frac{\hbar k_0}{m_n L^3} \quad (2.12)$$

by the incoming neutron flux (2.8) so that

$$\sigma = 4\pi |b|^2 \quad \text{and} \quad \frac{d\sigma}{d\Omega} = |b|^2 \quad (2.13)$$

As can be seen in figure 2.1 most elements have a scattering length  $b$  which is real and positive. The scaling of  $b$  with  $A^{\frac{1}{3}}$  is only limited visible, especially for  $A > 70$ . The simple hard-nucleus model is clearly incomplete. That the scattering length does not scale with the atomic weight gives neutron diffraction a big advantage compared to X-ray diffraction. Using neutron diffraction it is possible to observe light elements and to have a good contrast between elements with small differences in atomic weight.

The spin ( $\frac{1}{2}$ ) of the neutron can be parallel or anti-parallel to the nuclear spin ( $I$ ) when it scatters on that nucleus, where  $I=0, \frac{1}{2}, 1, \dots$ . These two situations are not the same and give rise to two different scattering lengths, namely  $b^+$  and  $b^-$  for the parallel and anti-parallel case respectively. The weighted average of these two scattering lengths is called the coherent scattering length and is defined by

$$b_{coh} = \frac{1}{2I+1} [(I+1)b^+ + Ib^-] \quad (2.14)$$

For the total scattering cross section one can write

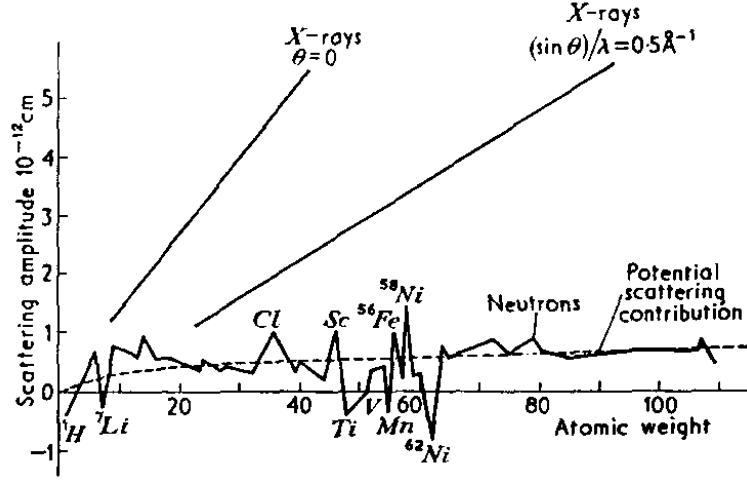


Figure 2.1: Scattering length as function of atomic weight for neutrons and X-rays. The potential scattering given by (2.11) is also displayed (dashed curve).

$$\sigma_s = \frac{4\pi}{2I+1} [(I+1)|b^+|^2 + I|b^-|^2] \quad (2.15)$$

We now give the definitions of  $b_{coh}$ ,  $\sigma_s$  and  $\sigma_{coh}$  for an element consisting of isotopes with abundance  $c_a$  and spin  $I_a$ .

$$b_{coh} = \sum_a \frac{c_a}{2I_a+1} [(I_a+1)b_a^+ + I_a b_a^-] \quad (2.16)$$

$$\sigma_s = 4\pi \sum_a \frac{c_a}{2I_a+1} [(I_a+1)|b_a^+|^2 + I_a|b_a^-|^2] \quad (2.17)$$

$$\sigma_{coh} = 4\pi |b_{coh}|^2 \quad (2.18)$$

Independent on the structure of the system the isotopes which form the element will give rise to an isotropic (incoherent) scattering contribution, given by

$$\sigma_{inc} = \sigma_s - \sigma_{coh} \quad (2.19)$$

where  $\sigma_{inc}$  is the incoherent scattering cross section. In paragraph 2.4 we will deal with the separation between coherent and incoherent scattering again.

## 2.3 Inelastic scattering by a collection of atoms

Consider a collection of atoms in a stationary state, characterized by the quantum numbers  $n_0$  and an incident neutron with wave vector  $\mathbf{k}_0$  and spin  $\sigma_0$ . After scattering, the sample and neutron are characterized by quantum-numbers  $n_1$ , wave vector  $\mathbf{k}_1$  and spin  $\sigma_1$ . In first-order perturbation theory the transition probability per unit of time from the initial state  $|i\rangle$  to the final state  $|f\rangle$  is given by [9]

$$W_{i \rightarrow f} = \frac{2\pi}{\hbar} |\langle f|V|i\rangle|^2 \rho_{k_1}(E_1) \quad (2.20)$$

The interaction potential  $V$  between neutron and sample is a function of the neutron position  $\mathbf{r}$  and the positions of all the nuclei.  $\rho_{k_1}(E_1)$  is the density of final states of the neutron within  $d\Omega$ , between  $E_1$  and  $E_1 + dE_1$ . Using (2.20) and (2.5) gives

$$\left(\frac{d\sigma}{d\Omega}\right)_{i \rightarrow f} = \frac{W_{i \rightarrow f}}{\Phi(E_0)d\Omega} \quad (2.21)$$

Within the defined volume  $L^3$ ,  $\rho_{k_1}(E_1)$  can be written as

$$\rho_{k_1}(E_1)dE_1 = \left(\frac{L}{2\pi}\right)^2 d\mathbf{k}_1 = \frac{L^3}{8\pi^3} k_1^2 dk_1 d\Omega \quad (2.22)$$

Using the relation  $dE_1 = \frac{\hbar^2 k_1}{m_n} dk_1$ , equation (2.8) and the wave functions of the incident and scattered neutron

$$\Psi_i = L^{-\frac{3}{2}} e^{-i\mathbf{k}_0 \cdot \mathbf{r}} = |\mathbf{k}_0\rangle \quad (2.23)$$

$$\Psi_f = L^{-\frac{3}{2}} e^{-i\mathbf{k}_1 \cdot \mathbf{r}} = |\mathbf{k}_1\rangle \quad (2.24)$$

equation (2.21) can be written as

$$\left(\frac{d\sigma}{d\Omega}\right)_{i \rightarrow f} = \frac{k_1}{k_0} \left(\frac{m_n}{2\pi\hbar}\right)^2 |\langle \mathbf{k}_1 \sigma_1 n_1 | V | \mathbf{k}_0 \sigma_0 n_0 \rangle|^2 \quad (2.25)$$

The wave functions of the spin state of the neutron before and after scattering are  $|\sigma_0\rangle$  and  $|\sigma_1\rangle$  respectively.

To get the double differential cross section the conservation law for energy (2.3) is inserted in (2.25) as an  $\delta$ -function. Furthermore (2.25) has to be averaged over an ensemble of initial states weighted with the probability  $p(n_0)p(\sigma_0)$  and summed over all final states, giving

$$\begin{aligned} \frac{d^2\sigma}{d\Omega dE_1} &= \frac{k_1}{k_0} \left(\frac{m_n}{2\pi\hbar}\right)^2 \sum_{n_0\sigma_0} p(n_0)p(\sigma_0) \\ &\cdot \sum_{n_1\sigma_1} |\langle \mathbf{k}_1 \sigma_1 n_1 | V | \mathbf{k}_0 \sigma_0 n_0 \rangle|^2 \delta(\hbar\omega - E_0 + E_1) \quad (2.26) \end{aligned}$$

Equation (2.26) is the basis for the interpretation of arbitrary scattering experiments.

## 2.4 Nuclear scattering

A very good approximation for the interaction potential of a collection of nuclei with positions  $\mathbf{R}_i$  and an incident neutron with  $\lambda_0 \gg r_{N,i}$  is the Fermi pseudo potential, given by

$$V(r) = \frac{2\pi\hbar^2}{m_n} \sum_i b_i \delta(\mathbf{r} - \mathbf{R}_i) \quad (2.27)$$

Substitution in the matrix element of (2.26)

$$\begin{aligned} \langle k_1 | V | k_0 \rangle &= \frac{2\pi\hbar^2}{m_n} \sum_i b_i \int d\mathbf{r} e^{i(\mathbf{k}_1 - \mathbf{k}_0) \cdot \mathbf{r}} \delta(\mathbf{r} - \mathbf{R}_i) \\ &= \frac{2\pi\hbar^2}{m_n} \sum_i b_i e^{i\mathbf{k} \cdot \mathbf{R}_i} \end{aligned} \quad (2.28)$$

gives the general relation for the double-differential cross-section

$$\begin{aligned} \frac{d^2\sigma}{d\Omega dE_1} &= \frac{k_1}{k_0} \sum_{n_0\sigma_0} p(n_0)p(\sigma_0) \sum_{n_1\sigma_1} | \langle \sigma_1 n_1 | \sum_i b_i e^{i\mathbf{k} \cdot \mathbf{R}_i} | n_0\sigma_0 \rangle |^2 \\ &\quad \cdot \delta(\hbar\omega - E_0 + E_1) \end{aligned} \quad (2.29)$$

We restrict ourselves further to the low temperature case, where all positions  $\mathbf{R}_i$  are fixed. Then the scattering will be elastic, i.e.  $E_0 = E_1$ ,  $n_0 = n_1$  and  $\sigma_0 = \sigma_1$

$$\frac{d\sigma}{d\Omega} = \sum_{n_0\sigma_0} p(n_0)p(\sigma_0) \sum_{ii'} e^{i\mathbf{k} \cdot (\mathbf{R}_i - \mathbf{R}_{i'})} \langle n_0\sigma_0 | b_{i'}^* b_i | n_0\sigma_0 \rangle \quad (2.30)$$

defining

$$\langle b_{i'}^* b_i \rangle = \sum_{n_0\sigma_0} p(n_0)p(\sigma_0) \langle n_0\sigma_0 | b_{i'}^* b_i | n_0\sigma_0 \rangle \quad (2.31)$$

leads to

$$\frac{d\sigma}{d\Omega} = \sum_{ii'} e^{i\mathbf{k} \cdot (\mathbf{R}_i - \mathbf{R}_{i'})} \langle b_{i'}^* b_i \rangle \quad (2.32)$$

The two types of averaged products

$$\langle b_{i'}^* b_i \rangle = \langle b_{i'}^* \rangle \langle b_i \rangle \quad \text{if } i \neq i' \quad \langle |b_i|^2 \rangle \quad \text{if } i = i' \quad (2.33)$$

can be notated using a Kronecker  $\delta$ -function as

$$\langle b_{i'}^* b_i \rangle = \langle b_{i'}^* \rangle \langle b_i \rangle + \delta_{i,i'} (\langle |b_i|^2 \rangle - \langle b_{i'}^* \rangle \langle b_i \rangle) \quad (2.34)$$

Substituting (2.34) in (2.32) results in

$$\begin{aligned} \frac{d\sigma}{d\Omega} &= \sum_i [\langle |b_i|^2 \rangle - |\langle b_i \rangle|^2] + \left| \sum_i \langle b_i \rangle e^{i\mathbf{k}\cdot\mathbf{R}_i} \right|^2 \\ &= \left( \frac{d\sigma}{d\Omega} \right)_{inc} + \left( \frac{d\sigma}{d\Omega} \right)_{coh} \end{aligned} \quad (2.35)$$

The first part represents the sum over the incoherent contributions of all separate nuclei. In the second part expresses the interference between the scattering nuclei.

## 2.5 Coherent nuclear scattering by a crystal

In paragraph 2.4 we found the expression for the coherent scattering on a collection of fixed nuclei (2.35).

$$\left( \frac{d\sigma}{d\Omega} \right)_{coh} = \left| \sum_i \langle b_i \rangle e^{i\mathbf{k}\cdot\mathbf{R}_i} \right|^2 \quad (2.36)$$

Before we can use (2.36) on a crystal, we will first have to define it mathematically. A ideal crystal can be obtained by translating a unit cell along three unit vectors  $\mathbf{a}_\nu$  ( $\nu = 1, 2, 3$ ), which are not in the same plain. The unit cell formed by these vectors has a volume of

$$v_a = \mathbf{a}_1 \cdot (\mathbf{a}_2 \times \mathbf{a}_3) \quad (2.37)$$

In general a unit cell will contain  $n$  atoms of which the coordinates relative to the origin of the unit cell are denoted as  $\mathbf{r}_j$ . The origin of the  $l^{th}$  unit cell can be represented as

$$\mathbf{l} = l_1 \mathbf{a}_1 + l_2 \mathbf{a}_2 + l_3 \mathbf{a}_3 \quad (l_\nu \text{ is an integer}) \quad (2.38)$$

We can now write for the position of the  $j^{th}$  atom in the  $l^{th}$  unit cell

$$\mathbf{R}_i = \mathbf{r}_j + \mathbf{l} \quad (2.39)$$

We will now define the three reciprocal lattice vectors  $\mathbf{b}_\mu$  ( $\mu = 1, 2, 3$ )

$$\mathbf{b}_1 = \frac{(\mathbf{a}_2 \times \mathbf{a}_3)}{v_a} \quad \mathbf{b}_2 = \frac{(\mathbf{a}_3 \times \mathbf{a}_1)}{v_a} \quad \mathbf{b}_3 = \frac{(\mathbf{a}_1 \times \mathbf{a}_2)}{v_a} \quad (2.40)$$

The vectors are defined in such a way that they satisfy

$$\mathbf{a}_\nu \cdot \mathbf{b}_\mu = \delta_{\nu\mu} \quad (\nu, \mu = 1, 2, 3) \quad (2.41)$$

The volume of the cell formed by  $\mathbf{b}_1$ ,  $\mathbf{b}_2$  and  $\mathbf{b}_3$  is  $\frac{1}{v_a}$ . An arbitrary reciprocal vector can be written as

$$\boldsymbol{\tau} = h_1 \mathbf{b}_1 + h_2 \mathbf{b}_2 + h_3 \mathbf{b}_3 \quad (h_\mu \text{ integer}) \quad (2.42)$$

For a crystal with one atom in the unit cell on position  $\mathbf{r}_j=0$  (2.36) transfers into

$$\left( \frac{d\sigma}{d\Omega} \right)_{coh} = | \langle b_i \rangle |^2 \left| \sum_i e^{i\mathbf{k} \cdot \mathbf{1}} \right|^2 \quad (2.43)$$

Using equations (2.38), (2.41) and (2.42) one can see from (2.43) that constructive interference (diffraction) will occur when  $\mathbf{k} = 2\pi\boldsymbol{\tau}$ . For a crystal consisting of  $N$  unit cells one can derive

$$\left( \frac{d\sigma}{d\Omega} \right)_{coh} = | \langle b_i \rangle |^2 \left| \sum_i e^{i\mathbf{k} \cdot \mathbf{1}} \right|^2 = N \frac{(2\pi)^3}{v_a} | \langle b \rangle |^2 \sum_{\boldsymbol{\tau}} \delta(\mathbf{k} - 2\pi\boldsymbol{\tau}) \quad (2.44)$$

Coherent scattering, given by (2.44), can be easily represented in reciprocal space using the Ewald-construction. Select an arbitrary reciprocal lattice point as the origin and draw the vector  $\mathbf{k}_0$  to point towards the origin. Since we are assuming elastic scattering (the nuclei are fixed) we have  $|\mathbf{k}_0| = |\mathbf{k}_1| = \frac{2\pi}{\lambda}$  where  $\lambda$  is the wavelength of the neutrons. All points on the sphere of radius  $|\mathbf{k}_0| = |\mathbf{k}_1|$  centered around the starting point of the vector  $\mathbf{k}_0$  describe the end points of the vector  $\mathbf{k} = \mathbf{k}_0 - \mathbf{k}_1$ . The condition  $\mathbf{k} = 2\pi\boldsymbol{\tau}$  is satisfied whenever the surface of the Ewald-sphere coincides with points of the reciprocal lattice. At these points diffraction beams (so called Bragg-peaks) are produced and they are labeled with the indices (hkl) corresponding to the relevant reciprocal lattice point. For arbitrary values of the magnitude and direction of  $\mathbf{k}_0$  this will generally not be the case. In order to observe diffraction one must either use a continuum of incident wavelengths or vary the orientation of the crystal. In figure 2.2 a two dimensional representation of the Ewald-construction is given. For a crystal with  $n$  atoms in the unit cell  $\left( \frac{d\sigma}{d\Omega} \right)_{coh}$  becomes

$$\left( \frac{d\sigma}{d\Omega} \right)_{coh} = N \frac{(2\pi)^3}{v_a} |F_N(\mathbf{k})|^2 \sum_{\boldsymbol{\tau}} \delta(\mathbf{k} - 2\pi\boldsymbol{\tau}) \quad (2.45)$$

where  $F_N(\mathbf{k})$  is the nuclear structure factor of the unit cell, defined by

$$F_N(\mathbf{k}) = \sum_{j=1}^n \langle b_j \rangle e^{i\mathbf{k} \cdot \mathbf{r}_j} \quad (2.46)$$

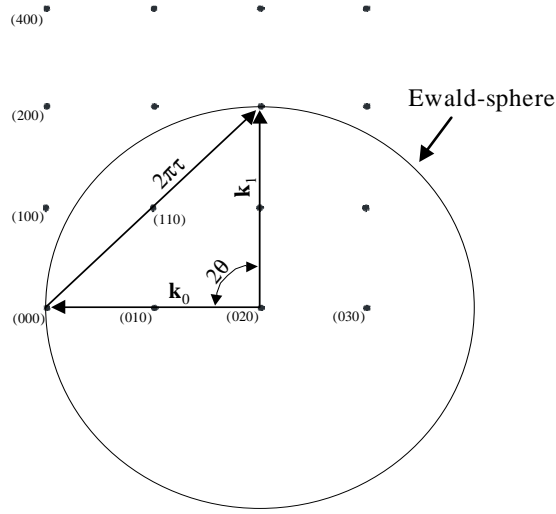


Figure 2.2: The Ewald-sphere of the reciprocal lattice illustrating the condition  $\mathbf{k} = 2\pi\boldsymbol{\tau}$ . Diffraction beams are produced whenever a reciprocal lattice point coincides with the surface of the sphere.

Until now the nuclei were fixed, but in practice they will, due to thermal agitation, move around an equilibrium position  $\mathbf{r}_j$ , so

$$\mathbf{R}_i = \mathbf{l} + \mathbf{r}_j + \mathbf{u}_j(t) \quad (2.47)$$

This does not change the scattering conditions, but  $b_j$  in (2.46) should be multiplied by

$$T_j(\mathbf{k}) = \langle e^{i\mathbf{k}\cdot\mathbf{u}_j} \rangle \quad (2.48)$$

where the averaging is over time.

Assuming an isotropic thermal agitation, the averaging results in

$$T_j(\mathbf{k}) = e^{-W_j(\mathbf{k})} = e^{-\frac{1}{6}\mathbf{k}^2\langle\mathbf{u}_j^2\rangle} \quad (2.49)$$

where  $e^{-W_j(\mathbf{k})}$  is called the Debye-Waller factor of the  $j^{\text{th}}$  atom. Thus, the nuclear structure factor including thermal agitations is given by

$$F_N(\mathbf{k}) = \sum_{j=1}^n \langle b_j \rangle T_j(\mathbf{k}) e^{i\mathbf{k}\cdot\mathbf{r}_j} \quad (2.50)$$

## 2.6 Coherent scattering by a powder

In the previous paragraphs we described the scattering of neutrons on a crystal. In practice the material which one wants to study is not always

a single crystal, but often a powder consisting of many randomly oriented crystallites. The reciprocal lattice will now not consist out of single points anymore but out of concentric spheres around the reciprocal lattice origin, as is displayed in two dimensions in figure 2.3. The Ewald-sphere now intersects all spheres with  $2\pi|\boldsymbol{\tau}| < 2|\mathbf{k}_0|$  (see figure 2.3). This means that in contrast to the single crystal case one needs only one angle-scan at a given  $\mathbf{k}_0$  to detect all the  $|\boldsymbol{\tau}| < \frac{|\mathbf{k}_0|}{2\pi}$ .

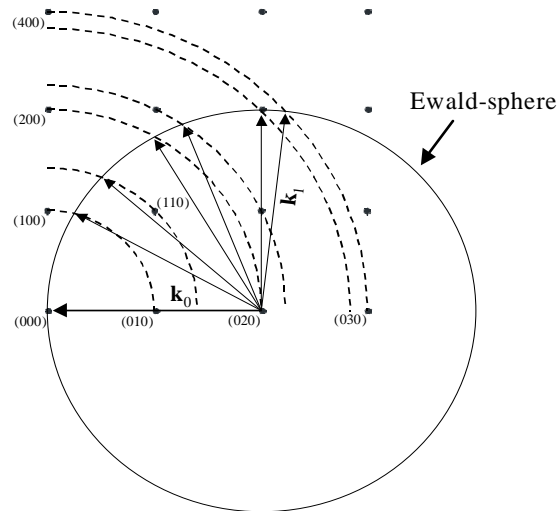


Figure 2.3: The Ewald-sphere of the reciprocal lattice of a powder. Since the powder particles are randomly distributed, the reciprocal lattice points are converted into concentric spheres around the lattice origin. Therefore the Ewald-sphere will coincide with a reciprocal lattice sphere for all  $2\pi|\boldsymbol{\tau}| < 2|\mathbf{k}_0|$ .

A disadvantage of powder diffraction is that  $\boldsymbol{\tau}$ -vectors with a different direction but the same magnitude, e.g. the (100), (010) and (001) reflections in a cubic crystal, can not be detected separately anymore. Therefore one generally uses a profile refinement method (also known as "Rietveld-refinement") to analyze powder diffraction data. With use of a weighted least squares method the calculated diffraction pattern described by a set of parameters  $p_1, p_2, \dots, p_n$  is 'refined' to the measured pattern. The used variables are the instrument characteristics (e.g. resolution parameters) and the structural parameters, such as space group, atomic positions, Debye-Waller factors etc.



## 2.7 Magnetic Diffraction

The neutron is, because of its magnetic moment, a unique tool to study magnetism on an atomic level. The interaction potential is related to the magnetisation density  $\mathbf{M}(\mathbf{r})$ , which is defined as the magnetic moment per unit of volume.  $\mathbf{M}(\mathbf{r})$  in a crystal is caused by both the intrinsic magnetic moment of the electron (electron spin) and the magnetic moment generated by the movement of the electron (orbital magnetic moment). Generally paired electrons generate equal but counter active magnetic moments resulting in a zero magnetisation. Magnetic materials have unpaired electrons resulting in a non zero magnetisation. The interaction potential of the neutron with the unpaired electrons (dipole-dipole interaction) is of the same order as the nuclear interaction and thus measurable.

For magnetic scattering one can also deduce an equation for the differential cross section which is given by [10]

$$\left(\frac{d\sigma}{d\Omega}\right)_M = N \frac{(2\pi)^3}{v_{a,M}} |F_{M,\perp}(\mathbf{k})|^2 \sum_{\boldsymbol{\tau}_M} \delta(\mathbf{k} - 2\pi\boldsymbol{\tau}_M) \quad (2.51)$$

where  $v_{a,M}$  is the volume and  $\boldsymbol{\tau}_M$  is the reciprocal lattice vector of the magnetic unit cell, which is not necessarily the same as the nuclear unit cell.  $F_{M,\perp}(\mathbf{k})$  is the component perpendicular to  $\mathbf{k}$  of the magnetic structure factor  $\mathbf{F}_M(\mathbf{k})$  which is, in contrast to the nuclear structure factor, a vector, given by.

$$\mathbf{F}_M(\mathbf{k}) = \frac{\gamma r_e}{2} \sum_{j=1}^{n_M} \langle \boldsymbol{\mu}_j \rangle f_j(\mathbf{k}) T_j(\mathbf{k}) e^{i\mathbf{k}\cdot\mathbf{r}_j} \quad (2.52)$$

where  $\mu_j$  is the magnetic moment of the  $j^{\text{th}}$  atom,  $T_j(\mathbf{k})$  is the Debye-Waller factor again,  $\gamma = -1.913$  is the gyromagnetic ratio of the electron and  $r_e = 2.818 \text{ fm}$  is the classical electron radius. The normalized magnetic form factor  $f_j(\mathbf{k})$  (i.e.  $f_j(0) = 1$ ) is specific for each atom  $j$  and will be further discussed in chapter 4. Comparing (2.52) with (2.46) shows that  $\frac{\gamma r_e}{2} \langle \boldsymbol{\mu}_j \rangle$  is the magnetic scattering length. The expression for magnetic diffraction is very similar to (2.45). The main difference is that the magnetic form factor  $f_j(\mathbf{k})$  decays very rapidly with increasing  $k$ . Therefore magnetic scattering will mainly be visible at smaller  $k$ -values.

As already has been mentioned the magnetic unit cell does not have to be the same as the nuclear one. In figure 2.4 three simple magnetic structures are shown. For a crystal with randomly oriented magnetic moments one will only see the decaying magnetic form factor figure 2.4a). For a crystal with a ferromagnetic ordering the magnetic unit cell is identical to the nuclear unit

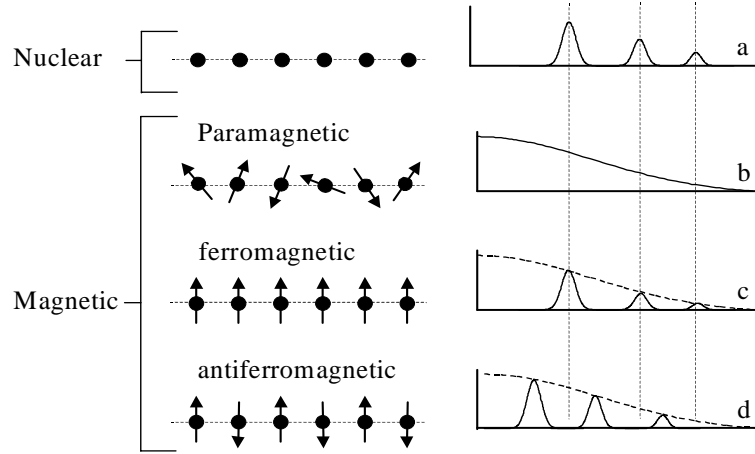


Figure 2.4: Schematic representation of only nuclear diffraction on a system (a) and of only magnetic diffraction on the same system with (b) paramagnetic ordering, (c) ferromagnetic ordering and (d) antiferromagnetic ordering.

cell. The magnetic Bragg peaks are at the same position as the nuclear peaks (figure 2.4b). In the case of anti-ferromagnetic ordered atoms the magnetic unit cell will be twice the nuclear one, resulting in a shift of the magnetic Bragg-peaks to smaller  $k$ -values (figure 2.4c).

In paragraph 4.2 some results of magnetic scattering will be discussed.

## 2.8 Neutron powder diffractometers

There are two kind of neutron powder diffractometers. The oldest and most simple one is the constant wavelength diffractometer. It uses monochromatic (mono-energetic) neutrons and measures the scattered intensity as a function of scattering angle. An example is given in figure 2.5. The scattering vector is determined by  $k = \frac{4\pi}{\lambda} \sin(\theta)$ . So this instrument measures in reciprocal space. This kind of diffractometers is normally used at continuous beams. In paragraph 4.2 constant wavelength diffraction experiments will be discussed.

Another kind of powder diffractometer is the time of flight (TOF) diffractometer. Here the complete wave length spectrum of a pulsed beam is used. By measuring the time of flight of the neutrons, detected in a detector at a fixed angle  $2\theta$  one can calculate the wavelength of the neutron and by that directly the lattice spacing  $d$ , using

$$t_{TOF} = \frac{L}{v} = \frac{Lm_n}{\hbar} \lambda = \frac{Lm_n 2 \sin \theta}{\hbar} d \quad (2.53)$$

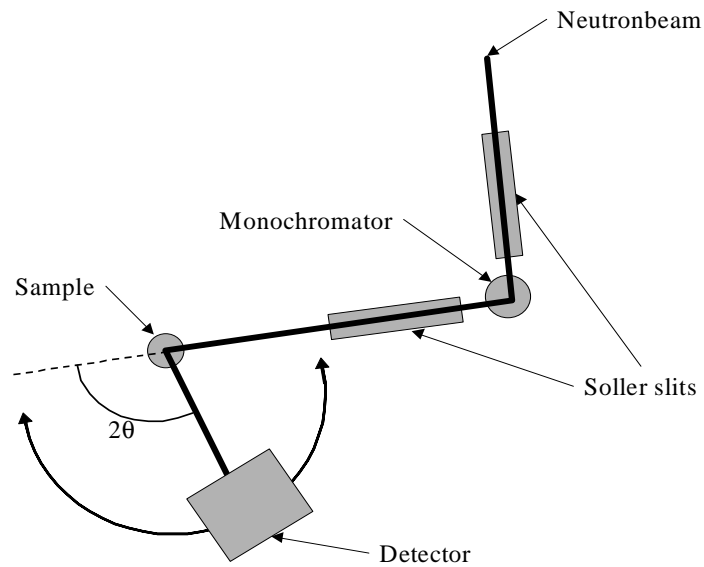


Figure 2.5: The powder diffractometer HB5 at ECN in Petten.

where  $t_{TOF}$  is the time of flight of the neutron and  $L$  is the flight path from source to detector. This technique measures diffraction peaks at a position directly related to lattice spacings  $d$  as can be seen in (2.53) and is mainly used at pulsed sources. In paragraph 3.1 TOF-diffraction experiments will be discussed. In figure 3.2 an example of a TOF-diffractometer is displayed.



# Chapter 3

## Neutron Diffraction on $\text{BPO}_4 + z\% \text{Li}_2\text{O}$

The crystal structure of pure  $\text{BPO}_4$  has been known for many years already [11, 12]. However, no literature has been found on Li-doped  $\text{BPO}_4$ . To reveal the location of the lithium ions neutron diffraction experiments were performed. These experiments and their results will be discussed in this chapter.

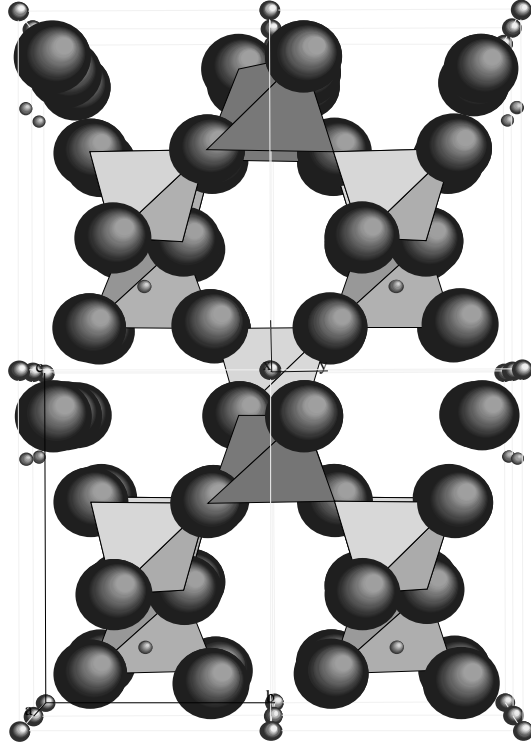
### 3.1 Li-doped $\text{BPO}_4$

The use of Li-doped  $\text{BPO}_4$  as a solid electrolyte for ceramic Li-ion batteries has been demonstrated by Kelder et al. [13]. The ionic conductivity depends on the Li-doping level. A maximum in the conductivity was found around 5 mol% lithium. Crystallographic studies of undoped (pure)  $\text{BPO}_4$  stem from the late 30s [11] and revealed that the crystalline ceramic adopts the high-cristobalite structure. Space group  $I-4$  with lattice parameters  $a = b = 4.3425 \text{ \AA}$  and  $c = 6.6415 \text{ \AA}$  [11] [12]. In the tetragonal unit cell all the  $\text{B}^{3+}$  and  $\text{P}^{5+}$  ions are tetrahedrally coordinated by  $\text{O}^{2-}$  ions, each  $\text{O}^{2-}$  ion being shared by two tetrahedra (figure 3.1).

The defect structure of Li-doped  $\text{BPO}_4$  has been reported by Jak et al. [14] and is given by the defect models



Here, the Kröger-Vink defect notation [14] is used, which reads as follows. In (3.1) a boron (subscript B) vacancy (V) with a net charge 3- (three primes) is surrounded on average by three interstitial (subscript i) Li-ions with a net

Figure 3.1: High-cristabolite structure of  $\text{BPO}_4$ 

charge of + (dot) so that the total net charge is zero. In (3.2) one  $\text{Li}^+$ -ion is located at a boron vacancy ( $\text{Li}_B''$  with two primes for the net charge 2-) and surrounded on average by two interstitial  $\text{Li}^+$ -ions. In these two defect models the ionic conductivity arises completely from the motion of the interstitial  $\text{Li}^+$  ions. In practice one expects both processes (3.1) and (3.2) to be present in a dynamic equilibrium, i.e.



To reveal the ratio between (3.1) and (3.2) neutron diffraction experiments were performed and are described in this chapter.

### 3.1.1 Sample

The synthesis of  $\text{BPO}_4$  with and without Li-doping is described in ref. [15]. Equimolar amounts of boric acid ( $\text{H}_3\text{BO}_3$ ) and phosphorus pentoxide ( $\text{P}_2\text{O}_5$ ) were mixed in water in order to obtain a homogeneous white paste. For the synthesis of Li-doped  $\text{BPO}_4$ , 10 mol% of  $\text{LiOH} \cdot \text{H}_2\text{O}$  was added to the

precursors. The  $\text{BPO}_4$  and 10 mol% Li-doped  $\text{BPO}_4$ -samples were dried under vacuum for several hours.

## 3.2 POLARIS

The neutron diffraction experiments on pure and Li-doped  $\text{BPO}_4$  were performed on the time of flight powder diffractometer POLARIS at the pulse neutron source ISIS (Didcot, England). In figure 3.2 a schematical overview of POLARIS is shown.

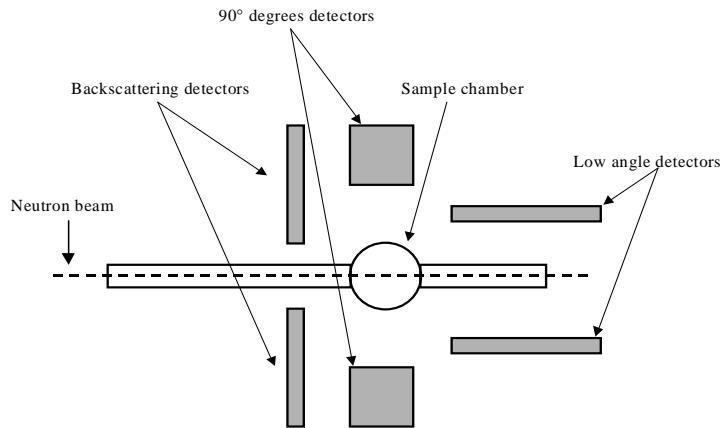


Figure 3.2: A schematical view of the powder diffractometer POLARIS.

POLARIS has three detector banks, located at an scattering angle  $2\theta$  of  $40^\circ$ ,  $90^\circ$  and  $150^\circ$  (backscattering) consisting out of 80 half inch  $^3\text{He}$ , 216 ZnS scintillator and 58 one inch  $^3\text{He}$  detectors respectively. The detectors in one bank are located at both sites of the neutron beam. We have used the detectors at  $90^\circ$  and the backscattering detectors ( $150^\circ$ ), since the first ones have the largest d-space range and the latter ones have the best resolution.

## 3.3 Sample container

The sample container was made out of  $\text{Ti}_{0.68}\text{Zr}_{0.32}$ . The alloy has in this composition a zero coherent scattering length ( $b_{\text{Ti}} = -3.3$  fm and  $b_{\text{Zr}} = 7.1$  fm) and is therefore often called a zero alloy. The advantage of this alloy is that it does not scatter coherently and therefore it will only produce an incoherent background, i.e. a flat background without Bragg-peaks. The sample container had a rectangular shape with a height of 50mm, a width of 20mm,

and a thickness of 2mm. The flat sample container was placed in the beam such that the surface made an angle of  $45^\circ$  with the incoming neutron beam.

### 3.4 Absorption correction

Since the sample was placed in the neutron beam such that it made an angle of  $45^\circ$  with respect to the incoming beam, the absorption on both sites of the beam will be different. The data have been corrected for absorption using standard (numerical) methods [16]. Since the amount of sample in the container was not known, we corrected the data in such a way that after the correction the patterns recorded at different sites of the beam (but in the same detector bank) matched each other. This could be done by changing the amount of sample in the container.

Boron has an enormous absorption cross section for neutrons, i.e. 3835 barn, where normally this is in the order of several barns, this complicates the absorption correction. We were not able to match the spectra, recorded at different sites of the beam, for large time-of-flight values, i.e. the slow neutrons. Since the absorption cross section scales with  $\frac{1}{v}$  these neutrons will be absorbed more than the faster ones. Probably the absorption becomes too large to be properly corrected for. For this reason we did not use the part of the spectra with  $t_{\text{TOF}} > 1500\mu\text{s}$ . The part of the spectra with  $t_{\text{TOF}} < 1500\mu\text{s}$  matched very good with each other.

### 3.5 Rietveld refinement

The neutron spectra were refined using the computer program GSAS (General Structure Analysis System) [17]. In figure 3.3 the spectra, measured at the  $90^\circ$  and backscattering detector bank, of the pure (undoped)  $\text{BPO}_4$  are shown, the dots are the measured data. Refining the data resulted in a good agreement with the structure as reported by [11]. In figure 3.3 the refinement is shown as the solid line. The parameters obtained from the refinement as well as the ones given by [11] are given in table 3.1.

In figure 3.4 the measured data of 10 mol% Li doped  $\text{BPO}_4$  is displayed. As is clearly visible no new peaks have appeared on doping  $\text{BPO}_4$  with lithium, showing the absence of a second phase or a superstructure involving lithium ions or boron vacancies. Refining the data leads to the parameters given in table 3.2. The mean difference with the parameters of the undoped  $\text{BPO}_4$  is the change in the lattice parameters. Doping  $\text{BPO}_4$  with lithium results in a small increase of the a- and b-axis while the c-axis decreases a



Table 3.1: Parameters obtained by refining the data of pure  $\text{BPO}_4$  and the ones reported in literature [12, 11]

Parameter	Refinement	Literature
a=b (Å)	4.3412	4.3525
c (Å)	6.6472	6.6415
B (x,y,z)	(0, 0.5, 0.25)	(0, 0.5, 0.25)
P (x,y,z)	(0, 0, 0)	(0, 0, 0)
O (x,y,z)	(0.137, 0.232, 0.132)	(0.138, 0.260, 0.131)

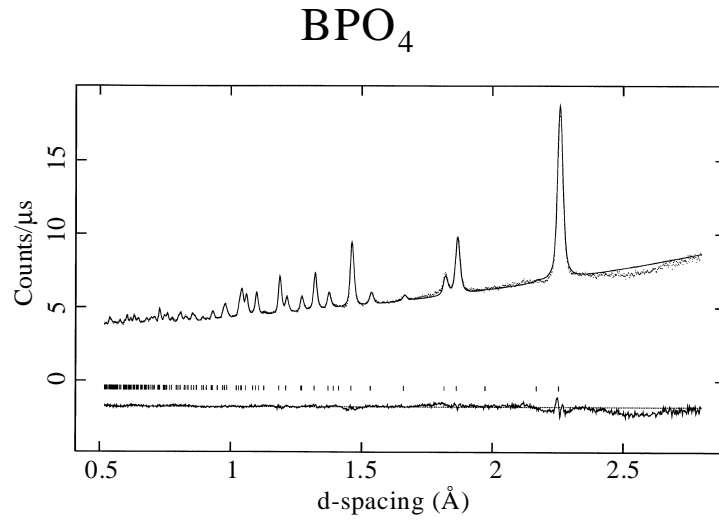
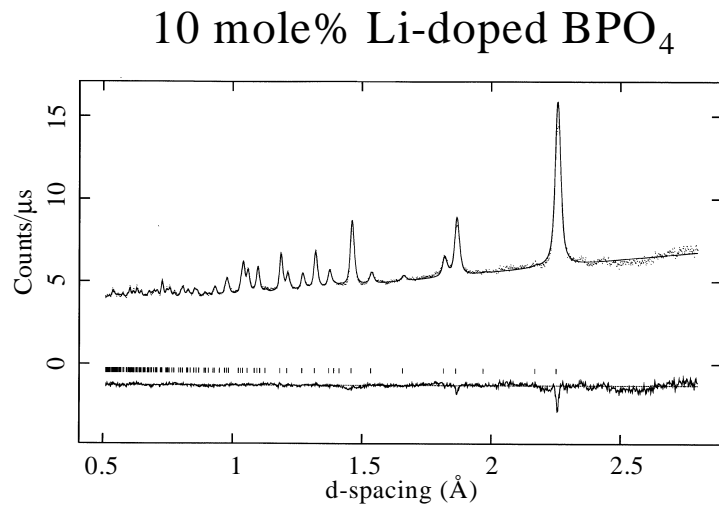
bit. Resulting in a small decrease of the unit cell volume.

Table 3.2: Parameters obtained by refining the data of 10 mole % Li-doped  $\text{BPO}_4$

Parameter	Refinement
a=b (Å)	4.3426
c (Å)	6.6363
B (x,y,z)	(0, 0.5, 0.25)
P (x,y,z)	(0, 0, 0)
O (x,y,z)	(0.139, 0.252, 0.127)

The Bragg-peak at  $2.25\text{Å}$  in figure 3.4 is not fitted very well. This deviation between fit and data might be caused by the (in this region of the spectrum) inaccurate absorption correction, since the absorption in the Li-doped sample is even larger than in the case of undoped  $\text{BPO}_4$  since natural lithium has been used, having a absorption cross section of 70.5 barns.

Since there are no major differences between the spectra of undoped and doped  $\text{BPO}_4$  we conclude that the interstitial  $\text{Li}^+$  ions are randomly distributed over the available lattice sites. The charge compensating boron vacancies or the substitutionally incorporated  $\text{Li}^+$  ions on boron sites are also randomly distributed.

Figure 3.3: Neutron diffraction spectrum of pure  $\text{BPO}_4$ .Figure 3.4: Neutron diffraction spectrum of 10 mole% Li-doped  $\text{BPO}_4$ .

## 3.6 Conclusions

The neutron diffraction experiments on pure and Li-doped  $\text{BPO}_4$  revealed that the interstitial Li-ions and the charge compensating boron vacancies are randomly distributed over the available lattice sites, since there are no major differences between the spectra of pure and Li-doped  $\text{BPO}_4$ . Studying the diffuse scattering (coherent scattering outside the Bragg-peaks) will give information about the random distribution of the boron vacancies and Li-ions. To perform these experiments accurately enough one has to do an empty sample container correction. Furthermore,  $^{10}\text{B}$  will have to be used instead of natural boron to reduce the absorption correction.



# Chapter 4

## Neutron Diffraction on $\text{Li}_x\text{Mn}_2\text{O}_4$

Pure  $\text{LiMn}_2\text{O}_4$  undergoes a phase transition at  $\sim 280$  K [19]. This phase transition is caused by a cooperative Jahn-Teller distortion and hampers the operation of a lithium ion battery. It is known that replacing 2% of the manganese by lithium improves the cyclability and it is assumed that the reason for this is a suppression of the Jahn-Teller effect. To validate this assumption temperature-dependent neutron diffraction experiments have been done and will be discussed in this section.

### 4.1 $\text{Li}_x\text{Mn}_2\text{O}_4$

$\text{LiMn}_2\text{O}_4$  adopts the spinel structure with space group  $\text{Fd}\bar{3}\text{m}$  and with a lattice parameter  $a = 8.24\text{\AA}$ . The structure comprises of a FCC packing of oxygen atoms (32e sites). Manganese ions (50%  $\text{Mn}^{3+}$  and 50%  $\text{Mn}^{4+}$ ) are located in the octahedral sites (16d sites) and the lithium ions in the tetrahedral sites (8a sites). For each lithium which is taken out of the structure (i.e. when the battery is charged) one Mn ion will change its valence from 3+ to 4+ to keep charge neutrality. When lithium enters the structure (i.e. discharging the battery) one Mn ion will change its valence from 4+ to 3+.

#### 4.1.1 Jahn-Teller effect

In lithium manganese oxide the Mn-ions are octahedrally surrounded by six  $\text{O}^{2-}$ -ions. A transition metal (like Mn) has five 3d orbitals, i.e.  $3d_{x^2-y^2}$ ,  $3d_{z^2}$ ,  $3d_{xy}$ ,  $3d_{xz}$ , and  $3d_{yz}$ . In an isolated atom these have the same energy and the level is 5-fold degenerate. However, in an octahedron of oxygens the  $3d_{x^2-y^2}$

and  $3d_{z^2}$  orbitals point directly to an oxide ion [18]. As usual we shall refer to  $3d_{xy}$ ,  $3d_{xz}$ ,  $3d_{yz}$  as the  $t_{2g}$  orbitals and to  $3d_{x^2-y^2}$ ,  $3d_{z^2}$  as the  $e_g$  orbitals. The energies of these two orbitals increase more than the other three compared with the energy levels of the isolated ion. This is due to the interaction with the electrons of the oxygen ion. Therefore the, 3d subshell is split into two levels. Figure 4.1 gives an energy diagram of the two electron-spin states. In  $\text{Mn}^{4+}$  there are three electrons in the 3d shell, which means that all electrons are in the lowest levels. The  $\text{Mn}^{3+}$  has four electrons in the 3d shell. The fourth electron can occupy two orbitals: spin parallel in an  $e_g$  orbital, or spin anti-parallel in a  $t_{2g}$  orbital. The energy difference between the  $e_g$  and the  $t_{2g}$  configuration is denoted as  $\Delta_0$ . Thus the  $\text{Mn}^{3+}$  ion can have two spin states: "high spin" with  $S=2$  and "low spin" with  $S=1$ , while the  $\text{Mn}^{4+}$  ion always has  $S=1.5$ , where  $S$  is the spin quantum number.

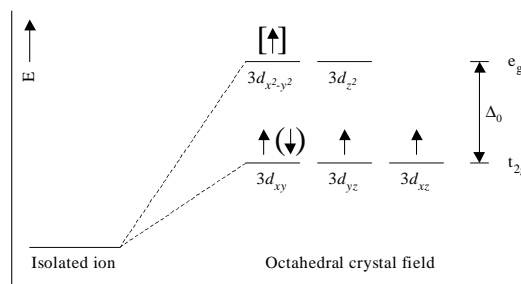


Figure 4.1: The energy diagram of the 3d sub-shell. At the low spin ( $S=1$ ) state the fourth electron is denoted in round brackets, while in the high spin state ( $S=2$ ) it is in the orbital indicated with the square brackets.

When the  $\text{Mn}^{3+}$  ion is in the high-spin state, there is one electron in one of the  $e_g$  orbitals. If this electron is in the  $3d_{z^2}$  orbital, then the  $\text{Mn}^{3+}$ -ion lacks spherical symmetry in such a way that the nucleus is less screened along the  $x$  and  $y$ -directions than along the  $z$ -direction. Consequently the O-ions in the  $xy$ -plane are attracted with a force equivalent to a larger apparent nuclear charge than that effective for the O-ions along the  $z$ -axis. In the same way there will be an attraction between the Mn-ion and the O-ions in the  $z$ -direction when the  $3d_{x^2-y^2}$  orbital is filled. One can imagine that when these interactions are coupled this can initiate a structural phase change, better known as a Jahn-Teller distortion or the Jahn-Teller effect [18]. Such a phase transition has indeed been found in pure  $\text{LiMn}_2\text{O}_4$  around  $T \sim 280$  K [19]. Note that a Jahn-Teller effect is only expected when the  $\text{Mn}^{3+}$  ions are in the high spin state.

### 4.1.2 Recyclability

The structure of an ideal lithium battery should be stable upon intercalating and de-intercalating lithium, since this takes place every time when the battery is discharged or charged respectively. To give an idea of how good the cyclability of a battery material must be we give the following example. A rechargeable battery is not usable anymore when it has only 80% of its original capacity. A lifetime of 500 charge/discharge cycles is reasonable. This demands however a cyclability of 99.96% or better at each cycle.

It is known from literature that pure  $\text{LiMn}_2\text{O}_4$  undergoes a cubic to orthorhombic phase transition at 280 K [19], caused by a cooperative Jahn-Teller distortion. This phase transition is thought to be responsible for the bad recyclability of this material, since the transition breaks up the powder particles leading to a bad electronic and ionic conductivity. To suppress the phase transition, a few percent of the manganese ions are substituted by lithium ions giving the compound  $\text{Li}[\text{Mn}_{2-y}\text{Li}_y]\text{O}_4$ , where  $0 < y < 0.04$ . For every Mn-ion which is replaced by a Li-ion two Mn-ions will have to change their valence from 3+ to 4+. This reduces the amount of the Jahn-Teller active ion  $\text{Mn}^{3+}$ , but it also leads directly to a reduced energy storage capacity. Keeping the amounts of substitution small, i.e. several percent, is a good compromise between the loss of capacity and the gain of recyclability.

### 4.1.3 Sample

#### $\text{Li}[\text{Mn}_{1.96}\text{Li}_{0.04}]\text{O}_4$

In order to study a material which will be used in a real battery, we used commercially produced materials for all the experiments. Another advantage of the commercially produced material is its large quantity, needed to perform all the experiments. The samples we used in the ND, 2D-NMR and QENS measurements were obtained from SEDEMA (Tertre, Belgium). The samples used in the 1D-NMR measurement were obtained from Riedel de Hahn (Seelze, Germany).

#### $\text{Li}_x[\text{Mn}_{1.96}\text{Li}_{0.04}]\text{O}_4$ with $x < 1$

As has been mentioned already, lithium is moving from one site of the battery to the other during charging and discharging. In the case of  $\text{LiMn}_2\text{O}_4$  lithium is pulled out of the structure when the battery is charged and is intercalated in the structure when the battery is discharged (being used). Lithium will have to be extracted from the structure when one wants to study

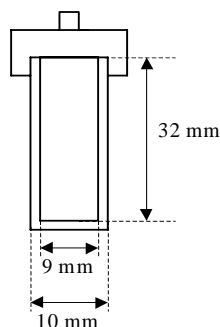


Figure 4.2: The used aluminium sample container.

the "charged" material. Doing this electro-chemically (as in an actual battery) leads to practical problems. An electrolyte will be necessary, which will undoubtedly lead to a mixing up of  $\text{LiMn}_2\text{O}_4$  and the used electrolyte. An other problem is that in order to get a working battery one needs thin layers of  $\text{LiMn}_2\text{O}_4$  (in the order of  $\mu\text{m}$ ) which complicates making large amounts of sample, needed for the experiments. To overcome these problems the so called Hunter's method [20] has been used. Here the lithium is not extracted in a electro-chemical way, but by using sulfuric-acid, giving the same result as when lithium would have been extracted electro-chemically. As starting material the commercially available materials, described above, have been used. After the treatment the samples have been characterized by XRD and Jaeger-Vetter titration.

## 4.2 HB5

Neutron diffraction experiments on  $\text{Li}_x[\text{Mn}_{1.96}\text{Li}_{0.04}]\text{O}_4$  have been performed at HB5 (figure 2.5), a constant wavelength powder diffractometer at the HFR in Petten (the Netherlands). The instrument uses a wavelength of  $2.57 \text{ \AA}$ . HB5 has 4 He-filled detectors which are positioned  $4^\circ$  from each other. The spectra recorded in the different detectors are summed, taking into account the  $4^\circ$  difference between the detectors. HB5 has a  $2\theta$  range of  $5^\circ < 2\theta < 155^\circ$ .

## 4.3 Sample environment

To control the temperature of the sample a closed cycle refrigerator (CCR) has been used. The CCR consists of three stages, has aluminium windows



and is able to bring the sample at a temperature of 4 K. For the higher temperatures, i.e.  $50 \text{ K} < T < 300 \text{ K}$ , a platinum thermal resistor was used to control the temperature. For the temperatures  $3.6 \text{ K} < T < 27 \text{ K}$  a rhodium-iron thermal resistor was used.

The used sample container was made of aluminium because of its good thermal conductivity. The container had a cylindrical shape with a diameter of 9 mm and a height of 32 mm. In figure 4.2 the sample container is shown.

Since the sample container and the windows of the CCR are both made out of aluminium (which has a non-zero coherent scattering length) the background will be polluted by aluminium Bragg-peaks.

## 4.4 Absorption correction

The averaged reduction of the intensity  $A$  of a reflection from a uniform beam due to absorption is given for a scattering angle  $2\theta$

$$A(2\theta) = \frac{1}{V} \int e^{-\mu T} dV \quad (4.1)$$

where the integration is over the volume  $V$  of the sample,  $T$  is the path length of the neutron through the crystal, i.e. the sum of the path lengths for incident and diffracted beams and where  $\mu$  is the absorption coefficient. Using a cylindrical sample one can write for the reduction [21]

$$\begin{aligned} A(2\theta) = \frac{1}{\pi R^2} \int_0^R \int_0^{2\pi} e^{-\mu(R^2 - r^2 \sin^2(\theta + \phi))^{\frac{1}{2}}} \\ \times e^{-\mu(R^2 - r^2 \sin^2(\theta - \phi))^{\frac{1}{2}}} \\ \times \cosh(2\mu r \sin\theta \sin\phi) r dr d\phi \end{aligned} \quad (4.2)$$

where  $R$  is the radius of the cylinder. To correct the measured data for absorption we divided them with  $A$ , which has been calculated numerically and is shown in figure 4.3.

## 4.5 $\text{Li}[\text{Mn}_{1.96}\text{Li}_{0.04}]\text{O}_4$

The neutron spectra of  $\text{Li}[\text{Mn}_{1.96}\text{Li}_{0.04}]\text{O}_4$  at 290, 100 and at 4 K, corrected for absorption, are given in figure 4.5a, 4.5b and 4.5c respectively. Peaks caused by the aluminium windows of the CCR and the sample container are marked by '\*'. The cubic to orthorhombic phase transition would give rise to new peaks in the diffraction pattern (see figure 4.4). It is clearly visible

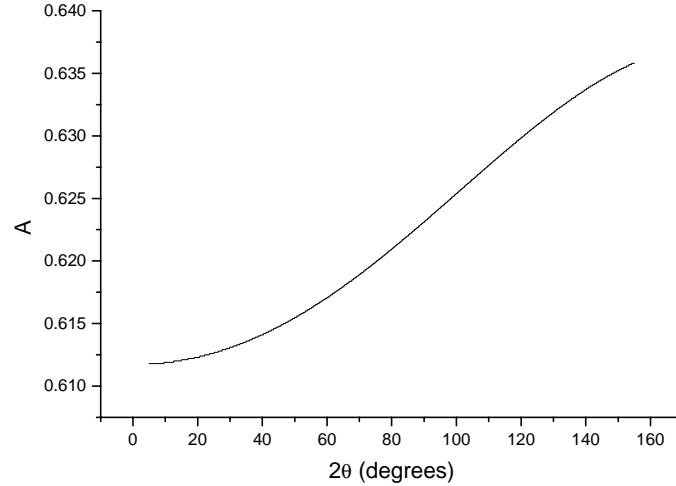


Figure 4.3: The reduction of the intensity  $A$  as a function of  $2\theta$  .

that both at 150 K and at 4 K no new peaks are observed. Indicating that a Jahn-Teller distortion has not occurred.

At low temperatures, i.e. 4 K, a very broad peak at  $2\theta = 32^\circ$  becomes visible (see inset of figure 4.5c), indicating a magnetically disordered structure, a so called spin-glass or -liquid. This is in agreement with magnetisation measurements and muon spin relaxation on the same sample [22]. The disorder is caused by the random character with which Mn is substituted by Li, since there is an ordered magnetic structure in  $\text{LiMn}_2\text{O}_4$  [19].

The structure of the disordered magnetic structure will be discussed further in chapter 6.

## 4.6 $\text{Li}_{0.2}[\text{Mn}_{1.96}\text{Li}_{0.04}]\text{O}_4$

The neutron spectra of  $\text{Li}_{0.2}[\text{Mn}_{1.96}\text{Li}_{0.04}]\text{O}_4$  corrected for absorption at 290, 100 and at 4 K are given in figures 4.6a, 4.6b and 4.6c, respectively. Most of the lithium has been removed from this sample. Therefore, almost all the manganese atoms have a valence of 4+, as for every Li-ion removed from the structure one manganese 3+-ion changes to a 4+-ion. Assuming that all oxide ions are 2- and all lithium ions are 1+, the averaged manganese valence should be 3.96+, which is in agreement with the value measured with Jaeger-Vetter titration. An average manganese valence of 3.96+ leads to a

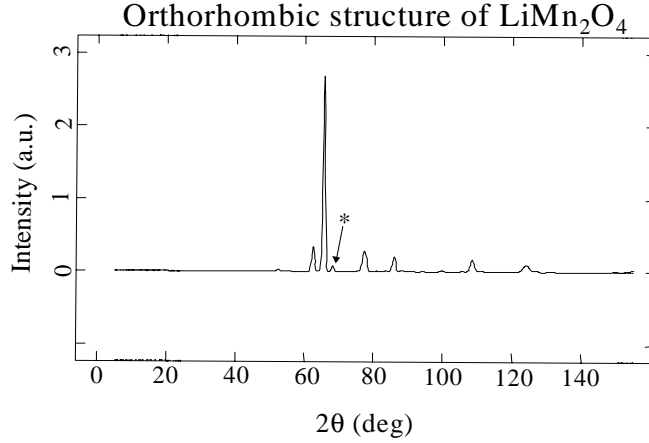


Figure 4.4: The orthorhombic structure of  $\text{LiMn}_2\text{O}_4$ . Peaks which are not visible in the spectrum of the cubic structure are indicated with '\*’.

$\text{Mn}^{3+}/\text{Mn}^{4+}$  ratio of 0.04. As has been explained in the introduction,  $\text{Mn}^{3+}$  is the active Jahn-Teller ion, since this ion is almost not present in this sample we expect no Jahn-Teller distortion here. The neutron experiments shown in figures 4.6a, 4.6b and 4.6c confirm that indeed, i.e. no peaks belonging to the orthorhombic structure are visible.

Decreasing the temperature to 4 K results in contrast to the  $\text{Li}[\text{Mn}_{1.96}\text{Li}_{0.04}]\text{O}_4$  sample in a three-dimensional long-range magnetic ordering. In figure 4.6c the magnetic Bragg peaks belonging to this magnetic structure are clearly visible. The positions of the magnetic peaks are not the same as the positions of the nuclear peaks, meaning that the magnetic unit cell is different from the nuclear one. It is larger than its nuclear counterpart since the peaks are shifted to smaller  $2\theta$ -values, i.e. larger d-space values, with respect to the nuclear peaks. This means that the magnetic active atoms, here only the manganese ions, order in an antiferromagnetic way, since with ferromagnetic ordering the magnetic unit cell is equal to the nuclear, see figure 2.4.

Like in the case of Li-doped  $\text{BPO}_4$ , we use the refinement program GSAS again. This time we try to solve the magnetic structure. Therefore, we have to give GSAS the parameters of the magnetic form factor (see equation (2.52)). The used magnetic form factor is given by [21]

$$f_j(\boldsymbol{\tau}) = 0.3760e^{-12.566s^2} + 0.6602e^{-5.133s^2} - 0.0372e^{-0.563s^2} + 0.0011 \quad (4.3)$$

where  $s = \frac{\sin\theta}{\lambda}$ .

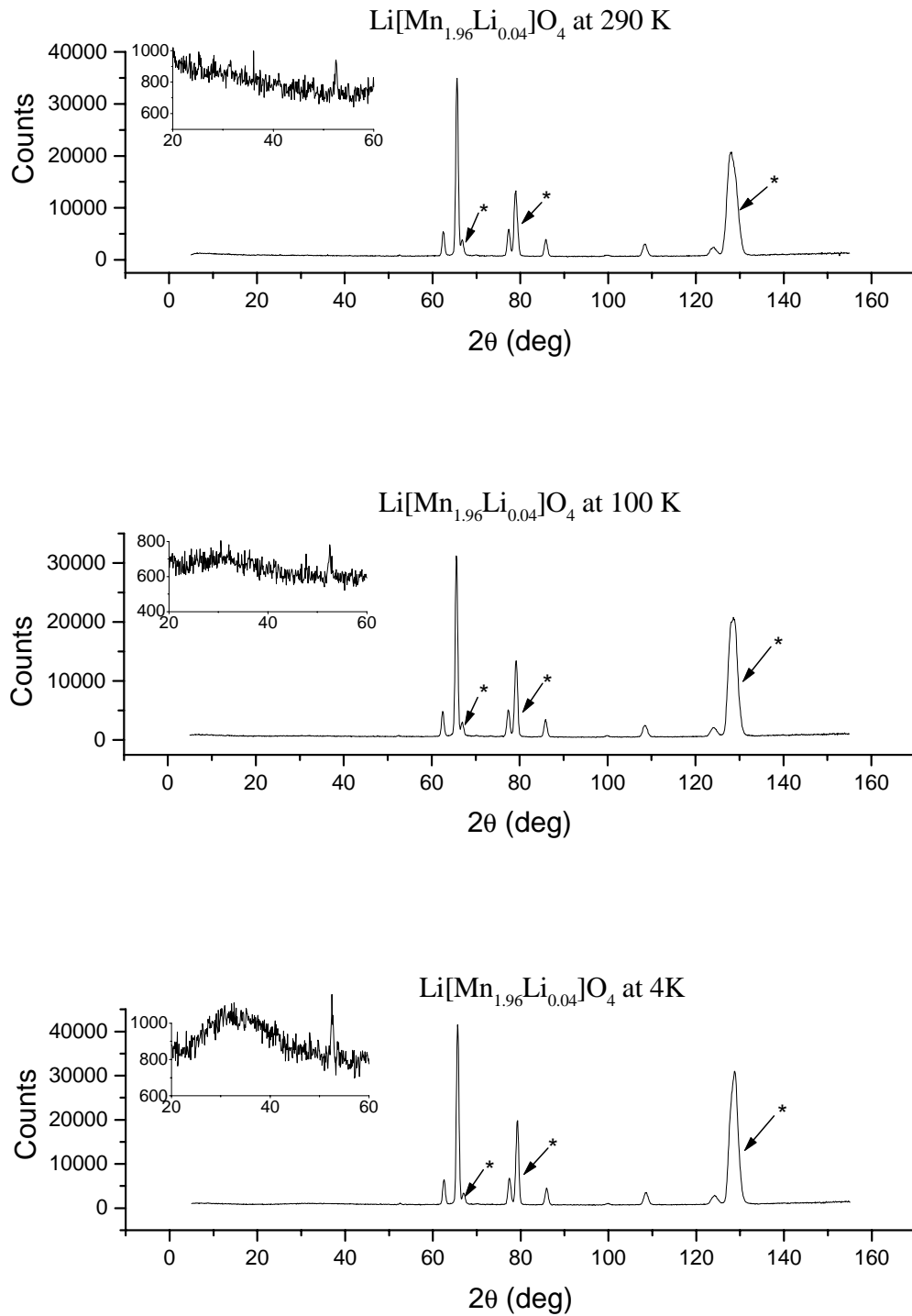


Figure 4.5: The neutron diffraction spectra of  $\text{Li}[\text{Mn}_{1.96}\text{Li}_{0.04}]\text{O}_4$  measured at 4 K, 100 K and 290 K. Reflections from the aluminium CCR windows and sample container are marked with '\*’.

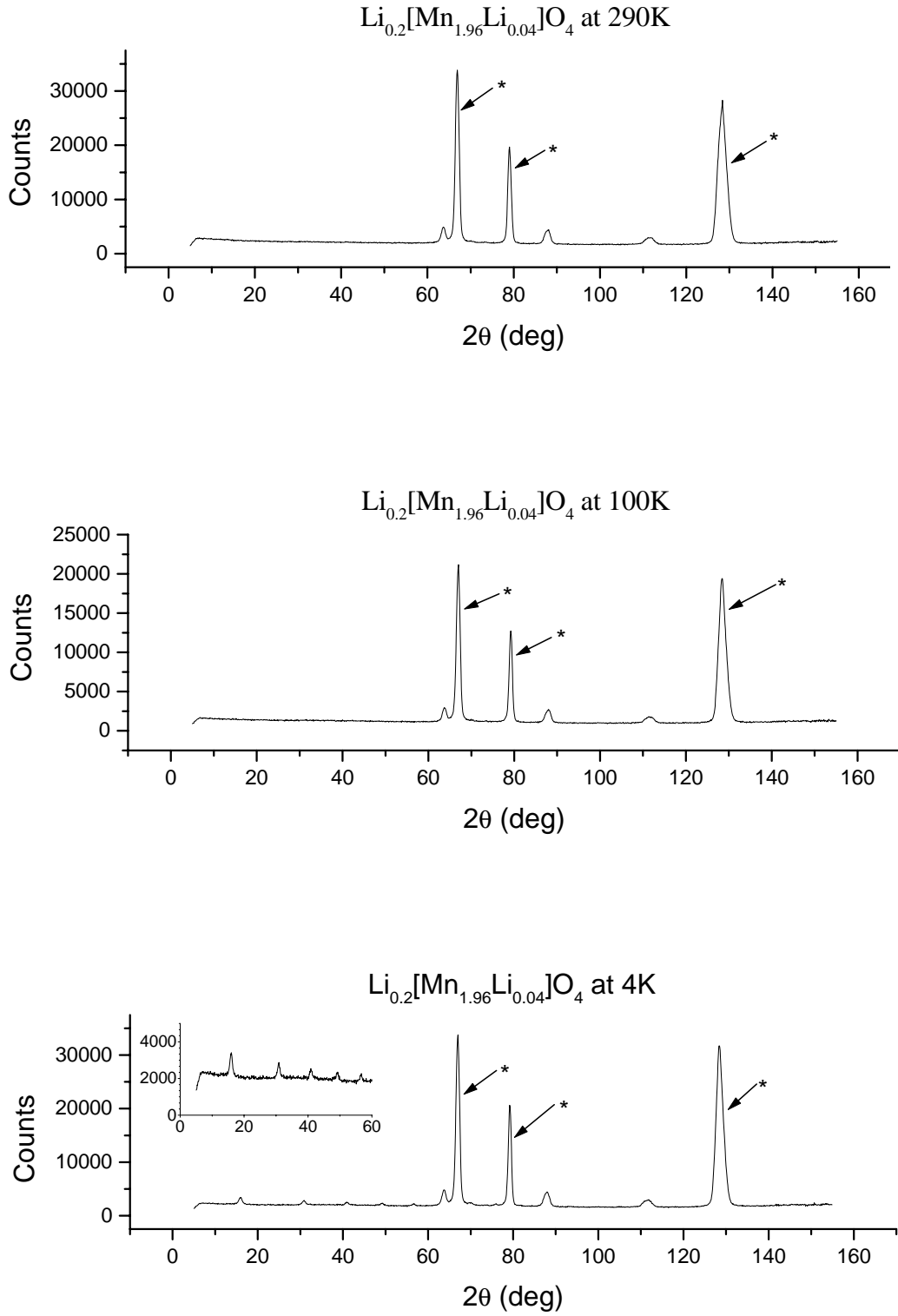


Figure 4.6: The neutron diffraction spectra of  $\text{Li}_{0.2}[\text{Mn}_{1.96}\text{Li}_{0.04}]\text{O}_4$  measured at 4 K, 100 K and 290 K. Reflections from the aluminium CCR windows and sample container are marked with '\*’.

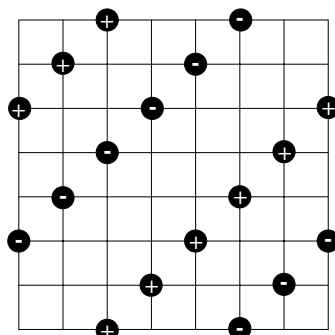


Figure 4.7: The plane  $z=0$  of the model for the magnetic structure. Positions of manganese ions are indicated with a dot. The plus or minus sign determines, whether the manganese spin is parallel or antiparallel to the  $z$ -axis.

To refine the data, a unit cell was constructed which consists solely of manganese ions, since these are the only magnetic ions in the system. In order to get the magnetic Bragg-peaks at the right positions we have to use a magnetic unit cell which is two times the nuclear unit cell in all directions (volume eight times larger).

Eight different models have been refined to the measured neutron diffraction spectrum. Each model has a unit cell with space group P1 (spacegroup number 1) with 128 manganese ions at the same position as in the nuclear unit cell. Each manganese atom has a magnetic moment in the  $z$ -direction. The ordering of the magnetic moments differed from model to model. In figure 4.7 the plane  $z=0$  of one of the models is given. The location of the manganese ions is indicated with a circle, the plus or minus sign indicates whether that particular spin is parallel or antiparallel to the  $z$ -axis. In figure 4.8 the calculated spectrum belonging to the model given in figure 4.7 is shown. As is clearly visible, the positions of the peaks is in agreement with the experiments. However, the intensities are not fitted perfectly. All the other models fit worse, therefore, these are not presented here. This indicates that the ordering of the magnetic moments of the manganese ions is like that in figure 4.7, but that most probably the spins are not parallel to the  $z$ -axis.

There is no possible solution to order 4 spins at the corners of a tetrahedron all antiparallel with each other. In figure 4.9a this is shown for the case of a two-dimensional system, a triangle with on each corner an ion. If the third ion orders antiparallel to the first ion then it is parallel to the second ion and vice versa. Therefore, the ion cannot be ordered anti-parallel to both its neighboring ions. In three dimensions (a tetrahedron) this is exactly

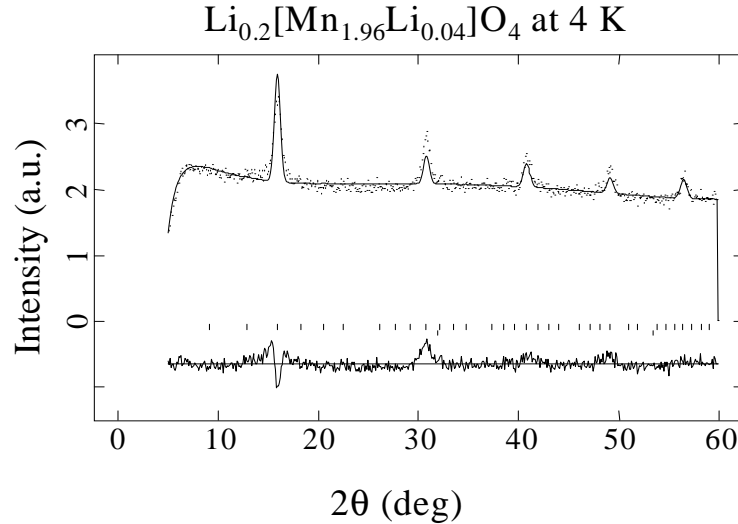


Figure 4.8: Part of the spectrum of  $\text{Li}_{0.2}[\text{Mn}_{1.96}\text{Li}_{0.04}]\text{O}_4$  with the magnetic Bragg-peaks. Measurement is indicated by the dots, the refined spectrum by the solid line.

the same. The phenomenon is called magnetic frustration. Since  $\text{LiMn}_2\text{O}_4$  consists of corner sharing tetrahedra, the system will be magnetically frustrated and, therefore, it will not order simple antiferromagnetically as in the models. In the two-dimensional case there is a solution to get long range ordering. It is called the Néel-ground state, but it is very instable. Here the magnetic moments make a angle of  $120^\circ$  with each other, as shown in figure 4.9b. For the three dimensional case a similar solution exists. Here the magnetic moments point toward or from the centre of the tetrahedron. Most probably models with each spin pointing into three directions will describe the measured data better then the antiferromagnetic models do. However, these models are highly complicated and we did not succeed in finding one that fits the data better then in figure 4.8.

## 4.7 Conclusions

The temperature-dependent neutron diffraction experiments revealed that by substituting 2 percent of the manganese ions by lithium ions results in a total disappearance of the Jahn-Teller distortion. Since the substitution also improves the cyclability of the battery it is assumed that the Jahn-Teller distortion is responsible for this bad cyclability.

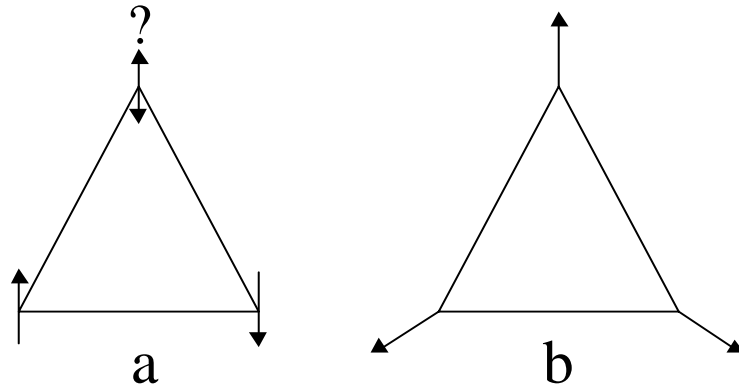


Figure 4.9: Example of magnetic frustration(a) and the Néel-groundstate(b).

The experiments also showed that the manganese spins in  $\text{Li}[\text{Mn}_{1.96}\text{Li}_{0.04}]\text{O}_4$  order only over a short range, whereas the manganese spins in  $\text{Li}_{0.2}[\text{Mn}_{1.96}\text{Li}_{0.04}]\text{O}_4$  order over a long range resulting in a three dimensional magnetic lattice. Unfortunately we did not succeed to refine the magnetic structure. To do this one would have to use more sophisticated models as the ones we have used, and this is an interesting subject for further research. The main differences between the two samples are the lithium content and the average manganese valence. The difference in the magnetic ordering of the manganese ions being caused by this. Since the Néel ground state is very instable, it might very well be possible that the system does not reach this ground state, due to the presence of two ions with different valencies in a tetrahedron. Further research is needed to reveal the actual cause of the difference in magnetic ordering between the two samples.



# Chapter 5

## One Dimensional NMR

One dimensional nuclear magnetic resonance (NMR) gives information about the local surrounding of a specific atom,  ${}^7\text{Li}$  in this case. In this chapter we will describe the theory of one dimensional NMR and give the experimental results obtained by using this technique.

### 5.1 theory

In materials consisting of elements with nuclei with a magnetic moment and a spin angular momentum the phenomenon of magnetic resonance can be observed.

The spin angular momentum  $\mathbf{J}$  is given in units of  $\hbar$  and the maximal observable component  $J$  is given by

$$J = I\hbar \quad (5.1)$$

$I$  is the nuclear spin quantum number of the considered isotope and will be whole or half numbered, i.e.  $0, \frac{1}{2}, 1, \frac{3}{2}, 2$ , etc.. All nuclei with  $I \neq 0$  have a magnetic moment  $\boldsymbol{\mu}$  given by

$$\boldsymbol{\mu} = \gamma\mathbf{J} \quad (5.2)$$

where  $\gamma$  is again the gyromagnetic ratio which has a different value for every isotope.

According to classical mechanics a couple  $\mathbf{T}$  acts on a magnetic moment when it interacts with a magnetic field  $\mathbf{B}_0$ , given by

$$\mathbf{T} = \boldsymbol{\mu} \times \mathbf{B}_0 \quad (5.3)$$

together with

$$\frac{d\mathbf{J}}{dt} = \mathbf{T} \quad (5.4)$$

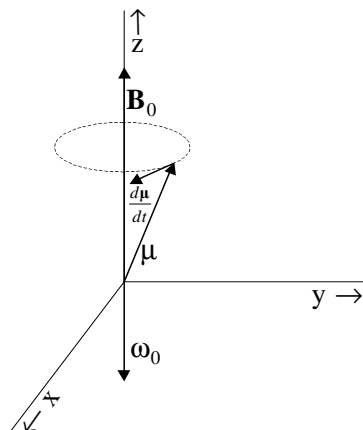


Figure 5.1: Precession of  $\boldsymbol{\mu}$  around the static magnetic field  $\mathbf{B}_0$  with frequency  $\boldsymbol{\omega}_0$

it follows that

$$\frac{d\boldsymbol{\mu}}{dt} = -\gamma\mathbf{B}_0 \times \boldsymbol{\mu} \quad (5.5)$$

Equation (5.5) shows that the magnetic moment precesses around the magnetic field. Characterizing this precession by the vector  $\boldsymbol{\omega}_0$  there has to apply (according to classical mechanics, see figure 5.1):

$$\frac{d\boldsymbol{\mu}}{dt} = \boldsymbol{\omega}_0 \times \boldsymbol{\mu} \quad (5.6)$$

with

$$\boldsymbol{\omega}_0 = -\gamma\mathbf{B}_0 \quad (5.7)$$

The classically deduced resonance frequency.

This resonance frequency can also be deduced in a quantum mechanical way. The interaction energy of a magnetic moment  $\boldsymbol{\mu}$  with an applied magnetic field is given by  $-\boldsymbol{\mu} \cdot \mathbf{B}_0$  or with the use of (5.2)  $-\gamma\mathbf{B}_0 \cdot \mathbf{J}$ . The Hamiltonian describing this interaction will then be

$$\hat{H} = -\gamma\mathbf{B}_0 \cdot \hat{J} \quad (5.8)$$

where  $\hat{J}$  is now an operator with eigenvalues:  $-\mathbf{I}\hbar$ ,  $(-\mathbf{I} + 1)\hbar$ , ...  $(\mathbf{I} - 1)\hbar$ ,  $\mathbf{I}\hbar$ . Solving the time independent Schrödinger equation results in

$$E_m = -\gamma\hbar m B_0 \quad (5.9)$$

The quantum number  $m$  can have the values:  $-I, -I+1, \dots, I-1, I$ , resulting in  $2I + 1$  energy levels.

In the case of a nucleus with  $I = \frac{1}{2}$  there will only be two energy levels with a energy difference  $\Delta E$  between them of

$$\Delta E = \gamma \hbar B_0 \quad (5.10)$$

A transition between the energy levels can be realized by irradiation with a RF magnetic wave. However, the transition will only take place when the energy quanta of the waves are equal to the energy difference between the two levels (Bohr's rule). This results in the resonance condition

$$\hbar \omega_0 = \Delta E = \gamma \hbar B_0 \quad (5.11)$$

or

$$\omega_0 = \gamma B_0 \quad (5.12)$$

Note that the quantum mechanically obtained result is the same as the classical one (5.7). In the following we will use the quantum mechanical description.

### 5.1.1 Relaxation

The distribution of the nuclei over the various energy levels is a result of two counter acting mechanisms. The tendency to go to the lowest energy level is thwarted by the thermal excitations which tend to occupy the  $2I + 1$  energy levels equally. The thermal distribution of nuclei over the energy levels can be described by a Boltzmann-distribution.

$$\left( \frac{n_+}{n_-} \right)_{eq} = e^{\frac{\Delta E}{k_B T}} \quad (5.13)$$

where  $n_-$  is the number of spins in the highest level,  $n_+$  is the number of spins in the lowest level,  $k_B$  is the Boltzmann constant and  $T$  the temperature. At room temperature the  $n_+$  level has a  $10^{-6}$  higher occupancy than the  $n_-$  level.

In NMR RF-fields are applied that create transitions between the levels. The transition probabilities caused by these fields are equal for transitions in both directions (i.e. higher or lower energy levels). Due to the difference in occupancy of the lower lying energy level the total energy of the system will increase through this. This energy will be absorbed from the RF-field. When the RF-field is switched off, the system relaxes back to the Boltzmann-distribution with a certain time constant (relaxation time) due to interactions

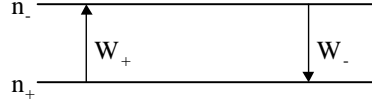


Figure 5.2: Schematic view of the energy levels of a spin  $\frac{1}{2}$  system and transitions between them.

of the spin system with the surroundings that can also create transitions between the spin levels (spin-lattice relaxation).

Consider a situation where only the static magnetic field is present and the spin system is for some reason not in equilibrium. This situation is shown schematically in figure 5.2. Where  $W_+$  is the probability of a transition from the lowest to the highest level per second,  $W_-$  is the probability of a transition from the highest to the lowest level per second. We can now write

$$\frac{dn_+}{dt} = n_-W_- - n_+W_+ \quad (5.14)$$

$$\frac{dn_-}{dt} = -n_-W_- + n_+W_+ \quad (5.15)$$

resulting in

$$\frac{dn}{dt} = 2n_-W_- - 2n_+W_+ \quad (5.16)$$

where  $n = n_+ - n_-$ .

If we furthermore assume that  $n_+^e$  and  $n_-^e$  are the number of spins in equilibrium in respectively the highest and lowest level. Using

$$\begin{aligned} n_+ + n_- &= n_+^e + n_-^e \\ n_{eq} &= n_+^e - n_-^e \\ W_+n_+^e &= W_-n_-^e \end{aligned} \quad (5.17)$$

we can express  $n_-$  and  $n_+$  in  $n$ ,  $n_{eq}$ ,  $W_+$  and  $W_-$ , resulting in

$$\frac{dn}{dt} = -(W_+ + W_-)(n - n_{eq}) \quad (5.18)$$

We now define

$$T_1 = \frac{1}{W_+ + W_-} \quad (5.19)$$

where  $T_1$  represents the spin-lattice relaxation time, which is a measure for the time it takes before the system reaches the equilibrium state after a perturbation.

Equation (5.18) can now be written as

$$\frac{dn}{dt} = -\frac{n - n_{eq}}{T_1} \quad (5.20)$$

which results after integration in

$$n - n_{eq} = (n - n_{eq})_{t=0} e^{-\frac{t}{T_1}} \quad (5.21)$$

Consider a macroscopic system of nuclear spins in a external static magnetic field ( $\mathbf{B}_0$ ). Polarization of the nuclear spins will occur. The magnetization per volume unit ( $\mathbf{M}$ ) is proportional to  $\mathbf{B}_0$ .  $\mathbf{M}$  and  $\mathbf{B}_0$  have the same direction in equilibrium. One can write for the equilibrium magnetization ( $\mathbf{M}_0$ )

$$M_0 = \frac{\chi_v B_0}{\mu_0 \mu_r} \quad (5.22)$$

Where  $\chi_v$  is the volume susceptibility,  $\mu_0$  is the permeability in vacuum and  $\mu_r$  is the relative permeability.

The volume susceptibility  $\chi_v$  is given by

$$\chi_v = \frac{N\gamma^2 \hbar^2 I(I+1)}{3kT} \quad (5.23)$$

where  $N$  is the number of nuclei of the considered isotope per volume unit.

Analogous to (5.5), the behaviour of the magnetization vector  $\mathbf{M}$  can be described by

$$\frac{\delta \mathbf{M}}{\delta t} = -\gamma \mathbf{B}_0 \times \mathbf{M} \quad (5.24)$$

The influence of the spin-lattice relaxation time  $T_1$  on the longitudinal component  $M_z$  can be described, analogous to (5.20), as

$$\frac{\delta M_z}{\delta t} = -\frac{(M_z - M_0)}{T_1} \quad (5.25)$$

Here  $\mathbf{B}_0$  is assumed to be parallel to the z-axis.

Introducing the phenomenological spin-spin relaxation time  $T_2$  causes a decay of the transversal magnetization which can be described by

$$\begin{aligned} \frac{\delta M_x}{\delta t} &= -\frac{M_x}{T_2} \\ \frac{\delta M_y}{\delta t} &= -\frac{M_y}{T_2} \end{aligned} \quad (5.26)$$

Equations (5.25) and (5.26) are valid when there is only a single  $T_1$  and a single  $T_2$ . This is not always the case.

Including the relaxation expressions we can now rewrite (5.24) as

$$\frac{\delta \mathbf{M}}{\delta t} = \gamma \mathbf{M} \times B_0 \mathbf{k} - \frac{M_z - M_0}{T_1} \mathbf{k} - \frac{M_x \mathbf{i} + M_y \mathbf{j}}{T_2} \quad (5.27)$$

where  $\mathbf{i}$ ,  $\mathbf{j}$  and  $\mathbf{k}$  are the unit vectors in the laboratory system. Equation (5.27) is the Bloch equation in the laboratory system. Working out this expression results in

$$\frac{\delta M_x}{\delta t} = \gamma M_y B_0 - \frac{M_x}{T_2} \quad (5.28)$$

$$\frac{\delta M_y}{\delta t} = \gamma M_x B_0 - \frac{M_y}{T_2} \quad (5.29)$$

$$\frac{\delta M_z}{\delta t} = \frac{M_z - M_0}{T_1} \quad (5.30)$$

which has the solutions

$$M_x = (M_{tr})_{t=0} e^{-\frac{t}{T_2}} \cos(\omega_0 t + \phi) \quad (5.31)$$

$$M_y = (M_{tr})_{t=0} e^{-\frac{t}{T_2}} \sin(\omega_0 t + \phi) \quad (5.32)$$

$$M_z = M_0 + (M_z - M_0)_{t=0} e^{-\frac{t}{T_1}} \quad (5.33)$$

with  $M_{tr} = \sqrt{M_x^2 + M_y^2}$  and  $\phi$  is the phase of  $M_{tr}$  with respect to the y-axis at  $t=0$ .

A Fourier transform of this exponentially decaying oscillating signal results in a Lorentz line in the frequency domain. The line shape function  $f(\nu)$  of this Lorentz-line is given by

$$f(\nu) = \pi T_2 \left[ \frac{1}{1 + (2\pi(\nu - \nu_0)T_2)^2} \right] \quad (5.34)$$

where  $\nu_0$  is the position of the center of the line in Hz. The line-width at half the maximum ( $\nu_{\frac{1}{2}}$ ) is then

$$T_2 = \frac{1}{\pi \nu_{\frac{1}{2}}} \quad (5.35)$$

In order to observe the behaviour of the magnetization-vector one will have to bring it out of equilibrium, since the equilibrium corresponds to  $M_z(t) = M(0)$ , i.e. no observable precession. The application of RF-fields can produce well defined non-equilibrium situations. To study such a field we transform the laboratory system into a system that rotates around the z-axis

with an angle frequency  $\omega$ . In this system the magnetization is represented by  $\mathbf{M}$ .

The equation of motion for  $\mathbf{M}$  in the rotating system, neglecting the relaxation times, is given by

$$\frac{d\mathbf{M}}{dt} = \frac{\delta\mathbf{M}}{\delta t} - \boldsymbol{\omega} \times \mathbf{M} = \gamma\mathbf{M} \times \mathbf{B}_0 + \mathbf{M} \times \boldsymbol{\omega} = \gamma\mathbf{M} \times \left( \mathbf{B}_0 + \frac{\boldsymbol{\omega}}{\gamma} \right) \quad (5.36)$$

where  $\frac{\delta\mathbf{M}}{\delta t}$  represents the movement of the magnetization in the laboratory system and from now on  $\frac{d\mathbf{M}}{dt}$  will be used to represent the movement of the magnetization in the rotating system. From (5.36) it is clear that  $\frac{d\mathbf{M}}{dt} = 0$  for  $\boldsymbol{\omega} = -\gamma\mathbf{B}_0$

Including relaxation in (5.36) results in:

$$\frac{d\mathbf{M}}{dt} = \gamma\mathbf{M} \times \left( B_0 + \frac{\omega}{\gamma} \right) \mathbf{k} - \frac{M_z - M_0}{T_1} \mathbf{k} - \frac{M_x \mathbf{i} + M_y \mathbf{j}}{T_2} \quad (5.37)$$

where  $\mathbf{i}$  and  $\mathbf{j}$  are the unit vectors and  $M_x$  and  $M_y$  the magnetization components in the rotation system. Since the z-components are not influenced by the rotation around the z-axis, it also applies that  $M_z = M_z$  and  $M_0 = M_0$ .

Normally the RF-field is a linear polarized field with a magnetic component along the x-axis (in the laboratory system).

$$\mathcal{B}_x = 2\mathcal{B}_1 \cos(\omega t + \varphi) \quad (5.38)$$

This field can be split into two counter rotating fields with equal amplitudes  $\mathcal{B}_1$  and precession frequencies  $\frac{\omega}{2\pi}$  and  $-\frac{\omega}{2\pi}$ . Normally only the component rotating in the same direction as the precessing magnetization will influence this magnetization (the counter rotating field averages to zero in the rotating frame). When the precession frequency of the rotating system is equal to the frequency of the applied RF-field, the effect of the rotating component can be expressed as

$$\begin{aligned} \frac{d\mathbf{M}}{dt} = \gamma\mathbf{M} \left[ \left( B_0 + \frac{\omega}{\gamma} \right) \mathbf{k} + B_1 \cos\varphi \mathbf{i} + B_1 \sin\varphi \mathbf{j} \right] \\ - \frac{M_z - M_0}{T_1} \mathbf{k} - \frac{M_x \mathbf{i} - M_y \mathbf{j}}{T_2} \end{aligned} \quad (5.39)$$

where  $B_1$  is the RF-component which rotates with the same frequency as the rotating system (it is fixed, seen from the rotating system). This is the Bloch-equation in the rotating system, which is valid when  $B_0 \gg B_1$  and  $B_0, B_1 \gg \frac{1}{\pi\gamma T_2}$ .

Equation (5.39) can be interpreted as if the spins in the rotating system feel an effective field  $\mathbf{B}_{\text{eff}}$ , given by

$$\mathbf{B}_{\text{eff}} = \left( B_0 + \frac{\omega}{\gamma} \right) \mathbf{k} + B_1 \cos\varphi \mathbf{i} + B_1 \sin\varphi \mathbf{j} \quad (5.40)$$

Neglecting the influence of  $T_1$  and  $T_2$  the magnetization  $\mathbf{M}$  will, in this system, precess around  $\mathbf{B}_{\text{eff}}$  with angular frequency  $\omega_{\text{eff}}$ .

$$\omega_{\text{eff}} = -\gamma \mathbf{B}_{\text{eff}} \quad (5.41)$$

The magnetization will be influenced mostly by  $B_1$  if  $B_0 + \frac{\omega}{\gamma} = 0$ , corresponding to the resonance frequency.

### 5.1.2 Pulses

A pulse is defined as irradiating with a RF-field with a well defined frequency, amplitude and phase for a relatively short time. The pulse lengths meant here are short compared to the relaxation times; therefore we will neglect the influence of the relaxation times during these pulses. When the RF-field has the same frequency as the resonance frequency (5.39) will result in

$$\frac{d\mathbf{M}}{dt} = \gamma \mathbf{M} \times \mathbf{B}_1 \quad (5.42)$$

This equation shows that if the phase  $\varphi$  is zero, the magnetization is rotating around the x-axis in the rotating system with an angular frequency

$$\omega_1 = \gamma \mathbf{B}_1 \quad (5.43)$$

Irradiating during a time  $t_w$  results in a rotation ( $\alpha$ ) of the magnetization.

$$\alpha = \int_0^{t_w} \omega_1(t) dt = \int_0^{t_w} \gamma B_1(t) dt \quad (5.44)$$

The cases  $\alpha = \frac{\pi}{2}$  or  $\alpha = \pi$  are called  $90^\circ$  and  $180^\circ$  pulses. Starting with  $M_0$  parallel to  $B_0$  a  $90^\circ$  pulse with  $\varphi = 0$  will result in a magnetization along the y-axis (see figure 5.3). A  $180^\circ$  pulse inverts the equilibrium magnetization.

If  $\varphi = 0$  we speak about a  $90_x^\circ$  or a pulse along the x-axis. When  $\varphi = \frac{\pi}{2}$  it is called a  $90_y^\circ$  pulse. In the case that the RF-frequency and the resonance frequency do not match, the magnetization will precess around  $\mathbf{B}_{\text{eff}}$  with a angular frequency given by (5.41).



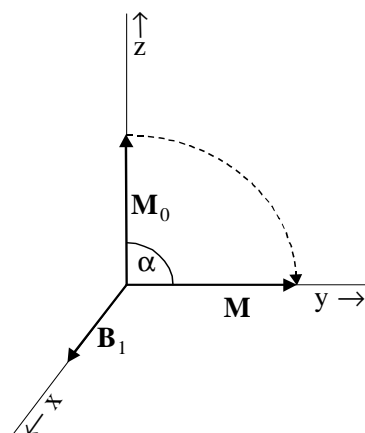


Figure 5.3: Schematic representation of a  $90^\circ_x$  pulse.

### 5.1.3 Chemical Shift

Nuclei with different surroundings (e.g. different crystallographic sites) will feel a distinct external field, caused by the magnetic interaction of the field with the electrons surrounding the nuclei. The field at the nuclear site becomes different from the applied field and their precession frequencies will be shifted with respect to each other. This shift is called the chemical shift.

The chemical shift,  $\sigma$ , is caused by the electron polarization at the nuclear site induced by the external field  $B_0$  in the material.  $\sigma$  can be divided into four parts, i.e.

$$\sigma = \sigma_d + \sigma_p + \sigma_n \quad (5.45)$$

where  $\sigma_d$  is a diamagnetic shielding term, which reduces the field  $B_0$  at the position of the considered nucleus,  $\sigma_p$  is a paramagnetic term that usually enhances  $B_0$ .  $\sigma_n$  is a contribution to the chemical shift which can be positive or negative and is caused by the polarization of electrons of neighboring atoms hybridized with electrons on the NMR isotope. We will not describe these contributions in more detail.

In principle the direction of the applied field relative to the crystallographic axis, i.e. the orientation of the electrons around the nucleus relative to the field, is of importance since the polarizability of the electrons can vary with this direction. This leads to the so called chemical shift anisotropy. In a powder all directions are present and the presence of chemical shift anisotropy can lead to a distribution of resonance frequencies, a so called powder pattern.

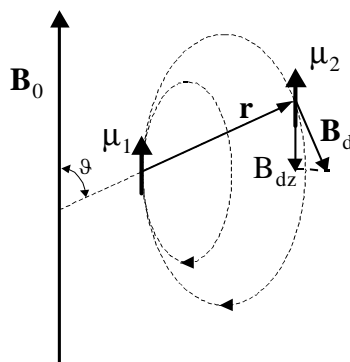


Figure 5.4: The component of the dipole-dipole interaction parallel to the z-axis.

#### 5.1.4 Direct dipole-dipole interaction and Magic Angle Spinning (MAS) NMR

Consider the component,  $\mathbf{B}_{dz}$ , of the local dipole field ( $\mathbf{B}_d$ ) of spin  $\mu_1$  at the position of  $\mu_2$  to be parallel to  $\mathbf{B}_0$ , see figure 5.4. Components of  $\mathbf{B}_d$  perpendicular to  $\mathbf{B}_0$  are neglected here when  $B_0 \gg B_d$ .  $B_{dz}$  can then be given by (see figure 5.4)

$$B_{dz} = \frac{\mu_1}{4\pi r^3}(3\cos^2\vartheta - 1) \quad (5.46)$$

In poly-crystalline materials many values of  $\vartheta$  will be present, resulting in resonance frequencies in the area

$$\gamma \left( B_0 - \frac{\mu_1}{4\pi r^3} \right) < \omega_{res} < \gamma \left( B_0 + \frac{2\mu_1}{4\pi r^3} \right) \quad (5.47)$$

In many cases in the solid state this area is so big that the effects of chemical shift become invisible. For instance interactions between protons in various molecules the spectrum will be broadened in this way.

Due to movements of the molecules (5.46) will have to be averaged over time. In isotropic, non viscous liquids this time averaging can be replaced by an average over all possible values of  $\vartheta$ .

$$\langle B_{dz} \rangle \sim \int_0^\pi (3\cos^2\vartheta - 1)\sin\vartheta d\vartheta = 0 \quad (5.48)$$

Therefore dipole-dipole interactions are not visible in the NMR spectrum of liquids and narrow lines can be observed, yielding chemical shifts.

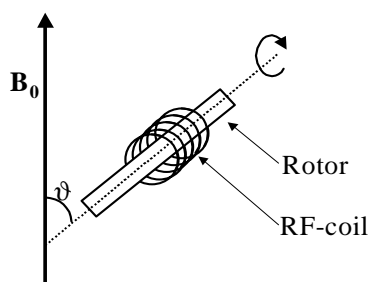


Figure 5.5: A schematic representation of the orientation of the MAS-rotor and RF-coil with respect to the external magnetic field  $B_0$ .

Equation (5.46) becomes zero for  $\vartheta = 54.74^\circ$ . Spinning the sample, with a frequency large compared to the dipolar interaction strength, around an axis which is under an angle of  $\vartheta = 54.74^\circ$  with respect to the external magnetic field, results in an averaging out of the dipole-dipole interaction. Narrow lines will be visible again, making it possible to observe chemical shifts and scalar interactions. This technique is called Magic Angle Spinning NMR (MAS-NMR) and the arrangement of the rotor with respect to the external magnetic field is shown in figure 5.5.

A second effect of MAS is that the chemical shift anisotropy is averaged leading to narrow lines separated by the MAS frequency instead of the broad powder patterns.

### 5.1.5 Quadrupole interaction

In the previously section we considered only nuclei with  $I = \frac{1}{2}$ . If a nucleus has a spin of  $I = \frac{3}{2}$ , like  ${}^7\text{Li}$ , then there will not be a single transition but there will be three transitions, i.e.  $m = \frac{3}{2} \leftrightarrow m = \frac{1}{2}$ ,  $m = \frac{1}{2} \leftrightarrow m = -\frac{1}{2}$ ,  $m = -\frac{1}{2} \leftrightarrow m = -\frac{3}{2}$ . Depending on the quadrupole interaction one will observe a central transition resonance with two satellite resonances or only the central one.

A spin  $\frac{3}{2}$  atomic nucleus has four different energy levels in a large magnetic field. In the absence of a nuclear quadrupole interaction, these energy levels are equally spaced. Because only transitions between neighboring energy levels can be induced by the R.F.-pulse of the NMR spectrometer, there are only three different nuclear spin transitions and they all occur at the same frequency.

In the presence of a nuclear electric quadrupole interaction, the energy levels are shifted and the three different transitions occur at different fre-

quencies. In first order perturbation theory, these frequencies are related to the nuclear electric quadrupole interaction as follows [23]:

$$\omega_{\frac{3}{2}} = \omega_0 - \frac{1}{4} \frac{e^2 q Q}{h} [(3 \cos^2 \vartheta - 1) + \eta \sin^2 \vartheta \cos 2\phi] \quad (5.49)$$

$$\omega_{\frac{1}{2}} = \omega_0 \quad (5.50)$$

$$\omega_{-\frac{1}{2}} = \omega_0 + \frac{1}{4} \frac{e^2 q Q}{h} [(3 \cos^2 \vartheta - 1) + \eta \sin^2 \vartheta \cos 2\phi] \quad (5.51)$$

where  $\vartheta$  and  $\phi$  are the polar and azimuthal angles of the orientation of the principal axis system in the laboratory coordinate system,  $eQ$  is the nuclear quadrupole moment of the ion,  $eq$  is the electric field gradient (EFG) at the nuclear site and  $\eta$  the asymmetry parameter corresponding to asymmetry in the EFG. The central transition is unshifted by the first order quadrupole interaction; whereas, the two outer transitions are shifted from the Larmor frequency  $\nu_0$  by an amount that is directly proportional to the quadrupole coupling constant  $\frac{e^2 q Q}{h}$ . The central transition is a narrow, intense peak at the Larmor frequency and the outer transitions frequencies are spread over a range because of the dependence on orientation ( $\vartheta$ ,  $\phi$ ). The outer transitions are called "satellite" transitions. The positions of the satellite transitions are much more sensitive to the surroundings or details of the ion binding than that of the central transition. From equations (5.49) and (5.51) it is clear that like the dipole-dipole interaction the first order quadrupole interaction (with  $\eta=0$ ) can also be suppressed by using the MAS NMR technique described in the previous section: when MAS is applied  $3 \cos^2 \vartheta - 1 \approx 0$ .

When the calculation is extended to include second order effects, the frequencies of the outer transitions remain the same. However, the central transition frequency shifts [23]:

$$\omega_{\frac{1}{2}}^{(2)} = -\frac{1}{64} \left( \frac{e^2 q Q}{h} \right)^2 \frac{1}{\omega_0} [3(1 - \cos^2 \vartheta)(9 \cos^2 \vartheta - 1)] \quad (5.52)$$

In the case of  $\text{Li}[\text{Mn}_{2-y}\text{Li}_y]\text{O}_4$ , the small electric field gradient (because of the cubic crystal structure) and the small nuclear quadrupole moment of  ${}^7\text{Li}$  (i.e.  $-3 \cdot 10^{-30} \text{ m}^2$  [24]) make that the first and second order effects can be neglected. This can also be observed from the constant spectrum width in ppm on 300 and 400 MHz NMR setups. Therefore the quadrupole interaction will not have an influence on the shape of the  ${}^7\text{Li}$  NMR spectrum of  ${}^7\text{Li}$  NMR on  $\text{Li}[\text{Mn}_{2-y}\text{Li}_y]\text{O}_4$

### 5.1.6 Line width

The "homogeneous" line width of a NMR resonance under MAS conditions is depending on a few parameters, such as residual dipolar-interactions, second order quadrupole interactions and, if present, the exchange rate of motions of the probed nucleus. The "heterogeneous" line width depends on static spread in chemical shift, quadrupole interactions or the external applied field. All of these interactions and sources of line broadening (except the external field) can be averaged by rapid exchange between a large number of different sites, leading to so called motional averaging. In the case of exchange between just two environments A and B there are two extremes. In the case of the fast exchange extreme, the two spectra will have merged to form a single spectrum with the mean spectral parameters. This single spectrum widens as the exchange rate decreases, reflecting the less effective averaging of the two environments A and B. That is, fast exchange causes the spins to experience effective local field and quadrupole interaction that is the mean of the two sites between which they hop.

In the case that the exchange between the two sites A and B is slow, i.e. much slower than the difference of spectral resonances expressed in Hz, a measurable effect on the NMR line width can be observed if the exchange is comparable or faster than the line width expressed in Hz. In this case the line width is, in a first order approximation, equal to  $\Gamma = \Gamma_0 + \frac{1}{\sqrt{2}\tau_{exchange}}$ , i.e. as a result of a kind of life time broadening the line width increases as the exchange rate  $\frac{1}{\tau_{exchange}}$  increases. It is this approximation that we will use in paragraph 5.2.2 for determination of the lithium mobility time scales in  $\text{Li}_{0.75}[\text{Mn}_{1.95}\text{Li}_{0.05}]\text{O}_4$ .

In the case of an intermediate exchange rate the differences in the timescale of the evolution of the nuclear spin states and the exchange between the different sites are on a similar time scale. The spectra have often broad features that can be simulated numerically.

Changing the temperature may change the exchange rate of the system which in the slow or fast exchange regime will result in a changing of the line width of the measured spectrum.

## 5.2 Experiment

The  $^7\text{Li}$  MAS NMR spectra, presented in this chapter, were recorded using a NMR instrument at the NSR Center in Nijmegen, which was kindly made available to us. The Bruker DMX-300 spectrometer operated at a frequency (resonance frequency of  $^7\text{Li}$ ) of 116 MHz. A 2.5 mm MAS probe spinning

at 28 kHz was employed. The temperature was controlled by putting the sample in a heated nitrogen gas flow and was stabilized within 0.5 K. The temperature of the sample will differ from the temperature of the gas flow, due to friction caused by the high spinning frequencies. Calibration of the sample temperature was performed using the  $^{207}\text{Pb}$  resonance of  $\text{Pb}(\text{NO}_3)_2$  [25].

The  $90^\circ$  and  $180^\circ$  pulses were determined to be  $1.7 \mu\text{s}$  and  $3.3 \mu\text{s}$  respectively. The used band width was 500 kHz except for the  $\text{Li}_{0.2}[\text{Mn}_{1.95}\text{Li}_{0.05}]\text{O}_4$  where a band width of 1 MHz was used. Determination of the relaxation time  $T_1$  resulted in a value of 10 ms at 345 K. This  $T_1$  did not depend on the temperature very much.

As reference point the resonance of  $^7\text{Li}$  in an aqueous solution of  $\text{LiCl}$  has been used.

### 5.2.1 Data analysis

To suppress noise, we apodized the measured data, also called free induction decay (FID), using a  $\cos^2$  function. After that, the size of the data was doubled by adding zeros (so called zero filling) in order to make the Fourier transformed data smoother. Then the data were Fourier transformed using a complex Fourier transform. After Fourier transforming the data was phased. In figure 5.6 a typical Fourier transformed spectrum is shown. As is clearly visible the baseline contains a broad oscillation. This broad oscillation will be caused by the first few points of the FID. Deleting the first points and then predicting them back using the other data points normally results in an improvement of the background. Here this was not the case and therefore a baseline correction was applied. In figure 5.7 the same data is displayed as in figure 5.6 but now the baseline is corrected.

In general one means with the term "NMR spectrum" the Fourier transformed data. The spectra are plotted as a function of the resonance frequency relative to the resonance frequency of  $^7\text{Li}$  in  $\text{LiCl}$  in ppm (parts per million).

### 5.2.2 $\text{Li}_x[\text{Mn}_{1.95}\text{Li}_{0.05}]\text{O}_4$

#### $\text{Li}[\text{Mn}_{1.95}\text{Li}_{0.05}]\text{O}_4$

In figure 5.8 the  $^7\text{Li}$  MAS NMR spectra of  $\text{Li}[\text{Mn}_{1.95}\text{Li}_{0.05}]\text{O}_4$  are shown as a function of temperature. The strongest MAS NMR spinning side band manifold in the spectrum is assigned to lithium on 8a sites, which is the lithium site with the highest occupancy as was observed in neutron diffraction [26]. The smaller peak is assigned to the 16c site since it is located at the same

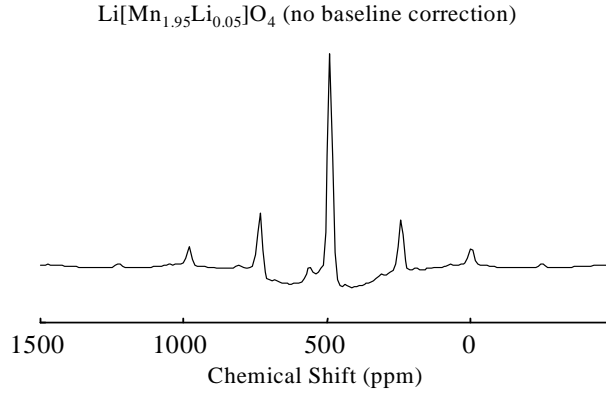


Figure 5.6: Typical  ${}^7\text{Li}$  MAS NMR spectra of  $\text{Li}[\text{Mn}_{1.95}\text{Li}_{0.05}]\text{O}_4$  at a spinning speed of 28 kHz (241 ppm).

chemical shift as the 16c site resonance in the spectra discussed in chapter 7 [27]. This peak shifts towards the 8a site peak when the temperature is increased. Since the peaks of this sample are broader than the ones reported in chapter 7 [27], the 16d and 8a site resonances are overlapping each other, what makes the peak belonging to the 16d site invisible.

### **Li<sub>0.75</sub>[Mn<sub>1.95</sub>Li<sub>0.05</sub>]O<sub>4</sub>**

In figure 5.9 the  ${}^7\text{Li}$  MAS NMR spectra of  $\text{Li}_{0.75}[\text{Mn}_{1.95}\text{Li}_{0.05}]\text{O}_4$  are shown as a function of temperature. In contrast to the spectra of  $\text{Li}[\text{Mn}_{1.95}\text{Li}_{0.05}]\text{O}_4$  there is only one peak manifold visible. Furthermore it is clearly visible that the peaks become broader at 400 K, which might point at an increase in the lithium dynamics. Extracting lithium creates vacancies in the crystal lattice, which will enhance the lithium mobility, since it has more places to go to. This influence of the vacancy concentration is given by [28]

$$D_{self} = [V]D_v \quad (5.53)$$

where  $D_{self}$  is the self diffusion coefficient, in this case of lithium,  $[V]$  is the concentration of vacancies and  $D_v$  is the diffusion coefficient of the vacancies. When the lithium ions are moving fast from one site to the other the NMR resonances belonging to these sites will shift towards each other and finally they will merge (so called motional averaging). This might very well be the reason why only one sideband manifold is observed. The broad spinning side band manifold for each site will be caused by interactions between the nuclear and unpaired electron spins as described in [31], it is not caused

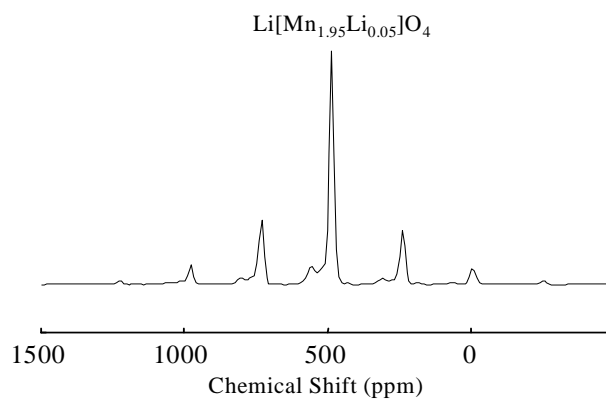


Figure 5.7:  ${}^7\text{Li}$  MAS NMR spectra of  $\text{Li}[\text{Mn}_{1.95}\text{Li}_{0.05}]\text{O}_4$  where a baseline correction has been applied.

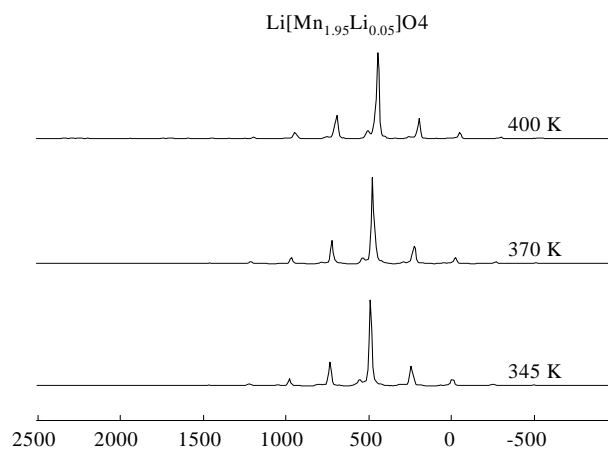


Figure 5.8:  ${}^7\text{Li}$  MAS NMR spectra of  $\text{Li}[\text{Mn}_{1.95}\text{Li}_{0.05}]\text{O}_4$  at temperatures as indicated in the figure. The spinning speed equals 28 kHz.



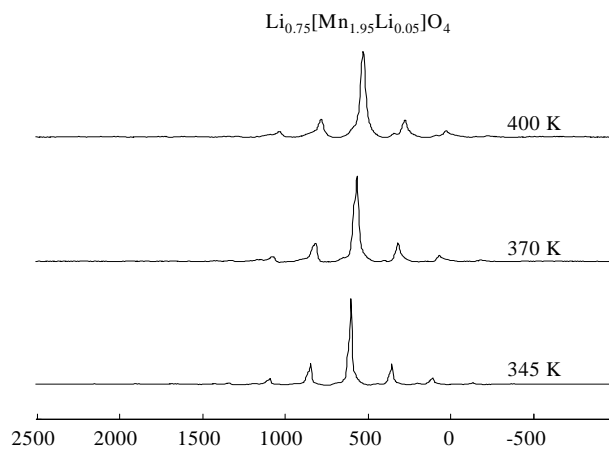


Figure 5.9:  ${}^7\text{Li}$  MAS NMR spectra of  $\text{Li}_{0.75}[\text{Mn}_{1.95}\text{Li}_{0.05}]\text{O}_4$  at temperatures as indicated in the figure. The spinning speed equals 28 kHz.

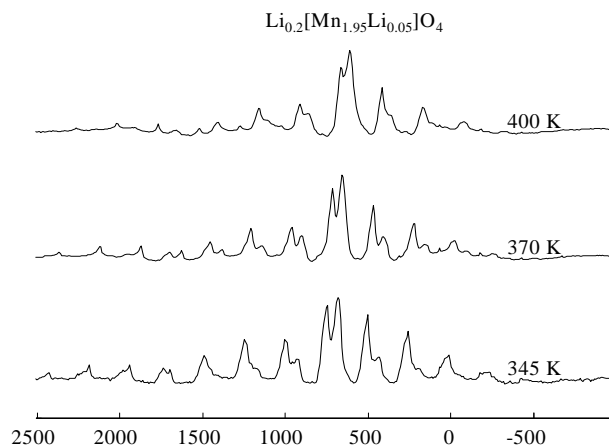


Figure 5.10:  ${}^7\text{Li}$  MAS NMR spectra of  $\text{Li}_{0.2}[\text{Mn}_{1.95}\text{Li}_{0.05}]\text{O}_4$  at temperatures as indicated in the figure. The spinning speed equals 28 kHz.

by quadrupole interactions, since the width of the spectrum (expressed in ppm) measured on a 300 MHz and a 400 MHz set up is the same. The different 8a sites in the unit cell have a different orientation with respect to the static applied magnetic field, resulting in different chemical shifts as is described in [30]. In the MAS spectrum this results in the occurrence of MAS spinning side bands. If now the Li starts hopping between different 8a and \ or 16c, 16d sites sufficiently rapid compared to the homogeneous line width but slower than the distance between the spinning side bands we are in the "slow" exchange regime of paragraph 5.1.6. The Li will contribute to one spinning side band at one instant and to another an instant later. This will effectively lead to life time broadening.

Fitting the central peak with a Lorentzian line shape (since this line shape fits better than a Gaussian line shape) as a function of temperature results in an FWHM of the peak as given in table 5.1. What is observed for this compound in table 5.1 is consistent with motions on a time scale faster than the reciprocal line width (Hz). The line width increases with increasing temperature, which could be caused by motional averaging, in the following way. If we assume that the line-width is dominated by such a motional exchange process, we can determine a time constant of the lithium motion according to  $\frac{1}{\tau} \approx \frac{FWHM}{\sqrt{2}}$ . Values for  $\tau$  are given in table 5.1. In chapter 7 we will show that in  $\text{Li}[\text{Mn}_{1.96}\text{Li}_{0.04}]\text{O}_4$  at 400 K the averaged time constant for the lithium motion is  $\frac{1}{\tau} = 46 \text{ s}^{-1}$ . Calculating a time constant from the line width of the peak of  $\text{Li}_{0.75}[\text{Mn}_{1.95}\text{Li}_{0.05}]\text{O}_4$  at 400 K gives  $\frac{1}{\tau} = 2.5 \cdot 10^3 \text{ s}^{-1}$ . So by extracting 25 % of the lithium from the sample the mobility of lithium increased by a factor of  $\sim 50$ , according to equation (5.53) this means that the concentration of vacancies is increased significantly and \ or the diffusion coefficient  $D_v$  of the vacancies has increased. In view of the diffusion mechanism that will be found in chapter 7, which shows that there are already a large number of empty 8a sites in  $\text{Li}[\text{Mn}_{1.96}\text{Li}_{0.04}]\text{O}_4$ , the larger  $D_{self}$  cannot be explained by a larger [V] alone. Therefore,  $D_v$  has to be significantly larger in  $\text{Li}_{0.75}[\text{Mn}_{1.96}\text{Li}_{0.04}]\text{O}_4$ . This will be due to changes in the electronic structure upon changing the lithium content.

The center of mass of the spectrum is also shifted to larger ppm values (from  $\sim 500$  to  $\sim 900$  ppm, i.e. larger hyperfine fields) which is caused by the larger amount of  $\text{Mn}^{4+}$  in this sample compared to  $\text{Li}_{0.75}[\text{Mn}_{1.95}\text{Li}_{0.05}]\text{O}_4$ .  $\text{Mn}^{4+}$  has a  $\sim 2$  times larger magnetic moment than  $\text{Mn}^{3+}$  in the low spin state (all the  $\text{Mn}^{3+}$  is in the low spin state as will be shown in chapter 6). The larger magnetic moments causes a larger paramagnetic contribution in  $\sigma$  (equation (5.45)).

Table 5.1: The line width of the Lorentzian line shape, fitted to the central line of the  $\text{Li}_{0.75}[\text{Mn}_{1.95}\text{Li}_{0.05}]\text{O}_4$  spectrum at various temperatures and the derived time constants for the lithium mobility.

Temperature (K)	FWHM (Hz)	$\frac{1}{\tau}$ ( $s^{-1}$ )
345	1508	1066
370	2668	1887
400	3480	2461

### $\text{Li}_{0.2}[\text{Mn}_{1.95}\text{Li}_{0.05}]\text{O}_4$

Lithium extracted samples,  $\text{Li}_{0.2}[\text{Mn}_{1.95}\text{Li}_{0.05}]\text{O}_4$ , characterized by ND in the previous chapter show the same crystal structure as the non-extracted samples. NMR characterization was performed at several temperatures. Figure 5.10 shows the spectra of  $\text{Li}_{0.2}[\text{Mn}_{1.95}\text{Li}_{0.05}]\text{O}_4$  as a function of temperature. In contrast with  $\text{Li}[\text{Mn}_{1.95}\text{Li}_{0.05}]\text{O}_4$  and  $\text{Li}[\text{Mn}_{1.95}\text{Li}_{0.05}]\text{O}_4$  we now see two peaks of almost the same intensity as well as an increase of the spectrum width from  $\sim 1500$  ppm to  $\sim 3000$  ppm. The two peaks can be assigned in two ways. 1. Since the lithium from the tetrahedrally 8a sites have been removed the visible peaks can be assigned to the 16c and 16d site. 2. Although all the lithium ions located at the 8a sites have been extracted from the structure, the peaks are assigned to the 8a and 16c site. Since there is lithium exchange between the 8a and 16c site (chapter 7 [27]), part of the lithium ions on 16c site will be at 8a sites after a certain amount of time. The increase of the spectrum width can be caused by the fact that in  $\text{Li}_{0.2}[\text{Mn}_{1.95}\text{Li}_{0.05}]\text{O}_4$  almost all the Mn is in the 4+ state which has a higher magnetic moment as the  $\text{Mn}^{3+}$  in the low spin state, which is the case here [29]. As the magnetic moment is increased the paramagnetic broadening will also have a larger influence, leading to increased spectrum width. One can also observe that the envelope of the spinning sidebands becomes less symmetric. This may indicate a change in the magnetic anisotropic polarisability of the spins. In the next chapter the interaction between the  $\text{Mn}^{4+}$  and  $\text{Mn}^{3+}$  spins is investigated by means of neutron scattering. There will be found that the interaction between the  $\text{Mn}^{4+}$  and  $\text{Mn}^{3+}$  spins is very different in strength. This effect may be responsible for the different chemical shift anisotropy observed in the  $\text{Mn}^{3+}, \text{Mn}^{4+}$  ( $\text{Li}[\text{Mn}_{1.96}\text{Li}_{0.04}]\text{O}_4$ ) and the  $\text{Mn}^{4+}$  ( $\text{Li}_{0.2}[\text{Mn}_{1.96}\text{Li}_{0.04}]\text{O}_4$ ) compounds At 400 K the spectrum width starts to de-

crease which might point at motion of lithium again. The small size of the outer spinning sidebands may cause that any line broadening makes them less visible. In the other samples this has not been observed, but since the lithium sites in this sample are highly unoccupied, the lithium ions will not be obstruct by other lithium ions and therefore it will be more mobile in this sample than in the other two.

All the spectra, shown in Figures 5.8, 5.9 and 5.10, shift to smaller ppm values, i.e. smaller hyperfine fields when the temperature is increased (see table 5.2). This was analyzed in refs. [30] and [31] as the effect of the paramagnetic susceptibility changing proportional to  $\frac{1}{T}$ . In the case of a paramagnetic material a change in temperature will result in a change of the number of unpaired electrons that align themselves parallel to the magnetic field, which leads to a small change in the local magnetic field, resulting in a shift of the spectrum. Increasing the temperature will result in a decreased number of aligned unpaired electrons, therefore the local magnetic field will decrease leading to a shift of the spectrum to smaller precession frequencies.

Table 5.2: The Chemical shift of the peak assigned to the 8a sites of  $\text{Li}_x[\text{Mn}_{1.95}\text{Li}_{0.05}]\text{O}_4$  at 345 K and the averaged shift of this peak (Curie-Weiss behaviour).

$x$	CS (8a-site) (ppm)	$\frac{\Delta CS}{\Delta \frac{1}{T}}$ (ppm·K)
1	489	117500
0.75	594	180000
0.2	–	130000

### 5.3 Results and Discussion

The NMR experiments on  $\text{Li}[\text{Mn}_{1.95}\text{Li}_{0.05}]\text{O}_4$  are in good agreement with crystallographic data from literature [26] that neutrons give: lithium is located at the 16c and 8a site. The 8a and 16c site are clearly visible, unfortunately the 16d and 8a site are overlapping making the 16d site poorly visible for these samples. Extracting 25% of the lithium results in a shift of the spectrum to larger hyperfine fields which can be explained by the increased amount of

$\text{Mn}^{4+}$ . Contrary to the spectrum of  $\text{Li}[\text{Mn}_{1.95}\text{Li}_{0.05}]\text{O}_4$  we now observe only one resonance, which is broadened and has a lorentzian shape. This is probably caused by an increased lithium mobility which is corroborated by the increasing line width as a function of temperature. Extracting even more lithium results in a totally different spectrum. First, the spectrum width is doubled, attributed to the fact that all the  $\text{Mn}^{3+}$  changed into  $\text{Mn}^{4+}$  which has a larger magnetic moment. Second, two peaks can be observed again which have both almost the same intensity. At this moment it is not clear yet to which sites the peaks can be assigned. Finally all spectra shift to smaller ppm values as the temperature is increased, which is caused by the paramagnetic susceptibility changing proportional to  $\frac{1}{T}$ .



# Chapter 6

## Quasi Elastic Neutron Scattering

Quasi elastic neutron scattering (QENS) gives information about the dynamics in the sample. The theory of qens and the experimental results will be discussed in this chapter.

### 6.1 Theory

In chapter 2 the double differential cross section was given by

$$\frac{d^2\sigma}{d\Omega dE_1} = \frac{k_1}{k_0} \sum_{n_0\sigma_0} p(n_0)p(\sigma_0) \sum_{n_1\sigma_1} | \langle \sigma_1 n_1 | \sum_i b_i e^{i\mathbf{k}\cdot\mathbf{R}_i} | n_0\sigma_0 \rangle |^2 \cdot \delta(\hbar\omega - E_0 + E_1) \quad (6.1)$$

In contrast with chapter 2 we will now work this expression out in the case that there is energy transfer between the neutron and the sample.

First we will transform  $dE_1$  into  $d\omega$  using  $E_1 = \hbar\omega$ , this results in

$$\frac{d^2\sigma}{d\Omega d\omega} = \frac{k_1}{k_0} \sum_{n_0\sigma_0} p(n_0)p(\sigma_0) \sum_{n_1\sigma_1} | \langle \sigma_1 n_1 | \sum_i b_i e^{i\mathbf{k}\cdot\mathbf{R}_i} | n_0\sigma_0 \rangle |^2 \cdot \delta\left(\omega - \frac{E_0 + E_1}{\hbar}\right) \quad (6.2)$$

The  $\delta$ -function can be written as a Fourier-integral in time  $t$

$$\delta\left(\omega - \frac{E_0 - E_1}{\hbar}\right) = \frac{1}{2\pi} \int_{-\infty}^{+\infty} dt e^{i\left(\omega - \frac{E_0 - E_1}{\hbar}\right)t} \quad (6.3)$$

this results in

$$\begin{aligned} \frac{d^2\sigma}{d\Omega d\omega} &= \frac{k_1}{k_0} \frac{1}{2\pi} \int_{-\infty}^{+\infty} dt e^{i\omega t} \sum_{n_1} \sum_{n_0} p(n_0) p(\sigma_0) \\ &\cdot \langle n_0 \sigma_0 | \sum_i b_i e^{i\mathbf{k}\cdot\mathbf{R}_i} | \sigma_1 n_1 \rangle \\ &\cdot \langle n_1 \sigma_1 | e^{\frac{iE_1 t}{\hbar}} \sum_i b_i e^{-i\mathbf{k}\cdot\mathbf{R}_i} e^{-\frac{iE_0 t}{\hbar}} | \sigma_0 n_0 \rangle \end{aligned} \quad (6.4)$$

Using

$$e^{-\frac{iE_0 t}{\hbar}} | \sigma_0 n_0 \rangle = e^{-\frac{i\hat{H}_s t}{\hbar}} | \sigma_0 n_0 \rangle \quad (6.5)$$

where  $\hat{H}_s$  is the hamiltonian of the sample, equation (6.4) results in

$$\begin{aligned} \frac{d^2\sigma}{d\Omega d\omega} &= \frac{k_1}{k_0} \frac{1}{2\pi} \int_{-\infty}^{+\infty} dt e^{i\omega t} \sum_{n_1} \sum_{n_0} p(n_0) p(\sigma_0) \\ &\cdot \langle n_0 \sigma_0 | \sum_i b_i e^{i\mathbf{k}\cdot\mathbf{R}_i} | \sigma_1 n_1 \rangle \\ &\cdot \langle n_1 \sigma_1 | e^{\frac{i\hat{H}_s t}{\hbar}} \sum_i b_i e^{-i\mathbf{k}\cdot\mathbf{R}_i} e^{-\frac{i\hat{H}_s t}{\hbar}} | \sigma_0 n_0 \rangle \end{aligned} \quad (6.6)$$

Using the Heisenberg operators

$$\hat{O}(r, t) = e^{\frac{i\hat{H}_s t}{\hbar}} \hat{O}(r) e^{-\frac{i\hat{H}_s t}{\hbar}} \quad (6.7)$$

and

$$\sum_{n_1 \sigma_1} | \sigma_1 n_1 \rangle \langle n_1 \sigma_1 | = \hat{1} \quad (6.8)$$

equation (6.6) results in

$$\begin{aligned} \frac{d^2\sigma}{d\Omega d\omega} &= \frac{k_1}{k_0} \frac{1}{2\pi} \int_{-\infty}^{+\infty} dt e^{i\omega t} \sum_{n_1} \sum_{n_0} p(n_0) p(\sigma_0) \\ &\cdot \langle n_0 \sigma_0 | \sum_i b_i e^{i\mathbf{k}\cdot\mathbf{R}_i(0)} \sum_j b_j e^{-i\mathbf{k}\cdot\mathbf{R}_j(t)} | \sigma_0 n_0 \rangle \end{aligned} \quad (6.9)$$

The definition of (2.31) together with

$$\langle e^{i\mathbf{k}\cdot\mathbf{R}_i} e^{i\mathbf{k}\cdot\mathbf{R}_j(t)} \rangle = \sum_{n_0 \sigma_0} p(n_0) p(\sigma_0) \langle n_0 \sigma_0 | e^{i\mathbf{k}\cdot\mathbf{R}_i(0)} e^{-i\mathbf{k}\cdot\mathbf{R}_j(t)} | \sigma_0 n_0 \rangle \quad (6.10)$$

transforms equation (6.9) into

$$\frac{d^2\sigma}{d\Omega d\omega} = \frac{k_1}{k_0} \frac{1}{2\pi} \int_{-\infty}^{+\infty} dt e^{-i\omega t} \sum_{i=1}^N \sum_{j=1}^N \langle b_i b_j \rangle \langle e^{i\mathbf{k}\cdot\mathbf{R}_i(0)} e^{-i\mathbf{k}\cdot\mathbf{R}_j(t)} \rangle \quad (6.11)$$



Due to the fact that the scattering length depends on the orientation of the neutron's spin with respect to the spin of the scattering atom we can define a coherent and incoherent scattering length (as mentioned in chapter 2). The expansion of the term  $\langle b_i b_j \rangle$  give  $\langle b_i b_j \rangle = b_{coh}^2 + \delta_{ij} b_{inc}^2$ . Using  $\sigma_{coh} = 4\pi b_{coh}^2$  and  $\sigma_{inc} = 4\pi b_{inc}^2$ , equation (6.11) can be split into two parts, a coherent part

$$\left( \frac{d^2\sigma}{d\Omega d\omega} \right)_{coh} = \frac{\sigma_{coh}}{4\pi} \frac{k_1}{k_0} \frac{1}{2\pi} \int_{-\infty}^{+\infty} dt e^{-i\omega t} \sum_{i=1}^N \sum_{j=1}^N \langle e^{i\mathbf{k}\cdot\mathbf{R}_i(0)} e^{-i\mathbf{k}\cdot\mathbf{R}_j(t)} \rangle \quad (6.12)$$

and an incoherent part

$$\left( \frac{d^2\sigma}{d\Omega d\omega} \right)_{inc} = \frac{\sigma_{inc}}{4\pi} \frac{k_1}{k_0} \frac{1}{2\pi} \int_{-\infty}^{+\infty} dt e^{-i\omega t} \sum_{j=1}^N \langle e^{i\mathbf{k}\cdot\mathbf{R}_j(0)} e^{-i\mathbf{k}\cdot\mathbf{R}_j(t)} \rangle \quad (6.13)$$

The coherent part contains a sum of  $e^{i\mathbf{k}\cdot\mathbf{R}_i(0)} e^{-i\mathbf{k}\cdot\mathbf{R}_j(t)}$  for all combinations of particles. This term takes into account the correlations between the position of a particle and the position of every other particle, included itself, at different times. It gives therefore interference effects: the sample scatters as a whole. Only repeated distances and joint motions are seen. This explains the name coherent.

The incoherent part is a sum of  $e^{i\mathbf{k}\cdot\mathbf{R}_j(0)} e^{-i\mathbf{k}\cdot\mathbf{R}_j(t)}$  for every particle. This term expresses the correlation between the positions of a particle  $j$  at different times. Thus the incoherent part represents the sum of motions of individual particles.

### 6.1.1 Intermediate and scattering functions

The intermediate function  $I(\mathbf{k}, t)$  is defined as

$$I(\mathbf{k}, t) = \frac{1}{N} \sum_{i=1}^N \sum_{j=1}^N \langle e^{i\mathbf{k}\cdot\mathbf{R}_i(0)} e^{-i\mathbf{k}\cdot\mathbf{R}_j(t)} \rangle \quad (6.14)$$

The scattering function  $S(\mathbf{k}, \omega)$  is defined by

$$S(\mathbf{k}, \omega) = \frac{1}{2\pi} \int_{-\infty}^{+\infty} dt e^{-i\omega t} I(\mathbf{k}, t) \quad (6.15)$$

So that the coherent double differential cross section is

$$\left( \frac{d^2\sigma}{d\Omega d\omega} \right)_{coh} = \frac{N\sigma_{coh}}{4\pi} \frac{k_1}{k_0} S(\mathbf{k}, \omega) \quad (6.16)$$

Similarly the self intermediate function and the incoherent scattering function can be defined as

$$I_s(\mathbf{k}, t) = \frac{1}{N} \sum_{j=1}^N \langle e^{i\mathbf{k}\cdot\mathbf{R}_j(0)} e^{-i\mathbf{k}\cdot\mathbf{R}_j(t)} \rangle \quad (6.17)$$

$$S_i(\mathbf{k}, \omega) = \frac{1}{2\pi} \int_{-\infty}^{+\infty} dt e^{-i\omega t} I_s(\mathbf{k}, t) \quad (6.18)$$

Then the incoherent double differential cross section is

$$\left( \frac{d^2\sigma}{d\Omega d\omega} \right)_{inc} = \frac{N\sigma_{inc} k_1}{4\pi k_0} S_i(\mathbf{k}, \omega) \quad (6.19)$$

### 6.1.2 The harmonic oscillator

When (6.11) is evaluated for a single harmonic oscillator, no difference between coherent and incoherent scattering exists. A single particle has an average scattering length  $b_{av}$  and consequently a average scattering cross-section  $\sigma_{av}$ .

#### Scattering by a classical harmonic oscillator

Consider a particle bound in an one-dimensional parabolic potential well. The force acting on the particle is  $F(t) = Cr(t)$  at time  $t$ , where  $r(t)$  is the position and  $C$  the spring constant. Then the equation of motion for the particle is:

$$M\ddot{r}(t) + Cr(t) = 0 \quad (6.20)$$

with  $M$  the mass of the particle. Solving this differential equation and substituting  $\omega_0 = \sqrt{\frac{C}{M}}$ , gives:

$$r(t) = r_0 \cos(\omega_0 t) + \frac{v_0}{\omega_0} \sin(\omega_0 t) \quad (6.21)$$

The position and velocity at  $t = 0$  are denoted by the subscript 0. The Hamiltonian of the system is:

$$\hat{H}(r_0, v_0) = \frac{1}{2}C|r_0|^2 + \frac{1}{2}M|v_0|^2 \quad (6.22)$$

We evaluate (6.11) for a single harmonic oscillator, which means that the sums disappear. The intermediate function reads  $\langle e^{i(\mathbf{k}\cdot\mathbf{e})r(0)} e^{-i(\mathbf{k}\cdot\mathbf{e})r(t)} \rangle$ . When

we fill in the solution of (6.21), we get

$$I(\mathbf{k}, t) = \left\langle e^{-i\{(\mathbf{k} \cdot \mathbf{e})r_0(\cos(\omega_0 t) - 1) + (\mathbf{k} \cdot \mathbf{e})\frac{v_0}{\omega_0} \sin(\omega_0 t)\}} \right\rangle \quad (6.23)$$

where the unit vector  $\mathbf{e}$  is in the direction of the one-dimensional oscillation. The average can be taken using Boltzmann's Gaussian integrals for every component of  $r_0$  and  $v_0$ . The intermediate function then becomes:

$$I(\mathbf{k}, t) = e^{-\frac{(\mathbf{k} \cdot \mathbf{e})^2}{M\omega_0^2\beta}(1 - \cos(\omega_0 t))} \quad (6.24)$$

With the substitution

$$k_{cl}^{*2} = \frac{(\mathbf{k} \cdot \mathbf{e})^2}{M\omega_0^2\beta} \quad (6.25)$$

we can also write this as:

$$I(\mathbf{k}, t) = e^{-k_{cl}^{*2}} e^{k_{cl}^{*2} \cos(\omega_0 t)} \quad (6.26)$$

Lovesey [32, page 90] discusses the mathematical relation

$$e^{y \cosh(ix)} = \sum_{n=-\infty}^{\infty} e^{inx} I_n(y) \quad (6.27)$$

where  $n$  is an integer and  $I_n(y)$  is a Bessel function of the first kind. Using the substitutions

$$x = \omega_0 t \quad (6.28)$$

$$y = k_{cl}^{*2} \quad (6.29)$$

with

$$\cos(x) = \cosh(ix) \quad (6.30)$$

and (6.15), we obtain the classical solution

$$S_{cl}(\mathbf{k}, \omega) = e^{-k_{cl}^{*2}} \sum_{n=-\infty}^{\infty} I_n(k_{cl}^{*2}) \delta(\omega - n\omega_0) \quad (6.31)$$

Figure 6.1 gives  $S_{cl}(\mathbf{k}, \omega)$  for three different values of  $k_{cl}^*$ . Taking the limit  $k_{cl}^{*2} \rightarrow \infty$ , one obtains an approximation of (6.31). This approximation is a Gaussian with area 1 and half width (i.e. the standard deviation)  $k^*$ . In the figure these calculated Gaussians are plotted as well.

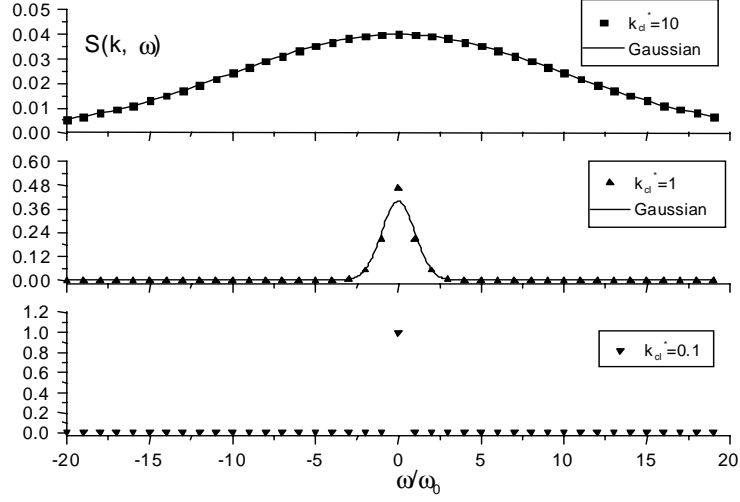


Figure 6.1: The classical treated scattering function  $S_{cl}(\mathbf{k}, \omega)$  for three different values of  $k_{cl}^*$ . Gaussian approximations of  $S_{cl}(\mathbf{k}, \omega)$  are plotted as solid lines.

### Scattering by a quantum-mechanical harmonic oscillator

Consider a particle in a one-dimensional parabolic potential well. The force  $F$  acting on the particle is again  $F = Cr$ . As in the classical case  $C = M\omega_0^2$ . We can write the Hamiltonian  $\hat{H}$  as

$$\hat{H} = \frac{p^2}{2M} + \frac{1}{2}M\omega_0^2 r^2 \quad (6.32)$$

where  $p$  is the momentum,  $r$  the position and  $M$  the mass of the particle. Using the quantum mechanical equivalent of the momentum  $p \rightarrow -i\hbar\nabla$ , the time-independent Schrödinger equation  $\hat{H}\Psi = E\Psi$  becomes:

$$\hat{H}\Psi = \left( \frac{-\hbar^2}{2M}\nabla^2 + \frac{1}{2}M\omega_0^2 r^2 \right)\Psi = E\Psi \quad (6.33)$$

$\hat{H}$  can also be written as:

$$\hat{H} = (a_+ a_- + \frac{1}{2})\hbar\omega_0 \quad (6.34)$$

$$\text{with } a_{\pm} \equiv \frac{1}{\sqrt{2M\hbar\omega_0}} (-i\hbar\nabla \pm iM\omega_0 r) \quad (6.35)$$

The operators  $a_+$  and  $a_-$  are the creation and annihilation operators, respectively. They satisfy

$$[a_-, a_+] = 1 \quad (6.36)$$

Using Heisenberg operators  $a_{\pm}(t) = e^{i\frac{\hat{H}t}{\hbar}} a_{\pm} e^{-i\frac{\hat{H}t}{\hbar}} = a_{\pm} e^{\pm i\omega_0 t}$  (see [32, pages 87 and 88]), the position vector as a function of time is :

$$r(t) = \sqrt{\frac{\hbar}{2M\omega_0}} (a_- e^{-i\omega_0 t} + a_+ e^{i\omega_0 t}) \quad (6.37)$$

Again we will take the intermediate function. From (6.14) and (6.37), one gets

$$I(\mathbf{k}, t) = \left\langle e^{i\sqrt{\frac{\hbar}{2M\omega_0}}(\mathbf{k} \cdot \mathbf{e})(a_- + a_+)} e^{-i\sqrt{\frac{\hbar}{2M\omega_0}}(\mathbf{k} \cdot \mathbf{e})(a_- e^{-i\omega_0 t} + a_+ e^{i\omega_0 t})} \right\rangle \quad (6.38)$$

where the unit vector  $\mathbf{e}$  is in the direction of the one-dimensional oscillation. Substituting

$$k^* = \sqrt{\frac{\hbar}{2M\omega_0}}(\mathbf{k} \cdot \mathbf{e}) \quad (6.39)$$

we obtain:

$$I(\mathbf{k}, t) = \left\langle e^{ik^*(a_- + a_+)} e^{-ik^*(a_- e^{-i\omega_0 t} + a_+ e^{i\omega_0 t})} \right\rangle \quad (6.40)$$

$k^{*2}$  is the energy change of the neutron,  $\frac{(\hbar\mathbf{k})^2}{2M}$ , over the distance between energy levels,  $\hbar\omega_0$ . It measures the energy of the neutron with respect to the energy differences in the sample.

When  $A$  and  $B$  are operators and  $[A, B]$  is a complex number, it holds that [33]:

$$\langle e^A e^B \rangle = \langle e^{A+B} \rangle e^{\frac{1}{2}[A, B]} \quad (6.41)$$

With this result and using  $[a_-, a_+] = 1$  we get

$$I(\mathbf{k}, t) = \left\langle e^{-ik^*(a_-(e^{-i\omega_0 t} - 1) + a_+(e^{i\omega_0 t} - 1))} \right\rangle e^{ik^{*2} \sin(\omega_0 t)} \quad (6.42)$$

Applying the Bloch theorem, valid for any operator  $X = ca_+ + da_-$ , with  $c$  and  $d$  complex numbers:

$$\langle e^X \rangle = e^{\frac{1}{2}\langle X^2 \rangle} \quad (6.43)$$

as derived in [32] gives

$$I(\mathbf{k}, t) = e^{-k^{*2}(1 - \cos(\omega_0 t))} \langle a_- a_+ + a_+ a_- \rangle e^{ik^{*2} \sin(\omega_0 t)} \quad (6.44)$$

Following [33] the average  $\langle a_- a_+ + a_+ a_- \rangle$  can be worked out:

$$\langle a_- a_+ + a_+ a_- \rangle = (e^{\hbar\omega_0\beta} + 1)/(e^{\hbar\omega_0\beta} - 1) = \coth(\frac{1}{2}\hbar\omega_0\beta) \quad (6.45)$$

with  $\beta = 1/(k_B T)$ , where  $k_B$  is the constant of Boltzmann and  $T$  is the temperature. The resulting intermediate scattering function is:

$$I(\mathbf{k}, t) = e^{-k^{*2}} (1 - \cos(\omega_0 t)) \coth\left(\frac{1}{2}\hbar\omega_0\beta\right) e^{ik^{*2}} \sin(\omega_0 t) \quad (6.46)$$

After some mathematics this expression can be written as:

$$I(\mathbf{k}, t) = e^{-k^{*2} \coth(\frac{1}{2}\hbar\omega_0\beta)} e^{k^{*2} \left\{ \frac{\coth(\omega_0(it + \frac{1}{2}\hbar\beta))}{\sinh(\frac{1}{2}\hbar\omega_0\beta)} \right\}} \quad (6.47)$$

Lovesey [32, page 90] showed that

$$e^{y \cosh(x)} = \sum_{n=-\infty}^{\infty} e^{nx} I_n(y) \quad (6.48)$$

where  $n$  is an integer and  $I_n(y)$  is a Bessel function of the first kind. Using the substitutions

$$x = \omega_0(it + \frac{1}{2}\hbar\beta) \quad (6.49)$$

and

$$y = \frac{k^{*2}}{\sinh(\frac{1}{2}\hbar\omega_0\beta)} \quad (6.50)$$

we obtain after taking the Fourier transform:

$$S_q(\mathbf{k}, \omega) = e^{-k^{*2} \coth(\frac{1}{2}\hbar\omega_0\beta) + \frac{1}{2}\hbar\omega\beta} \sum_{n=-\infty}^{\infty} I_n\left(\frac{k^{*2}}{\sinh(\frac{1}{2}\hbar\omega_0\beta)}\right) \delta(\omega - n\omega_0) \quad (6.51)$$

which is the exact solution for  $S(\mathbf{k}, \omega)$  for an harmonic oscillator. Note that  $S_q(\mathbf{k}, \omega)$  is not symmetric in  $\omega$ . It obeys the detailed balance criterion

$$S(-\mathbf{k}, -\omega) = e^{-\hbar\omega\beta} S(\mathbf{k}, \omega) \quad (6.52)$$

which is a direct consequence of the lower occupation of higher energy levels. Figure 6.2a gives a plot of  $S_q(\mathbf{k}, \omega)$  at  $T = 0.001$  K and different values of  $k^*$ . At higher temperatures  $S_q(\mathbf{k}, \omega)$  becomes more symmetric. Figure 6.2b gives a plot of  $S_q(\mathbf{k}, \omega)$  at  $T = 100$  K for three values of  $k^*$ .

### Evaluation of the classical and quantum-mechanical treatment of the harmonic oscillator

We repeat the scattering function of the classical treated harmonic oscillator:

$$S_{cl}(\mathbf{k}, \omega) = e^{-k_{cl}^{*2}} \sum_{n=-\infty}^{\infty} I_n(k_{cl}^{*2}) \delta(\omega - n\omega_0) \quad (6.53)$$

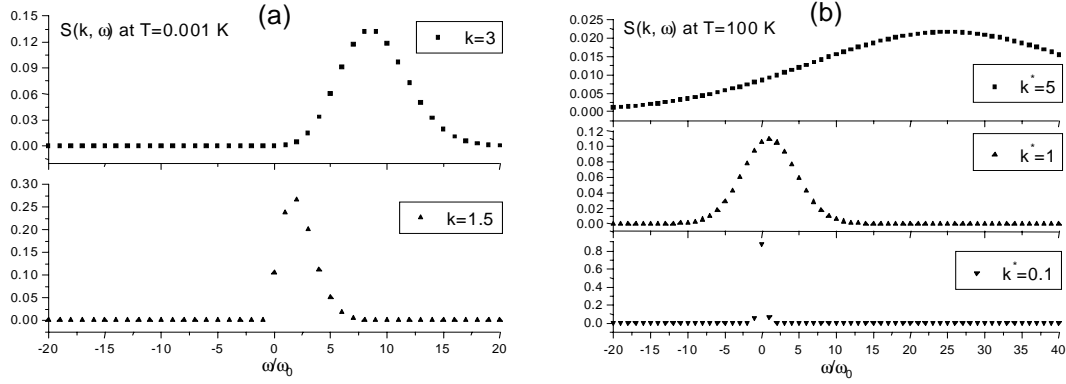


Figure 6.2: The quantum-mechanically treated  $S_q(\mathbf{k}, \omega)$  at  $T = 0.001$  K (a) and at  $T = 100$  K (b) for three different values of  $k^*$ .

and its quantum mechanical equivalent

$$S_q(\mathbf{k}, \omega) = e^{-k^{*2} \coth(\frac{1}{2}\hbar\omega_0\beta) + \frac{1}{2}\hbar\omega\beta} \sum_{n=-\infty}^{\infty} I_n \left( \frac{k^{*2}}{\sinh(\frac{1}{2}\hbar\omega_0\beta)} \right) \delta(\omega - n\omega_0) \quad (6.54)$$

At high temperatures there should be no difference between the two solutions. Let us take  $T$  very high, and thus  $\beta$  very small. With the limits

$$\lim_{x \rightarrow 0} \coth(x) = \frac{1}{x} \quad (6.55)$$

and

$$\lim_{x \rightarrow 0} \sinh(x) = x \quad (6.56)$$

it turns out that the two solutions are similar apart from the factor  $e^{\frac{1}{2}\hbar\omega\beta}$  in  $S_q(\mathbf{k}, \omega)$ . When the energy transfer  $\hbar\omega$  is small this term is also negligible and the two solutions are equivalent. At the position of the peak (see figure 6.2) this approximation is not valid. A shift in the peak position and an asymmetry of the line occurs.

### 6.1.3 Magnetic scattering

At high temperatures every magnetic material behaves like a paramagnet. In a paramagnet the correlation between the directions of adjacent spins vanishes due to the randomizing effect of thermal energy. The differential paramagnetic cross-section is with zero external magnetic field [33]:

$$\frac{d\sigma}{d\Omega} = \frac{2}{3} N (\gamma r_0)^2 \left\{ \frac{1}{2} g F(k) \right\}^2 e^{-2W} S(S+1) \quad (6.57)$$

where  $N$  is the number of atoms,  $\gamma$  is the gyromagnetic ratio,  $r_0$  is the classical radius of the electron:  $(\frac{1}{2}\gamma r_0) = 0.270 \times 10^{-14}$  m is the neutron scattering length per Bohr magneton,  $g$  is the Landé  $g$ -factor (it determines the ratio of the total magnetic momentum to the angular momentum),  $F(k)$  is the magnetic form-factor for the magnetic atoms and  $S$  is the magnitude of the electronic spin angular moment on the magnetic atoms. The factor  $\frac{2}{3}$  arises because the neutron sees only the components of the spins perpendicular to  $\mathbf{k}$ . The magnetic form factor  $F(k)$  dominates the  $k$ -dependence of the signal when the system is paramagnetic. This paramagnetic behaviour is independent on the type of interaction the magnetic moments have: a ferromagnet and an anti-ferromagnet show the same behaviour at high temperatures. However, on cooling down differences between these two types of material develop. In this thesis we will deal only with anti-ferromagnetic interactions.

When the temperature of a frustrated anti-ferromagnet is lowered, the spins condense (i.e. order anti-parallel) and form a spin-liquid. This means that some short range ordering is present. Long-range ordering is absent. In a spin-liquid the orientations of the spins can still change. This means that the neutron which interacts with the spins can exchange energy with the spins, resulting in a quasi-elastic scattering. At even lower temperatures the spins can freeze<sup>1</sup> and one gets a spin-glass in which the spins freeze in short-range ordering, still without long-range ordering. Because the orientations of the spins do not change any more, the neutrons do not have an energy-exchange with the spins in the sample. Therefore magnetic scattering from a spin-glass is completely elastic.

Reimers [34] published about diffuse scattering calculations for frustrated anti-ferromagnets. Following Bertaut and Burlet [35] he introduces the expression for a powder-averaged neutron scattering cross section:

$$\frac{d\sigma}{d\Omega} = \frac{3}{2}(\frac{1}{2}\mu\gamma r_0)^2 \{F(k)\}^2 \sum_{i,j=1}^N \langle \mathbf{S}_i \cdot \mathbf{S}_j \rangle \frac{\sin(kR_{ij})}{kR_{ij}} \quad (6.58)$$

where  $\mu$  is magnitude of the local spin moments, equivalent to the Landé factor  $g$ ,  $\langle \mathbf{S}_i \cdot \mathbf{S}_j \rangle$  is the thermal expectation of the correlation between two spins at sites  $i$  and  $j$  and  $R_{ij} = |R_i - R_j|$  is the distance between sites  $i$  and  $j$ . Using this equation as a starting point we will derive a simple model to describe scattering from anti-ferromagnetic ordered chains in paragraph 6.4.

---

<sup>1</sup>Not all systems are frozen at absolute zero: some systems remain liquid due to zero-point energy. See page 75.



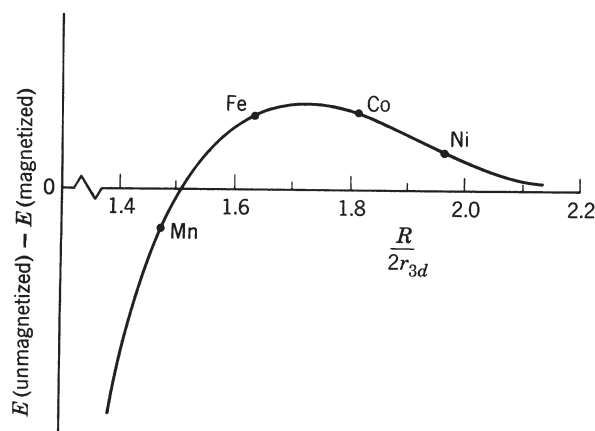


Figure 6.3: The energy difference between unmagnetized (anti-parallel) and magnetized (parallel) alignments of spins as a function of the distance  $R$  between two atoms divided by the radius of the 3d-subshells for some elements.

## 6.2 Magnetic properties

### 6.2.1 Anti-ferromagnetic interaction

The magnetic properties of  $\text{Li}[\text{Mn}_{2-y}\text{Li}_y]\text{O}_4$  depend fully on the manganese atoms since only manganese has a magnetic moment. Manganese is an element which can have (anti-) ferromagnetic coupling. For a description of the origin of these magnetic couplings see [36]. The interaction is represented by the exchange integral. In figure 6.3 the difference between unmagnetized (anti-parallel) and magnetized (parallel) configurations is plotted, which is a direct measure of the exchange integral. This integral depends on the distance between two atoms in the sense that the coupling between two atoms becomes smaller if they are closer together. Eventually the exchange integral will become negative for short distances. This means that the magnetic moments try to align anti-parallel with respect to each other, resulting in an anti-ferromagnetic ordering. Apart from direct exchange between manganese atoms, also indirect exchange via oxygen atoms can be present, so called super exchange.

The exchange integral is also dependent on the valence and the environment of the Mn-ions in the lattice. The valence of manganese ions in our material is 3 or 4 v.u. (valence unit). The anti-ferromagnetic interaction between two  $\text{Mn}^{3+}$  atoms is larger than between  $\text{Mn}^{3+}$  and  $\text{Mn}^{4+}$  and between  $\text{Mn}^{4+}$  and  $\text{Mn}^{4+}$ . This can be concluded from the paper of Jang et al. [37]. In this paper three different materials have been investigated. Starting

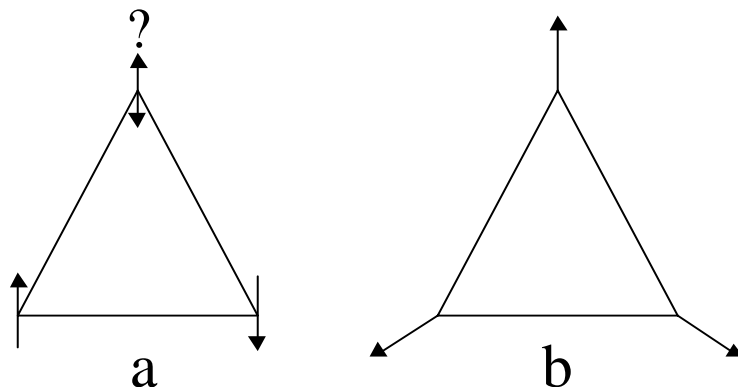


Figure 6.4: The Néel ground state for a two-dimensional spin system.

from  $\text{LiMn}_2\text{O}_4$  they added and extracted lithium. In this way they obtained three materials with basically the same structure, but with Li content varying from 0.07 via 0.98 to 1.87. This also means that the average valence of the Mn ions is 3.97, 3.51 and 3.09 v.u., respectively. The magnetic ordering sets in at different temperatures: at  $T = 16, 25$  and  $60$  K, respectively. The temperature at which such a system orders is a measure of the strength of the interactions. The experiments discussed in this paper suggest that there is more interaction between two  $\text{Mn}^{3+}$  ions than between two  $\text{Mn}^{4+}$  ions.

## 6.2.2 Magnetic frustration

In chapter 2 we already mentioned the magnetic frustration. We will now deal with it again, now in some what more detail.

At high temperatures a system of spins is paramagnetic: there is no correlation between the direction of spins of adjacent atoms. When the temperature is lowered a spin-system can freeze. Freezing of a spin system means that the direction of the spins are more or less fixed, like the position of atoms in a solid are ‘fixed’. In  $\text{Li}[\text{Mn}_{1.96}\text{Li}_{0.04}]\text{O}_4$  the manganese atoms occupy the corners of a network of corner-sharing tetrahedra. Such lattice is normally denoted as a *pyrochlore* lattice. The magnetic moments of the manganese atoms tend to align themselves in an anti-ferromagnetic order. In a pyrochlore lattice there is no configuration in which all atoms can be antiparallel with all other nearest neighbours. This is called spin frustration. The problem of the ordering in such a pyrochlore lattice was considered in 1956 by Anderson [38]. He showed that long-range ordering may only exist

if there are strong interactions on a length scale beyond the nearest neighbours. In fact, very few pyrochlores actually possess such an ordered ground state. For the 2 dimensional case a configuration can be imagined where each spin is oriented at an angle of  $120^\circ$  with respect to each other nearest neighbour. See figure 6.4 in which a picture is given of the solution of the two dimensional frustrated configuration. One speaks of the Néel ground state if an actual spin system freezes in such (although three dimensional) Néel ordering if the temperature is lowered. In this situation long-range ordering exists.

The systems which freeze without long-range ordering are called spin-glasses: below the spin-glass freezing temperature  $T_f$ , all spins freeze in a short-range ordering. Spin-glasses can easily be formed because the Néel configuration is highly degenerate: the energy of the system does not change when all spins rotate and changes very little if *some* spins rotate a bit. Thus due to temperature effects the long-range ordering can easily be destroyed. Another effect is that in every material defects are present which destroy the degeneracy of the ground-state. Consequently the Néel ground-state is a theoretical one. However, short-range anti-ferromagnetic order will still be present. This means that no extra Bragg-peaks will occur in neutron diffraction spectra, but a broad bump, as discussed in chapter 2.<sup>2</sup>

Finally a spin liquid is a system in which the spins do not freeze. Since 1974 several magnetic systems have been investigated experimentally, in a search for real spin liquids. Those spin liquids exist at low temperatures because the zero-point energy is high enough to prevent the spins to freeze, even at  $T = 0$  K. Spin liquids are thus comparable with pure helium, which also does not freeze at normal pressures because of the zero-point energy. Note that applying a high magnetic field can freeze the system because this increases the potential energy of the spins in the system. In the same way helium can be solidified by applying a high pressure (about 26 bar near absolute zero). In these cases the zero-point energy is not high enough to keep the system 'liquid'. For the spin-liquids this experiment has been done by Chen et al. [39].

The sample used in our experiments is frustrated and shows only short-range magnetic ordering according to neutron diffraction results [40]. The material is therefore a spin-glass below the freezing temperature.  $\mu$ SR measurements on this sample give a value of the freezing temperature of  $T_f = 25$  K [22]. Jang et al. [37] also found this freezing temperature. Others however found higher freezing temperatures:  $T_f = 60$  K [41] and  $T_f = 40$  K [42]. As

---

<sup>2</sup>Bragg-peaks do occur when long-range ordering exists, and a broad bump when only short-range ordering is present.

stated above this can well be caused by slight changes in sample composition. Kaiser et al. [22] used the same sample as we did in our experiments.

## 6.3 Experiments

In this section we will describe the instruments on which the experiments were performed, as well as the experiments themselves and the way the data were corrected.

### 6.3.1 RKSII

At IRI an instrument to perform quasi- and inelastic neutron scattering measurements is available. This instrument is called the Roterend Kristal Spectrometer, meaning Rotating Crystal Spectrometer and is called the RKSII. It is placed at a beamline of the 2 MW nuclear reactor at the IRI.

The RKSII uses the time-of-flight (TOF) technique to measure the speed of neutrons. This means that the energy of a neutron is derived from its arrival time (in the detector). When the length of the path the neutron followed is known with sufficient high accuracy, the speed and thus the energy of the neutron can easily be calculated.

Time-of-flight measurements require a pulsed beam to be able to perform measurements of the time-of-flight. Furthermore one needs to know which energy the neutron has when it enters the sample. The rotating crystal which gives the RKSII its name performs the energy selection because of its crystalline state and the pulsing of the beam because it rotates. Every time when a burst of neutrons arrives at the sample they interact with it, possibly resulting in energy loss or gain. These energy differences give rise to a change in speed of the neutrons compared with their original speed. A bank of 75 detectors count the number of neutrons as a function of time and angle. The time of flight of a neutron gives information about the energy transfer between neutron and sample. The scattering angle is a function of the momentum transfer in the sample.

In figure 6.5 an overview is given of the RKSII. Neutrons emitted from the reactor core are approximately thermal. This means that their energy distribution function is as if they were emitted by a reservoir at room temperature.

Let us follow the neutrons through the RKSII. First they pass two choppers C1 and C2 before they hit the rotating crystal X (see figure 6.5). The choppers are discs of a neutron-absorbing material with a gap in it. They rotate at exactly the same frequency as the crystal. The phase of the chop-

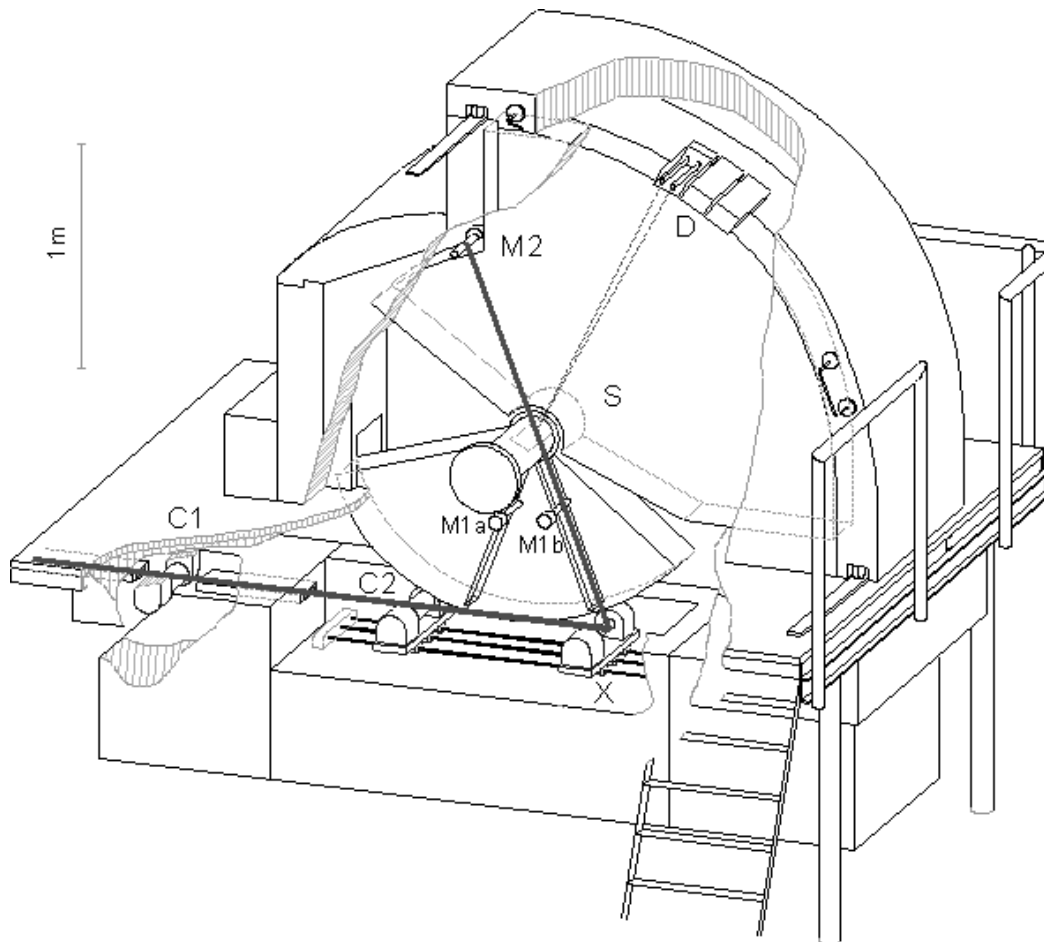


Figure 6.5: A schematic drawing of the RKSII

pers with respect to each other is such that only neutrons within a certain energy range can pass the first *and* the second chopper. This energy range is still too large for accurate TOF, but small enough to suppress –unwanted– higher order reflections of the crystal. Only neutrons within a small energy range are reflected by the crystal.

After reflection at the rotating crystal, the neutrons, which now form a pulsed, mono-energetic beam, pass monitor M1 (in the figure at position M1b). This is a low-efficiency detector, so most of them have no interaction. Then they arrive at the sample container S. Here they can have interaction with the sample or the container which can cause a change in direction or speed. These neutrons can be detected in one of the 75 Helium-filled detectors D. Neutrons which had no interaction, will hit monitor M2.

### Experimental parameters

The hardware of the detector counts the neutrons as a function of time. Time is divided in small time-channels of  $3 \mu\text{s}$  each. Every pulse of the neutron beam is in this way stored in an array of (75 detectors plus 2 monitors is 77) times 512 time channels. The reflecting crystal and the choppers were configured in such a way that they reflected neutrons with a wavelength of  $\lambda = 2.37 \text{ \AA}$ , resulting in a resolution of 0.8 meV. The flight path from sample to the detectors and monitor M2 is 1.503 m.

The container has a slab geometry, with dimensions of 10.4 times 6.2 time  $0.55 \text{ cm}^3$ . In the container we put 57 g of sample for the runs at  $T = 295 \text{ K}$ ,  $T = 150 \text{ K}$  and  $T = 15 \text{ K}$ . The container was filled with 66 g of sample at  $T = 100 \text{ K}$ . This difference was due to another filling method, because the powder had been compacted during the first three runs. To cool down

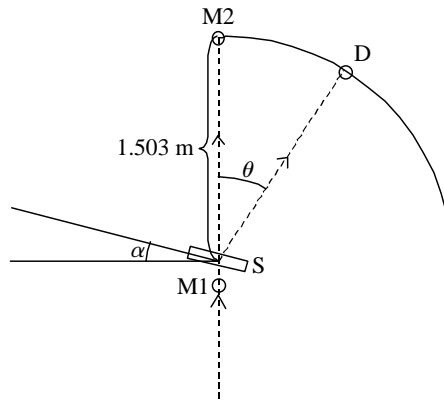


Figure 6.6: The flight path and sample geometry of the RKSII

our sample we used a closed-cycle cryostat (CCR) filled with helium. With this apparatus we could reach temperatures ranging from room temperature down to 15 K. See figure 6.6 for a picture of the flight path and sample geometry. The angle  $\alpha$  was  $13.2^\circ$ . The detector angles  $\theta$  range from  $4.96^\circ$  to  $85.8^\circ$ .

### 6.3.2 IN6

The IN6 spectrometer is located at the institute Laue-Langevin in Grenoble, France. Like the RKSII IN6 uses the Time-of-flight method to measure the energy of the neutron. Again the continuous neutron beam which is coming out of the reactor is chopped and monochromated to get a monochromatic

pulsed beam, necessary for the TOF method. In this case this is not done by a rotating crystal, but by using a fixed monochromator to select a narrow energy range and fermi choppers to make a pulse beam. To detect the neutron 337 elliptical  $^3\text{He}$  detectors are used. In figure 6.7 an overview of IN6 is given.

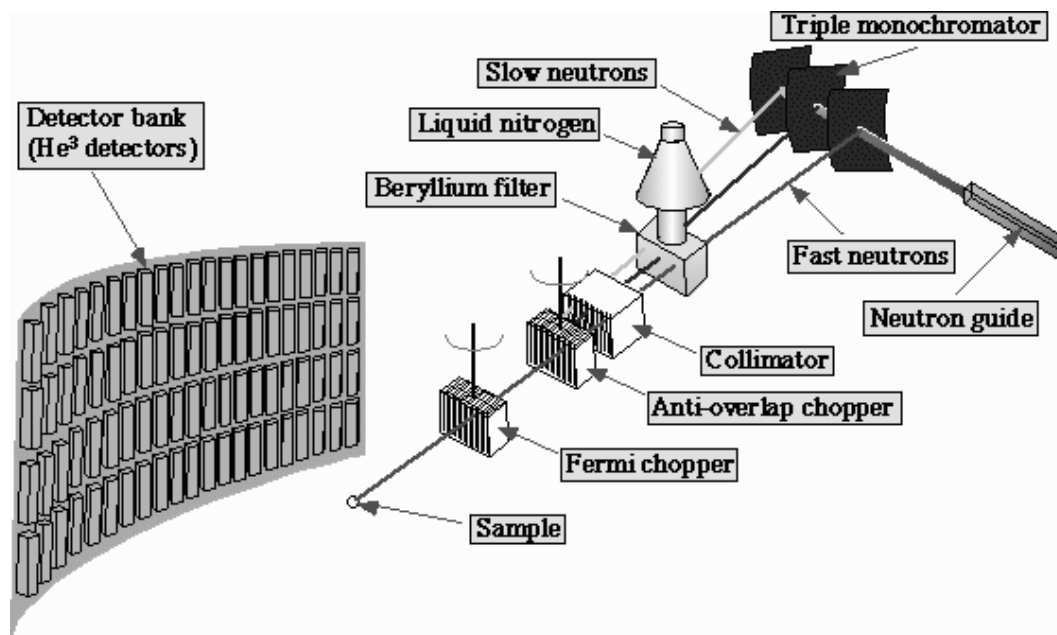


Figure 6.7: A schematic drawing of IN6

### Experimental parameters

The monochromator and the Fermi-choppers were configured in such a way that a pulsed beam of neutrons with  $\lambda = 5.9\text{\AA}$  was created. Using this wavelength of the neutrons resulted in a energy resolution of 0.1 meV. The flight path from sample to the detectors is 2.48 m.

The sample cell which has been used for the experiments was an annulus of 0.2 cm thickness with a radius of 1.4 cm. To control the temperature of the sample we used a orange cryostat, resulting in a temperature range of  $1.5\text{ K} < T < 310\text{ K}$ . The detectors covered a angular range of  $10^\circ < 2\theta < 114^\circ$ . The experiments were performed at 4 K, 10 K, 30 K, 50 K and 70 K.

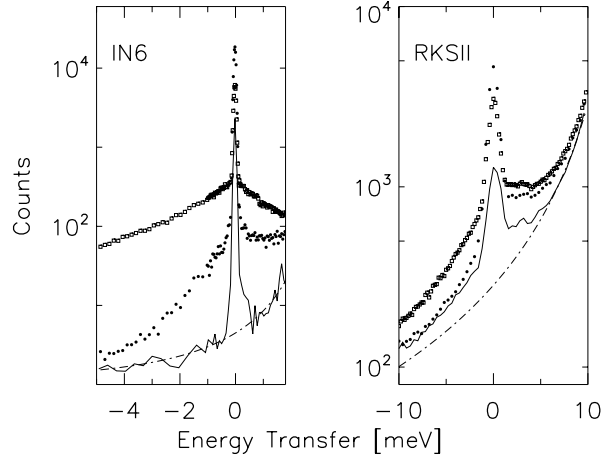


Figure 6.8: Sample uncorrected spectra for  $\text{Li}[\text{Mn}_{1.94}\text{Li}_{0.04}]\text{O}_{3.94}$ , for IN6 and RKSII measurements. Both sets of data are plotted on a log scale. The left half of the figure shows the summed IN6 spectra (scattering angles between  $50^\circ$  and  $55^\circ$ ,  $k \sim 1.1 \text{ \AA}^{-1}$  for the elastic channel) for  $T=10 \text{ K}$  (filled circles) and  $T=70 \text{ K}$  (open squares). Also shown are the corresponding empty container spectra (solid line) and the time-independent background (dotted line). The rise of the time-independent background with energy transfer is due to the (trivial) transformation from time-of-flight to energy transfer. The figure of the right shows equivalent spectra for the RKSII measurement ( $T=25 \text{ K}$  (filled circles),  $T=100 \text{ K}$  (open squares) and empty container (solid line) for scattering angles between  $38^\circ$  and  $42^\circ$ ,  $k \sim 1.8 \text{ \AA}^{-1}$ . Note the continuing presence of inelastic scattering at even the lowest temperatures.

### 6.3.3 Data processing

For both the IN6 and RKSII measurements, sample plus container, empty container and vanadium spectra were recorded. Typical results are given in figure 6.8. Because of the large neutron absorption cross section of the sample, data reduction was slightly more involved than standard. First, all spectra were corrected for the time independent background (the sloping dashed curve in figure 6.8). The relative detector efficiency was determined from the vanadium reference spectra. Vanadium scatters almost completely incoherently (isotropically). Therefore equal amounts of neutrons will arrive at each detector. Comparing the number of detected neutrons of every detector yields the relative detector efficiency. The amount of sample in the



beam was determined from the transmission coefficient. Because of the high absorption cross section of lithium this can be done very accurately. Since the amount of sample in the container will shield the back side of the container from the neutrons, one can not simply subtract the empty container data from the container plus sample data. First one will have to correct the empty container data for self-shielding or self-attenuation. This has been done using standard (numerical) methods [16]. The resultant spectra were then divided by the sample-attenuation factor (absorption factor). Thus, pure sample spectra were obtained, corrected for container and absorption, but uncorrected for instrument resolution and multiple scattering. The latter can be ignored because of the large absorption cross section compared to the scattering cross section. Examples of corrected IN6 and RKSII spectra are shown in figures 6.9 and 6.10.

Finally, in order to ascertain the validity of the above procedures in the presence of large self-attenuation correction factors (of the order of 2-3), we have attempted to put the scattering cross section onto an absolute scale. This was achieved by comparing the transmission ratios of the vanadium and the sample measurements (yielding the ratio of number of sample atoms to number of vanadium atoms), and normalizing to the known in coherent scattering cross section of  $\frac{5.1}{4\pi}$  barn per vanadium atom per steradian. Doing so we found that the amount of incoherent scattering from our sample (which was easily identifiable, see paragraph 6.4.3) was within 20% of the expected amount. Having so demonstrated the validity of the correction procedure. We could then use the absolute intensities for determining the magnetic moments on the  $\text{Mn}^{3+}$  and  $\text{Mn}^{4+}$  ions.

## 6.4 Results and Discussion

We will now give and discuss the results of the experiments on IN6 and RKSII.

### 6.4.1 Corrected data

In figure 6.9 and 6.10 the corrected data is presented in contour plots. The wing starting in figure 6.9 at the Bragg peak at  $k = 2.62\text{\AA}^{-1}$  is believed to be a phonon dispersion curve. In table 6.4.1 values of the slope of the dispersion curve are given, as well as the sound velocities calculated from these slopes.

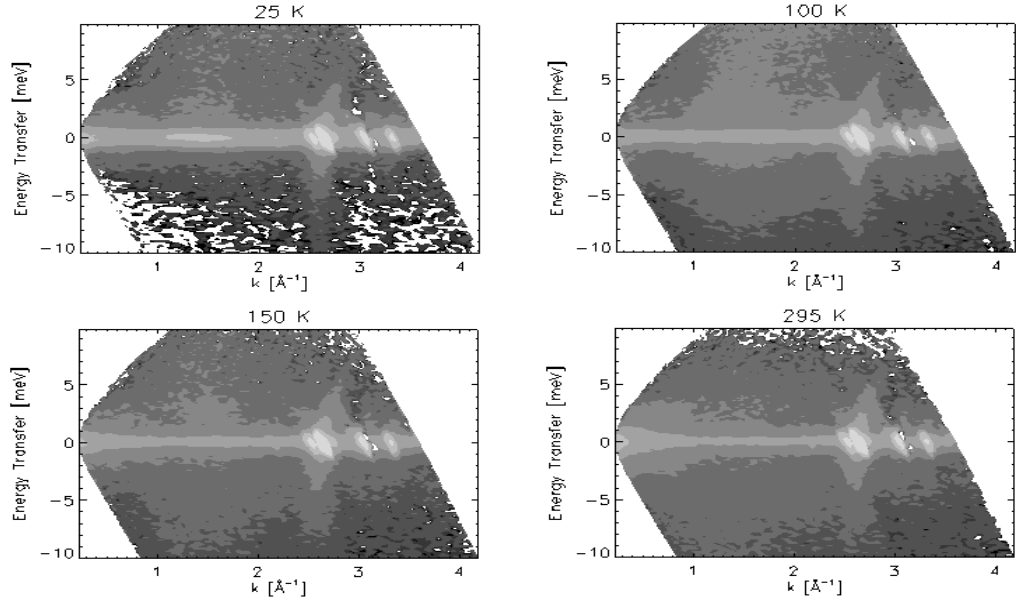


Figure 6.9: Contour plots of the corrected RKSII spectra at temperatures as indicated in the figure. Note the clearly visible Bragg-peaks. The colour scale is not linear.

Temperature [K]	slope [meV/Å <sup>-1</sup> ]	sound velocity [km/s]
15	21.4	3.3
100	22.8	3.5
150	24.8	3.8
295	20.4	3.1

Table 6.1: Slope values of the dispersion curve and sound velocities at four different temperatures.

### 6.4.2 Fit procedure

We can identify three components in the neutron scattering spectra of IN6.

- 1) An elastic component
- 2) A narrow (in energy) inelastic component whose width becomes less than the IN6 resolution function below  $T=30$  K.
- 3) A broad inelastic component, which remains identifiable down to 4 K.

In the neutron spectra of the RKSII only the first and the last component are observable, because of the less good resolution compared to IN6. An example of the three components is given in figure 6.11. These three components make up all of the observed intensity of the neutron scattering spectra. The intensities and widths of the three components have been de-

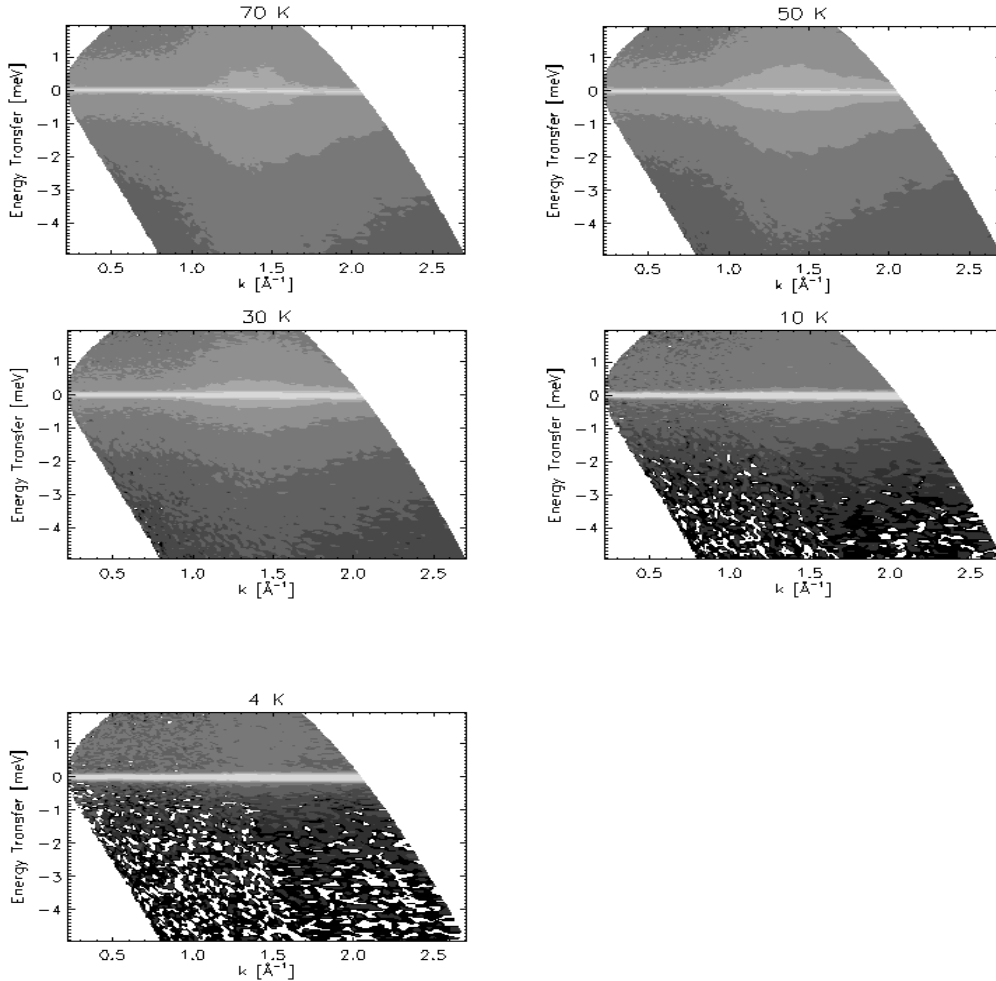


Figure 6.10: Contour plots of the corrected IN6 spectra at temperatures as indicated in the figure. The colour scale is not linear.

terminated through a least squares fitting procedure. In this procedure, we use a resolution limited central line, and two (over) damped harmonic oscillator (DHO) lineshapes, as defined in [43], for the two components that are wider than the resolution function. The DHO-lineshape has the advantage over the lorentzian form used in the literature [44] in that the former has a well-defined area and second frequency moment.

### Damped harmonic oscillator

As explained above the data has been fitted using a resolution limited central line and 1 or 2 damped harmonic oscillator lineshapes in the case of the RKSII and IN6 data respectively. Real data are skew due to the quantum-

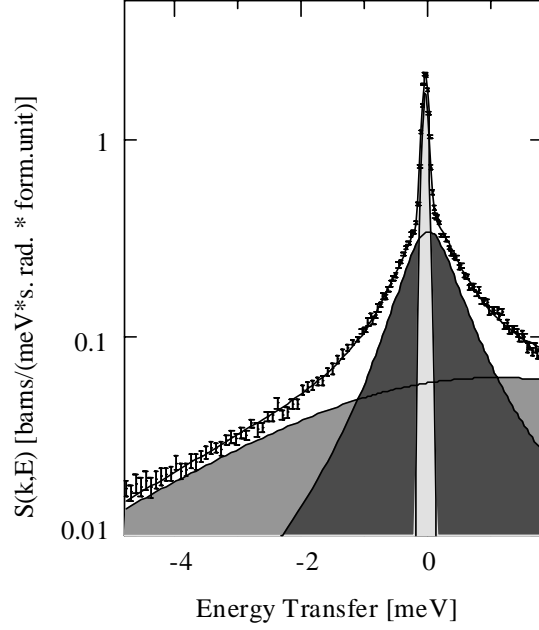


Figure 6.11: Decomposition of the scattered intensity (error bars) for  $k=1.45 \text{ \AA}^{-1}$  and  $T = 50 \text{ K}$  into three components (the dynamic structure factor  $S(k, E)$  is shown on a log scale). The sharp, resolution limited elastic line is given by the incoherent scattering of the sample at this temperature. The broadest component (light grey) remains present down to the lowest temperatures while the narrower component (dark grey) becomes increasingly more narrow with decreasing temperature, and freezes in (i.e. becomes resolution limited) at around  $T = 25 \text{ K}$ . The fit (see (6.60)) to the data is given by the solid line through the data points.

mechanical effects that states with higher energy are less occupied. For that reason we first multiplied the data with the symmetrizing function

$$S_{sym} = S_{skew} \frac{1 - e^{-\beta\hbar\omega}}{\beta\hbar\omega} \quad (6.59)$$

given by Lovesey and by Squires [32, 33]. The fitting formula is:

$$\begin{aligned} S_{fit}(\mathbf{k}, E) &= S_G(k, E) + S_{DHO}(k, E) = \\ &= \left[ \frac{A_g}{w_g \sqrt{\frac{\pi}{2}}} e^{-2\frac{E^2}{w_g^2}} + \frac{\chi_d w_d^2 Z_d}{\pi \{(E^2 - w_d^2)^2 + (Z_d E)^2\}} \right] \end{aligned} \quad (6.60)$$

where  $S_G(k, E)$  and  $S_{DHO}(k, E)$  are the Gaussian and the DHO functions, respectively,  $A_g$  is the area of the central Gaussian,  $\chi_d$  is the static suscep-

tibility of the DHO,  $w_g$  is the “width” of the Gaussian (not the full width at half maximum, but the standard deviation),  $w_d$  the parameter which describes the width of the DHO and  $Z_d$  is the damping factor, which was held constant at 20. One cannot find an analytical solution for the area of a DHO times the symmetrizing function. To get a normalized area of the DHO, the DHO-line was divided by the symmetrizing relation, to make it skew again. Then it was integrated numerically to get its real area  $A_d$ . Especially at the lowest temperature,  $T = 15$  K, the difference between  $\chi_d$  and  $A_d$  was large. To get a real half width at half maximum (HWHM) of the DHO-line we solved the following equation:

$$S_{DHO}(k, E_h) = \frac{1}{2}S_{DHO}(k, 0) \quad (6.61)$$

where  $E_h$  is the energy-transfer at which the DHO is at half maximum (thus  $E_h$  is the HWHM). Solving this equation gives:

$$E_h^2 = w_d^2 - \frac{1}{2}Z_d^2 \pm \frac{1}{2}\sqrt{(Z_d^2 - 2w_d^2)^2 - 4w_d^4} \quad (6.62)$$

provided that  $w_d$  is not equal to 0 and the DHO has its maximum at  $E = 0$  meV. The latter is always true when  $Z_d = 20$  (checked numerically). Substituting  $Z_d$  and using the positive root, which is correct for  $w_d < \frac{1}{\sqrt{2}}Z_d = 10\sqrt{2}$ , one reads

$$E_h = w_d^2 - 200 + \frac{1}{2}\sqrt{(400 - 2w_d^2)^2 - 4w_d^4} \quad (6.63)$$

A fit procedure optimizing the least squares criterion was used to fit the data. Figures 6.12 and 6.13 shows that equation (6.60) fits the data reasonably well. This is also illustrated by the fact that the value of  $\chi^2$ , which is defined as the average of the deviation divided by the error, is generally between 1 and 2 (ideally it should be one). The measurement at  $T = 100$  K has values of  $\chi^2$  round 3. At two points the experimental details of this measurement differ from others: a) two runs were added, resulting in better counting statistics and b) this run had more sample in the sample-chamber, giving a slightly lower transmission. A physical difference is that the intensity of the broad line is largest at this temperature. The high  $\chi^2$ -value is an indication that the broad line is not exactly a DHO, but has another line shape.

### Magnetic model

Magnetic scattering in the material investigated in this thesis is completely caused by manganese atoms. Oohara, Sugiyama and Kontani [44] propose a system in which the spins are anti-ferromagnetically ordered in a chain. Such

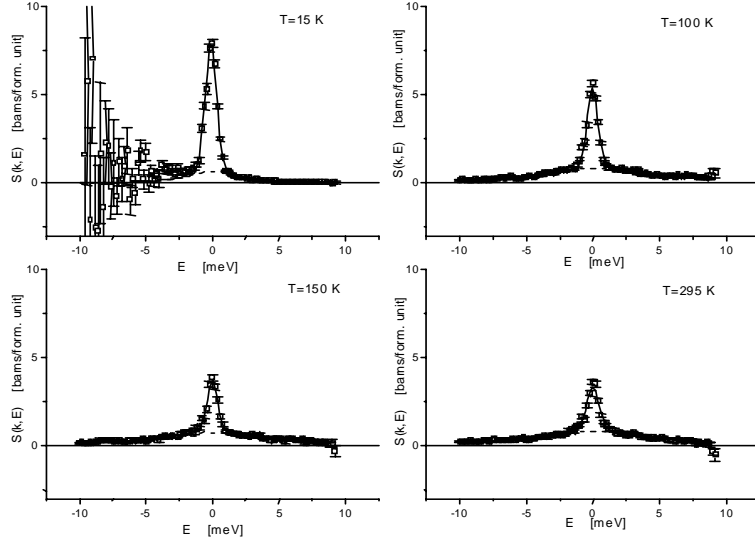


Figure 6.12: Spectra as function of energy transfer at  $\mathbf{k}=1.0 \text{ \AA}^{-1}$ . The solid line is the fit using (6.60). The dashed line shows the contribution of the Damped Harmonic Oscillator. The large deviations at the left-hand side of the spectrum at  $T = 15 \text{ K}$  are due to the symmetrization (equation (6.59)).

a chain is not linear, but looks like a random walk between the positions of the manganese atoms in the material. They assume that there is charge-ordering. Meaning that a Mn-atom has a valence of 3 v.u. or of 4 v.u., but not a average valence of 3.5 v.u. In fact, Rodríguez-Carvajal et al. [19] found that the charges in stoichiometric  $\text{LiMn}_2\text{O}_4$  become localized below 290 K. Furthermore they assume that there is no coupling between  $\text{Mn}^{3+}$  and  $\text{Mn}^{4+}$ . Each of the two sorts of manganese atoms forms a chain. These chain are believed to be independent of every other chain. Therefore only single chains are studied. It is assumed that within a chain  $\langle \mathbf{S}_0 \cdot \mathbf{S}_i \rangle = (-1)^i S^2$ , where  $i = 0$  denote the first atom in the chain. In this way the spins are alternately up and down, resulting in a anti-ferromagnetically ordered chain. Using (6.58) Oohara et al. [44] obtained in this way the following expression

$$\frac{d\sigma}{d\Omega} \propto \left\{ \left( \frac{1}{2} g S_{3+} F_{3+}(\mathbf{k}) \right)^2 + \left( \frac{1}{2} g S_{4+} F_{4+}(\mathbf{k}) \right)^2 \right\} g(\mathbf{k}) \quad (6.64)$$

with

$$g(\mathbf{k}) = 1 + 2 \sum_{i=1}^{\infty} (-1)^i \int dr \frac{\sin(\mathbf{k}r)}{kr} P_i(r) \quad (6.65)$$

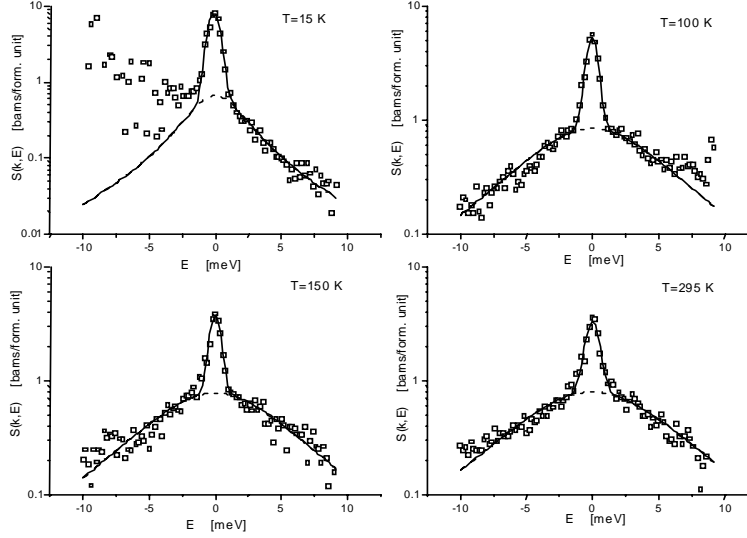


Figure 6.13: Spectra as function of energy transfer at  $\mathbf{k}=1.0 \text{ \AA}^{-1}$  plotted on a log scale. The solid line is the fit using (6.60). The dashed line shows the contribution of the Damped Harmonic Oscillator. The large deviations at the left-hand side of the spectrum at  $T = 15 \text{ K}$  are because some of the points have values smaller than 0, which can not be plotted in a log plot.

where  $P_i(r)$  is the probability to find the  $i^{\text{th}}$  spin at a distance  $r$  from the spin labelled  $i = 0$ . The self correlation is provided by adding one. The term is multiplied with 2 because the chain goes into both directions. The index 3+ and 4+ denote the valence of the manganese atoms. We replace (6.65) with:

$$g(\mathbf{k}) = 1 + 2 \sum_{i=2}^{\infty} \int dr \frac{\sin(\mathbf{k}r)}{\mathbf{k}r} P'_i(r) \quad (6.66)$$

where  $P'_i(r) = (-cor)^{i-1} P_i(r)$  is probability times a scale factor of the spin magnitude. Negative 'probabilities'  $P'_i$  denote an anti-parallel spin  $i$  with respect to the spin with  $i = 1$ . We separated the  $g(\mathbf{k})$  of  $\text{Mn}^{3+}$  and  $\text{Mn}^{4+}$  because we believe that they show completely different behaviour at lower temperatures. We use a standard expression for the magnetic form factor  $F(\mathbf{k})$  of manganese [45]. There is no significant difference between  $F_{3+}(\mathbf{k})$  and  $F_{4+}(\mathbf{k})$  in the  $\mathbf{k}$ -range of our simulation. The parameter  $cor$  serves to simulate the coupling between adjacent spins.

We have written a program which simulates a chain of atoms and calculates  $g(\mathbf{k})$ . The program takes a manganese atom and assigns  $P'_1 = 1$ . Then it makes a random walk with steps of one Mn-Mn distance in such a way that

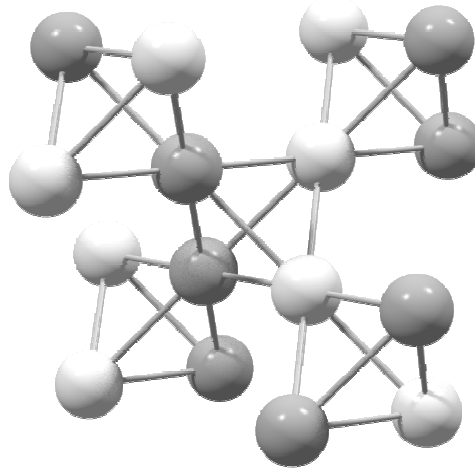


Figure 6.14: The structure of  $\text{Mn}^{3+}$  (dark grey) and  $\text{Mn}^{4+}$  (light grey) ions. The ice-rule is satisfied: every tetrahedron has two of each sort. The ice-rule minimizes the electrostatic energy. Note that one can see chains formed by ions of the same sort.

the ice-rule is satisfied. The ice-rule minimizes the electrostatic energy and says that each tetrahedron of Mn-atoms has two  $\text{Mn}^{3+}$  and two  $\text{Mn}^{4+}$  atoms. Distances to the origin are calculated each step. The number of steps in the random walk is fixed by the chain length  $cl$ . The program repeatedly ( $nc$  times) follows such a random walk and calculates  $P'_i(r)$ . Performing the transformation to  $g(\mathbf{k})$  and substituting in (6.64) gives the simulation result.

When an atom is added to the end of the chain, the parameter  $str$  restricts the position of that appended atom:  $str$  is the minimal amount with which the distance between the last and the first atom in the chain can *increase* in units of the distance between two manganese atoms. It restricts the direction in which the chain can develop and affects the randomness of the random walk. Thus if for instance  $str = 0$ , the chain can not roll up, because it is forbidden that an atom which is added to the chain is nearer to the first atom in the chain than its predecessor. If  $str = 1$  only linear chains are formed. Finally if  $str = -1$ , the chain can have every possible shape, provided that the chain does not touch itself.

There are four parameters which can be varied. These are the correlation between adjacent spins,  $cor$ , how straight the chain is,  $str$ , the chain length  $cl$  and the number of chains  $nc$ . First we will take  $str = -1$ . This means no restriction on the shape of the chain. Further we take  $cor = 1$ , which means that all spins in the chain have the same magnitude. In order to avoid



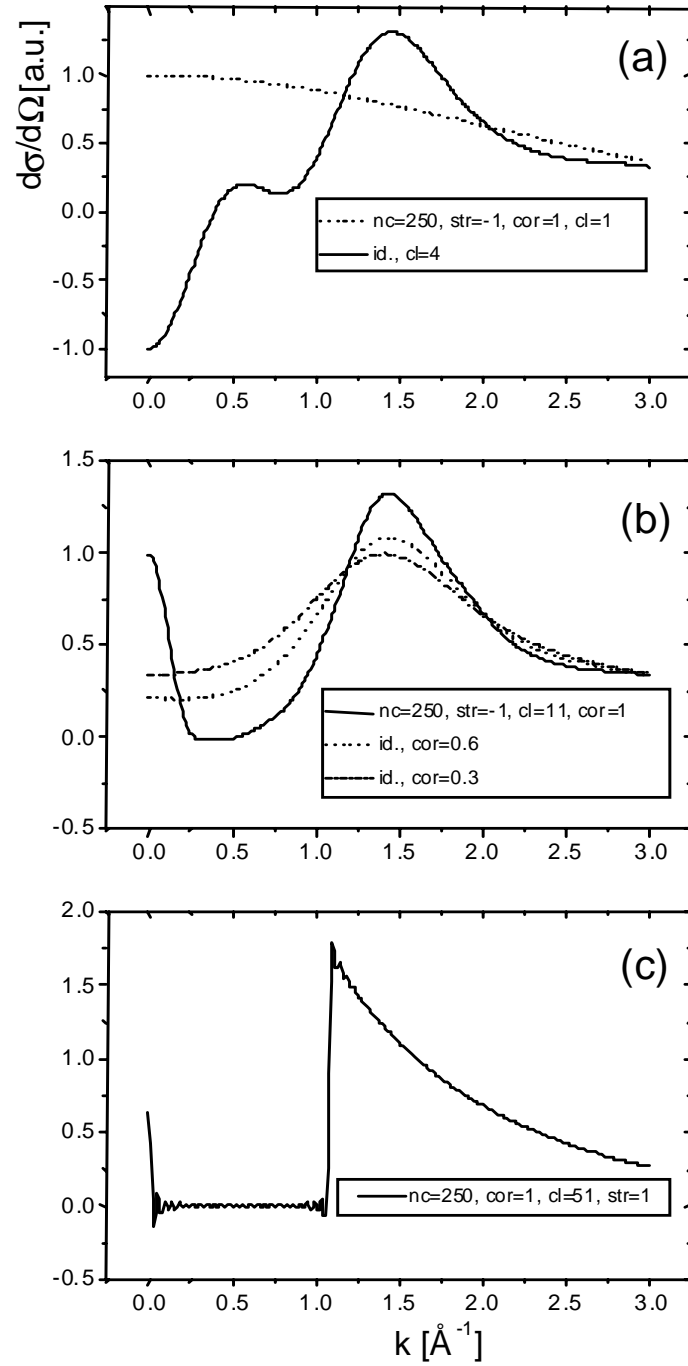


Figure 6.15: Simulations of a frustrated spin system. Parameters are given in the figure.

random outcomes, we take the number of chains,  $nc$ , equal to 250 for all simulations. Taking the chain length  $cl$  equal to one yields  $g(\mathbf{k}) = 1$ . Thus the dashed line in figure 6.15a shows only the magnetic form factor  $F(\mathbf{k})$ . In the case of the solid line the chains have a length of four ( $cl = 4$ ). Note that the simulation equals minus one at  $\mathbf{k} = 0 \text{ \AA}^{-1}$ . Odd values of  $cl$  generate a value of plus one at  $\mathbf{k} = 0 \text{ \AA}^{-1}$ .

When  $cor$  is lower than one, the bump in the simulation result becomes less sharp but the maximum stays at the same position. At the same time, the behaviour at low  $\mathbf{k}$  is more realistic: the line approaches a constant. This constant is higher as  $cor$  approaches zero. The results are almost independent of the length of the chain once  $cor < 1$ . We will take  $cl = 11$ . Plots of the simulation results are shown in figure 6.15b for  $cor = 1, 0.6$  and  $0.3$ , respectively. The result with  $cor = 0$  is exactly the same as that with  $cor = 1$  and  $cl = 1$ , which is already mentioned above. Taking  $cor = 0$  means that all neighbours of the starting atom have spin equal to zero. In this simulation this is the same as if they were not there at all (chain length  $cl = 1$ ).

In figure 6.15c one finds plots of the simulation with the following parameters:  $str = 1$  (the ions form a straight line),  $cor = 1.0$ ,  $cl = 51$  (which is big to achieve smooth results) and  $nc = 250$ .

We will discuss the physical meaning of the cases simulated above, starting with the dotted line in figure 6.15a. In this case only one atom is taken into account ( $cl = 1$ ). Thus there is no correlation with any other atom in the chain. This represents a paramagnet. At high temperatures every magnetic material (ferromagnetic as well as anti-ferromagnetic) is a paramagnet. The solid line in figure 6.15a is the case Oohara et al. mentioned in their paper. It shows the magnetic scattering from small chain of only 4 atoms, with full anti-ferromagnetic correlation between adjacent spins. It does not represent a real system because the chain length is much too small compared with the correlation between adjacent spins.

Plot (b) in figure 6.15 shows three cases in which the correlation varies between 1 and 0.3. As the correlation becomes lower, the line becomes more flat. At  $cor = 0$  we have exactly the same result as the dotted line in 6.15a. These correlations are dependent on temperature: increasing temperatures give less correlation between adjacent spins, because the randomizing effect of temperature destroys the anti-parallel ordering.

Part (c) of figure 6.15 shows the influence of the geometry of a chain. Here  $str = 1$ . This means that *linear* chains are formed with perfect ordering (anti-parallel). Note that in the spinel structure the charge can be ordered in such long linear chains and still obey the ice-rule.

### 6.4.3 Results

#### Dynamics

As mentioned before, the energy resolution for the RKSII measurements is broader than the intrinsic width of the narrow component at low temperatures, so that we fitted the RKSII data to the sum of a Gaussian and a single DHO lineshape. In figures 6.16 and 6.17 the results (pertaining to the magnetic contributions) for the halfwidths and intensities based upon the fitting procedure are given. To obtain pure magnetic intensities the (incoherent) nuclear contribution, as determined from the scattering data at the highest temperatures, was subtracted from the central Gaussian component. While this procedure for removing the nuclear part of the scattering is adequate for most temperatures and  $k$ -values, it does introduce (small) errors for the RKSII data sets at the lowest  $k$ -values. The reason for this is the increased compressibility around the temperature where the charges become localized, which is, unfortunately, the only temperature for the RKSII data sets where we can identify the incoherent scattering as a separate contribution from the magnetic scattering. Therefore, we shall not draw any conclusions from the low- $k$  behavior of the RKSII data sets at the lower temperatures. The IN6 data sets do not suffer from this drawback, since in this case the incoherent background could be determined at  $T=70$  K.

The overall agreement between the IN6 and RKSII data is satisfactory albeit that there are some small differences in the fitting parameters for the broad component. In particular, the broad component in the RKSII measurements appears to carry more intensity than the IN6 data at comparable temperatures ( $T \sim 30$  K). We believe that this is because of the more limited range of energy transfer in the IN6 measurements, making the determination of the parameters for the broad component more cumbersome. We now discuss the three components in detail.

The elastic, incoherent component, representative of the self correlation function of the Li and Mn atoms, is present at all temperatures. The width, related to the diffusivity of the atoms, is less than the resolution width of IN6 at 70 K and of RKSII at room temperature. This implies that neither the Li, nor the Mn atoms move on timescale less than 50 ps at 70 K, and 5 ps at 295 K. For both sets of measurements, the incoherent component is readily identifiable as the remaining elastic scattering at the highest temperatures (see figures 6.9 and 6.10), and does not significantly encumber the analysis of the other two components.

The measured level of incoherent scattering is  $\sim 2.5/4\pi$  barn/(s.rad\*form. unit) for both sets of experiments, while the expected level is some 20% lower

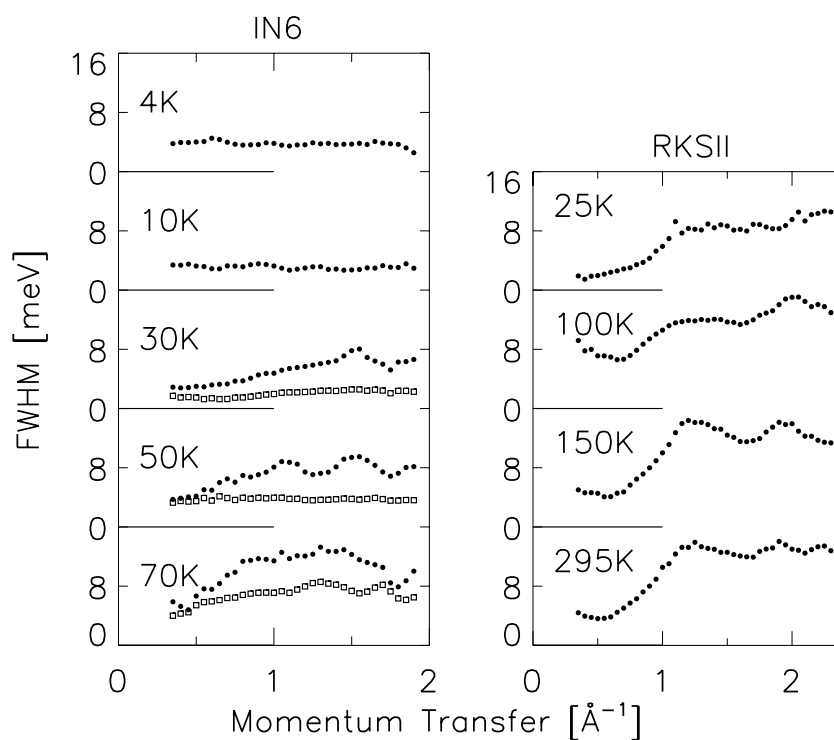


Figure 6.16: The Full Width at Half Maximum (FWHM) of the magnetic components of the scattering by  $\text{Li}[\text{Mn}_{1.94}\text{Li}_{0.04}]\text{O}_{3.94}$  for various temperatures. The width of the broadest component is given by the filled circles, while the width of the more narrow component is given by the open squares. The width of the narrow component has been exaggerated by a factor of 4 for the sake of clarity. Thus, the FWHM of the narrow component at  $T = 50$  K is of the order of 1 meV. The narrow component could only be observed as a separate component in the IN6 measurements.

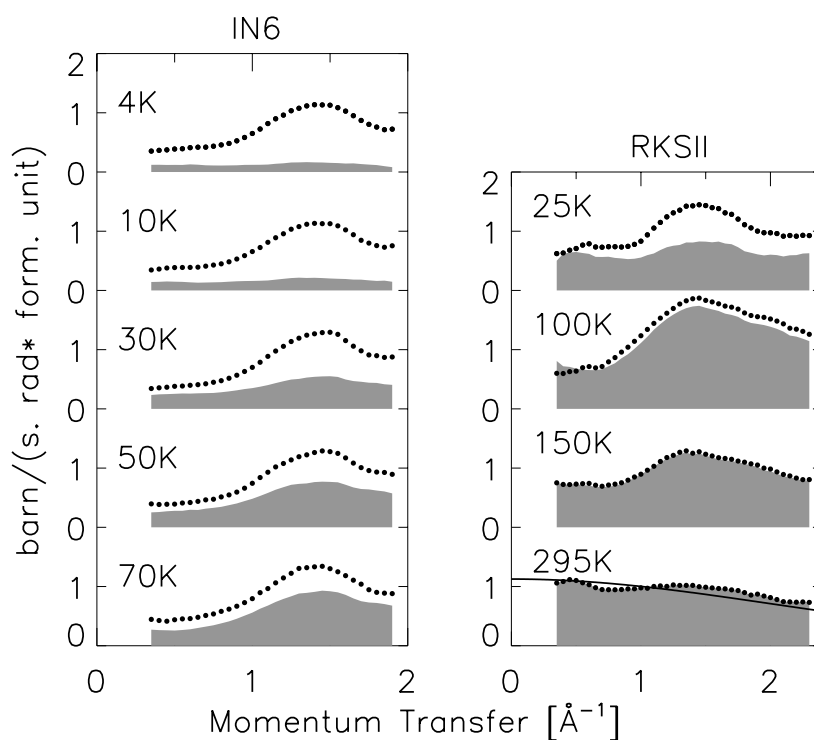


Figure 6.17: The magnetic intensity as a function of momentum transfer for the IN6 and RKSII measurements, for various temperatures given in the figure. The total magnetic intensity is given by the filled circles, while the intensity of the broadest component is depicted by the grey shaded area underneath the curves. The solid line at  $T=295$  K is the expected paramagnetic scattering for  $\text{Li}[\text{Mn}_{1.94}\text{Li}_{0.04}]\text{O}_{3.94}$ , with the  $\text{Mn}^{3+}$  ions in the low spin state.

at  $\sim 2/4\pi$  barn/(s.rad\*form. unit). The latter number is a combination of the incoherent cross sections of the Li and Mn atoms ( $1.72/4\pi$ ), augmented by isotope incoherent scattering to take into account the Li substitution on the Mn sites, and the distribution of the remaining Li over the 8a and 16c sites[19, 42, 40]. Since the absolute intensities of the various components form an essential part of our interpretation, we must look more closely at the implications of this 20% discrepancy.

On the one hand, if the difference is caused by the large correction factors present in our normalization procedure, then this would imply that the absolute intensities of the other two (magnetic) components would also be too high by 20%. This would not present a problem for our interpretation of the results for the other two components, since we will use the fact that the magnetic scattering intensities are already too *low* to allow the  $\text{Mn}^{3+}$  ions to be in the high spin state.

On the other hand, if the absolute level of incoherent scattering is correct, then this has consequences for the sample composition, since the additional incoherence must be caused by oxygen vacancies. Matching the observed incoherent level to the number of oxygen vacancies, we find a 2.4% oxygen vacancy level, yielding a sample composition of  $\text{Li}[\text{Mn}_{1.91}\text{Li}_{0.03}]\text{O}_{3.9}$  (with sample composition  $\text{Li}[\text{Mn}_{1.93}\text{Li}_{0.04}]\text{O}_{3.94}$  at the edge of the errorbars of the incoherent scattering level). In our discussion we show that a sample with oxygen deficiencies does not allow for an interpretation of the  $\text{Mn}^{3+}$ -ions being in the Jahn-Teller active high spin state.

We note that the correction procedures for the IN6 and RKSII data are uncorrelated, so that the fact that we find the same level of incoherent scattering for both data sets is encouraging in that the correction procedures have been carried out more or less correctly, despite the largeness of the attenuation corrections involved.

The 'narrow' inelastic magnetic component becomes increasingly more narrow with decreasing temperature (see figure 6.16), and which freezes out around  $T \sim 25$  K. The momentum dependence of the intensity of this component exhibits a broad maximum near  $k \sim 1.4 \text{ \AA}^{-1}$  (see figure 6.17). In contrast to the study on the parent material [42], no intensity associated with true long range order is observed (i.e. no Bragg peaks were observed). The freezing temperature of 25 K is the same as those reported in refs. [37, 22] for samples of similar composition.

The 'broad' inelastic magnetic component (partially) remains present in the spectra down to 4 K. The continuing existence of spin fluctuations at these low temperatures has been noted before[42, 44]. As with the 'narrow' component, the momentum dependence of the intensity of this component (see figure 6.17) exhibits a broad maximum near  $k \sim 1.4 \text{ \AA}^{-1}$ . At  $T = 295$

K, both the broad and narrow components barely show any structure with momentum, indicating that the response is almost entirely paramagnetic. The total magnetic intensity at  $T = 295$  K is about 1 barn/(s.rad\*form. unit).

The paramagnetic crosssection[33] for uncorrelated spin motions is given by

$$\frac{d\sigma}{d\Omega} = N \frac{2}{3} (\gamma r_0)^2 \left[ \frac{1}{2} g F(k) \right]^2 e^{-2W(k)} S(S+1) \quad (6.67)$$

with  $(\gamma r_0)^2 = 0.291$  barn,  $g$  is the Landé  $g$ -factor [which can be taken to be 2 for both  $\text{Mn}^{3+}$  and  $\text{Mn}^{4+}$ ],  $F(k)$  is the magnetic form factor for the Mn-ions[45],  $W(k)$  is the Debye-Waller factor and  $S$  is the magnitude of the electronic spin angular moment on the  $N$  Mn-ions ( $S = 3/2$  for  $\text{Mn}^{4+}$ ,  $S = 2$  for  $\text{Mn}^{3+}$  in the high spin state, and  $S = 1$  for  $\text{Mn}^{3+}$  in the low spin state). At low  $q$  (i.e.,  $F(k)=1$ ;  $W(k)=0$ ), Equation (6.67) reduces to

$$\frac{d\sigma}{d\Omega} = 0.194 N S(S+1) \text{ barn} \quad (6.68)$$

Thus, every  $\text{Mn}^{4+}$ -ion contributes 0.728 to the paramagnetic cross section, every low-spin  $\text{Mn}^{3+}$ -ion contributes 0.388 and every high spin  $\text{Mn}^{3+}$ -ion contributes 1.164. Other than diamagnetism, the Mn-ions are the only magnetic components of the system. Using the sample composition as given by the average Mn-valency of 3.55 ( $\text{Li}[\text{Mn}_{1.08}^{4+}\text{Mn}_{0.88}^{3+}\text{Li}_{0.04}]\text{O}_4$ ), we find a total paramagnetic cross section of 1.81 barn/(s.rad\*form.unit) with  $\text{Mn}^{3+}$  in the high spin state, and 1.13 barn/(s.rad\*form.unit) with  $\text{Mn}^{3+}$  in the low spin state. The intensity of the magnetic scattering at  $T = 295$  K shows very little  $k$ -dependence (see figure 6.17), indicating that there are no spatial correlations between the individual spin motions (paramagnetic behavior). We plot the paramagnetic response for the low spin state as a solid curve in figure 6.17 (this curve shows the magnetic form factor[45], but not the Debye-Waller factor). Clearly, our results reported in figure 6.17 are consistent with the  $\text{Mn}^{3+}$ -ions being in the low spin state.

Allowing for 2.4% oxygen vacancies (i.e.,  $\text{Li}[\text{Mn}_{1.04}^{4+}\text{Mn}_{0.85}^{3+}\text{Li}_{0.03}]\text{O}_{3.9}$ , see previous chapter), we find 1.77 and 1.10 barn/(s.rad\*form. unit) for the crosssections corresponding to the high spin and low spin configurations, respectively. Again, our results are only consistent with low-spin  $\text{Mn}^{3+}$ -ions. Scaling the observed magnetic intensity to the non-oxygen vacancy level for the incoherent scattering, would lead to an even lower value for the observed paramagnetic scattering. Also note that the overall level of intensity changes by only a small margin on cooling down to 150 K, indicating that our conclusions drawn from the data taken at 295 K are not invalidated by the proximity (in temperature) of the latter to the point where the charges

become localized. Therefore, we conclude that the  $\text{Mn}^{3+}$ -ions in our sample are in the low spin state.

At first glance, it is somewhat surprising to find  $\text{Mn}^{3+}$  in the low spin state, since this has not been reported before in the literature. However, it is known [19, 42] that the Jahn-Teller distortions are very small indeed, and of a more dynamic [42] than static character. Therefore, it could be feasible that small changes in sample composition might thwart the Jahn-Teller distortion completely, leaving the  $\text{Mn}^{3+}$  ions in the low spin state. We draw attention to the study by Young-II Jang *et al.* [37], who determined (from magnetization measurements) an effective Mn spin angular moment of  $(4.05 \pm 0.05)\mu_B$  for a sample of similar composition. This value is consistent with 40% to 50% of the  $\text{Mn}^{3+}$  ions being in the low spin state.

We now discuss the temperature dependence of the linewidths and intensities of the two magnetic components. At the highest temperature ( $T=295$  K), the intensity of the magnetic scattering shows very little  $k$ -dependence (see figure 6.17), indicating that the system is in a paramagnetic state. As mentioned in the preceding, the absolute value of the intensity at this temperature is consistent with the  $\text{Mn}^{3+}$  ions being in the low spin state. The linewidths are very large (FWHM  $\sim 14$  meV, see figure 6.16), showing that the spins fluctuate on time scales of less than 1 ps.

On cooling down, one observes a slightly increased  $k$ -dependence of the magnetic intensities (see figure 6.17), reflecting the increased correlation of the spin fluctuations between neighboring Mn-sites. The time scales associated with the spin fluctuations remain more or less unchanged down to  $T=100$  K (see figure 6.16), while practically all of the scattered intensity is in the broad component. Thus, it appears that both  $\text{Mn}^{3+}$  and  $\text{Mn}^{4+}$  ions show similar behavior for  $T > 100$  K. There is barely any correlation between neighboring Mn ions, indicating that the temperature is higher than any of the Mn-Mn exchange interactions present.

However, on cooling down further, we start to observe a difference in behavior between the  $\text{Mn}^{3+}$  and  $\text{Mn}^{4+}$  ions. While the linewidth of both the broad and narrow components decreases, the linewidth of the narrow component decreases much faster and becomes resolution limited for temperatures below  $T=30$  K. Meanwhile, the linewidth of the broad component is still of the order of 2 meV down to the lowest temperature. This shows that the system has both spins that are frozen in, and spins that are still free to fluctuate at the lowest temperatures.

The most obvious (but possibly fallacious) explanation for this is a difference in exchange integrals between the  $\text{Mn}^{3+}$ - $\text{Mn}^{3+}$ ,  $\text{Mn}^{3+}$ - $\text{Mn}^{4+}$  and  $\text{Mn}^{4+}$ - $\text{Mn}^{4+}$  ions, resulting in different freezing temperatures for the  $\text{Mn}^{3+}$ - $\text{Mn}^{3+}$  and the  $\text{Mn}^{4+}$ - $\text{Mn}^{4+}$  spin fluctuations. Judging by the fact that the narrow



component at the time of freezing-in carries most of the intensity, we are led to believe that this component is representative of the  $\text{Mn}^{4+}$  spin fluctuations. The freezing temperature of  $T \sim 25$  K is consistent with that reported in the literature [22], and consistent with the fact that  $T_g$  decreases [41] with increasing Li-substitution. Previous neutron scattering studies [44] lacked the energy resolution required to observe the presence of two components to the magnetic scattering. These results were interpreted as the spins partly freezing in, with some of the spin fluctuations persisting down to low temperatures. The present results clearly show that the freezing temperature is well defined for one type of spin fluctuations, which we have tentatively identified with the  $\text{Mn}^{4+}$  spin scattering.

Another interesting aspect of the data is the behavior of the halfwidth of the two components at low temperatures (see figure 6.16). While at high temperatures the linewidth shows a distinctive  $k$ -dependence (rapid increase at low  $k$ -values until it reaches a saturation value at  $k \sim 1 \text{ \AA}^{-1}$ ), at low temperatures (30 and 50 K for the narrow component, and 4 and 10 K for the broad component, respectively) the halfwidth does not depend on  $k$  in the region  $0.4 < k < 2 \text{ \AA}^{-1}$ . This implies that long wavelength spin fluctuations are just as long lived as short wavelength fluctuations. This lack of an obvious lengthscale is what one could expect for a system near a phase transition. At present, we have no explanation for the oscillations observable in the halfwidth of the broad component, such as can be seen in Fig. 6.16 at  $T = 50$  and 150 K.

### Magnetic structure

The momentum dependence of the magnetic intensity yields information about the underlying charge-ordering. The total magnetic intensity is displayed in figure 6.18. Clearly, we do not observe any Bragg peaks associated with three dimensional long-range order. As pointed out by Oohara *et al.* [44] and the simulation results in figure 6.15, organization of the charges into linear chains of either  $\text{Mn}^{3+}$  or  $\text{Mn}^{4+}$  ions would lead to the observation of a step function in the scattered intensity at  $k = \pi/d_{\text{Mn-Mn}} = 1.08 \text{ \AA}^{-1}$ , i.e., determined by the Mn-Mn distance  $d_{\text{Mn-Mn}}$  in a tetrahedron. This is not observed in our data plotted in figure 6.18.

Fitting the data to the model of manganese ions ordered magnetically in non-linear chains, as defined in paragraph 6.4.2, results in the fits displayed in figure 6.18. Figure 6.18 clearly shows that despite the simplicity of the model it describes the data very well. The parameter *cor* which was not included in the model of Oohara improves the fit considerably and it also gives useful information about the strength of the magnetic ordering. Table 6.2

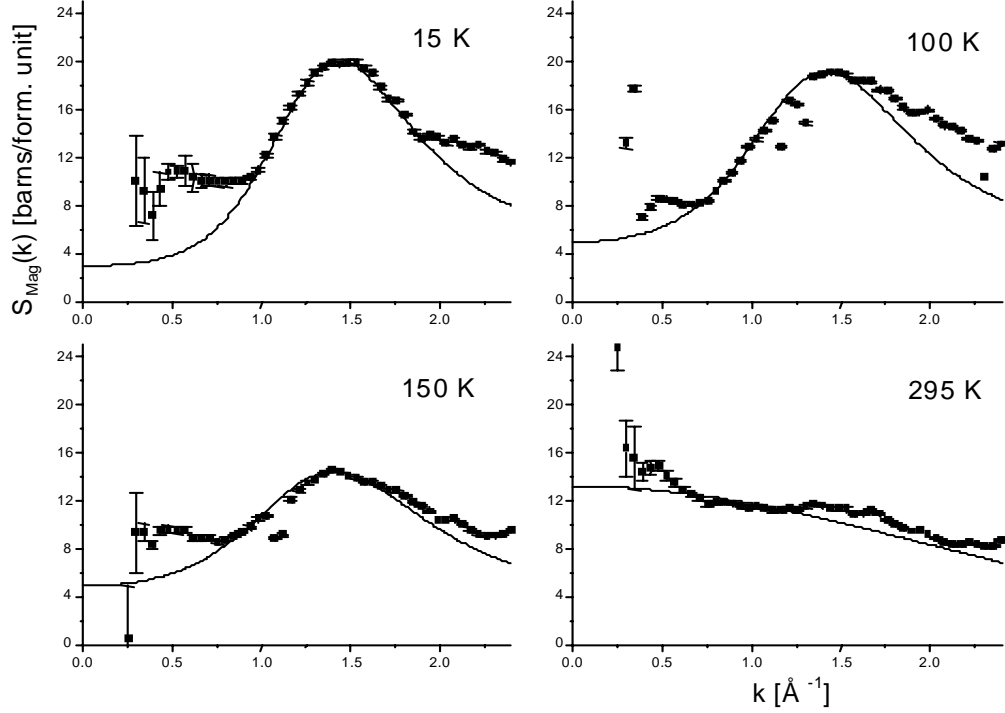


Figure 6.18:  $A_{tot}$  as a function of  $\mathbf{k}$  for (a)  $T = 15$ , (b) 100, (c) 150 and (d) 295 K. The lines are the results of the model of which the parameters are given in table 6.2.

shows that  $cor$  decreases when the temperature increases, meaning that the correlation between neighboring spins becomes less at higher temperatures, which is exactly what one expects. At room temperature the interaction between neighboring spins is completely overruled by the thermal energy of the spins, leading to a zero correlation between the spins as is the case in a paramagnetic material.

#### 6.4.4 Discussion

##### Magnetic structure in the paramagnetic regime

Above  $T_f$ , the temperature at which the spins freeze, the scattering becomes paramagnetic. We say that a system of spins is paramagnetic when the direction of a spin is not correlated to any other spin. The higher the temperature the better this description is. At the highest measured temperature, 295 K, the dependence of the magnetic scattering on the momentum transfer (figure

Table 6.2: Parameters used in the simulations plotted in figure 6.18. The other parameters had the following values:  $str = -1$ ,  $cl = 21$  and  $nc = 250$ .

$T$ [K]	15	100	150	295
$Ampl$	18.0	18.5	14.5	13.2
$cor$	0.7	0.6	0.5	0.0

6.16) shows that the spins in the sample are almost entirely paramagnetic. It is expected that the magnetic scattering as function of momentum transfer approaches the predicted paramagnetic line even better at temperatures higher than 295 K.

In the chapter 4 we argued that a Jahn-Teller structural phase change cannot occur when the  $Mn^{3+}$  ions are in the low spin state. The conclusion drawn here that the  $Mn^{3+}$  ions are in the low spin state is consistent with the result of neutron diffraction experiments on the same material, where no Jahn-Teller transition was found [40].

#### Magnetic structure just above $T_f$

On decreasing the temperature, the spins directions of neighbouring atoms get more and more correlated. At  $T = 150$  K,  $T = 100$  K for the RKSII measurements and  $T = 70$  K,  $T = 50$  K,  $T = 30$  K for the IN6 measurements we see a large magnetic signal which is strongly dependent on the momentum transfer  $\mathbf{k}$ . The bump in the signal near  $k = 1.4 \text{ \AA}^{-1}$  indicates that short range ordering is present. The intensity of this signal can successfully be described by the simple model described in paragraph 6.4 in which non-linear chains of manganese ions are proposed. The values of the parameter  $cor$ , 0.5 at 150 K and 0.6 at 100 K as given in table 6.2, indicate that spins order anti-ferromagnetically at a range of a few times the distance between two manganese atoms. The half widths at half maximum which can be calculated from  $cor$ , are 1 at 150 K and 1.3 at 100 K in units of the distance between two manganese atoms. At these two temperatures the  $Mn^{4+}$  and the  $Mn^{3+}$  ions are indistinguishable for neutron experiments.

#### Magnetic structure below $T_f$

Below the freezing temperature (which is at  $T = 25$  K [37, 22]), part of the spins is frozen, while another part is still free. We think the most plausible explanation of the two different phases is that the valence of the Mn ion

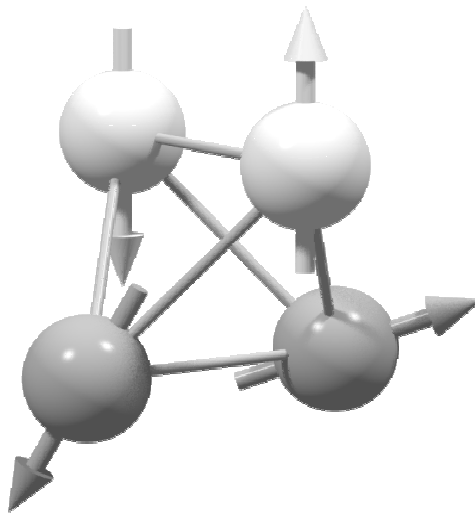


Figure 6.19: The magnetic structure below  $T_f$ , with free spins of  $\text{Mn}^{3+}$  (dark grey) and frozen ones of  $\text{Mn}^{4+}$  (light grey).

determines whether it freezes or not. Because  $S(S + 1)$  of the two type of Mn differs by a factor of 1.9, the neutron scattering experiments discussed here should be able to say which type of Mn freezes first. As can be seen in figures 6.16 and 6.17, the intensity of the frozen component is only about 10% larger than the intensity of the free component. This is much less than the factor of 1.9 we would expect to see if  $\text{Mn}^{4+}$  was frozen and  $\text{Mn}^{3+}$  free. Since the sample temperature (25 K) is close to the freezing temperature, not all the  $\text{Mn}^{4+}$  will have been frozen already, resulting in a smaller difference between the frozen and free component than the expected factor of 1.9.

From these arguments we regard the spins of the  $\text{Mn}^{4+}$  ions as being frozen and the spins of the  $\text{Mn}^{3+}$  ions as being free to rotate.

Figure 6.19 can serve to demonstrate the configuration at low temperatures. The direction of the spins of the 4+ ions are fixed *and* anti-parallel with respect to each other.

#### 6.4.5 Time-scales of magnetic excitations

Line-widths give information about time scales in the sample. If a certain state exists long, the line width associated with this process will be small. On the other hand, short time scales mean broad contributions to the spectra. It is plausible that we observe spin waves. The width of the line at a

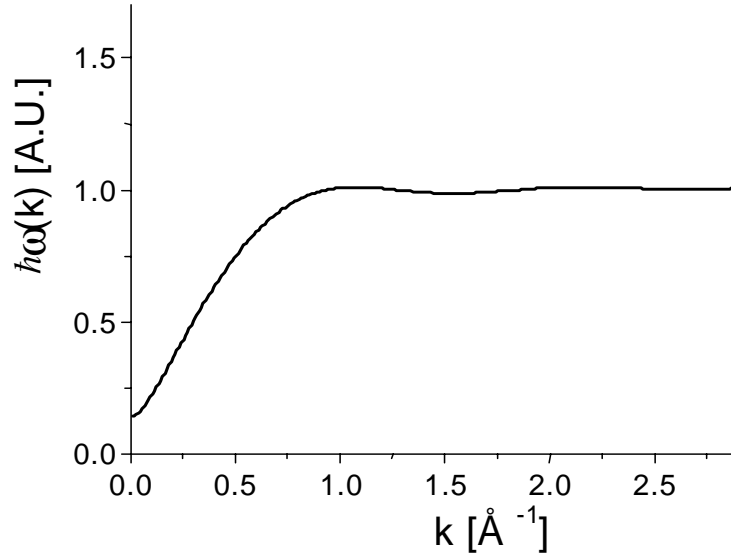


Figure 6.20: The theoretical dispersion relation for the Heisenberg anti-ferromagnet. Note the band gap at small  $k$  due to an anisotropy field.

certain momentum transfer gives information about the time scale at which the wave moves, while the momentum transfer gives information about the wave length associated with the spin wave. The theory which predicts the low-lying spin wave excitation energies of an anti-ferromagnet is rather complex [46]. Lovesey [10] gives the following dispersion relation for the energy  $\hbar\omega(\mathbf{k})$  as function of momentum transfer  $\mathbf{k}$  of magnons in a Heisenberg anti-ferromagnet:

$$\hbar\omega(\mathbf{k}) = 2rJS\sqrt{(1 + h_A)^2 - \gamma(\mathbf{k})^2} \quad (6.69)$$

where he assumes that there is only interaction with the  $r$  nearest neighbours,  $J$  is the Heisenberg exchange parameter or exchange integral,  $S$  is the spin quantum number,  $h_A$  is the reduced anisotropy field and  $\gamma(\mathbf{k})$  is defined as

$$\gamma(\mathbf{k}) = \frac{1}{r} \sum_{\boldsymbol{\rho}} e^{i\mathbf{k}\cdot\boldsymbol{\rho}} \quad (6.70)$$

In this definition  $\boldsymbol{\rho}$  is the set of vectors pointing to  $r$  anti-parallel ordered nearest neighbours and  $\mathbf{k}$  is the scattering vector. In  $\text{LiMn}_2\text{O}_4$ , every Mn atom has 6 nearest Mn neighbours. Because our compound is a powder, we

have an average over all directions of  $\mathbf{k}$ , which can be worked out to [47]:

$$\langle \gamma(\mathbf{k}) \rangle_{\hat{k}} = \left\langle \frac{1}{r} \sum_{\rho} e^{i\mathbf{k} \cdot \rho} \right\rangle_{\hat{k}} = \frac{\sin(k\rho)}{k\rho} \quad (6.71)$$

$\rho$  denotes the distance between two Mn-atoms, which is 2.92 Å[40]. When we paste this result into equation (6.69) and assume a reduced anisotropy field of  $h_A = 0.01$ , we get the result plotted in figure 6.20.

The line width in the experiments discussed here seems to start somewhat above zero at zero momentum transfer. With increasing  $k$ , it grows until it reaches a maximum at  $k = 1.0 \text{ \AA}^{-1}$ . When we compare the theory (figure 6.20) and the experimental line widths (figure 6.16), the theory shows interesting similarities.

## 6.5 Conclusions

The  $\text{Mn}^{3+}$  ions in the material  $\text{Li}[\text{Mn}_{1.96}\text{Li}_{0.04}]\text{O}_4$  are in the low spin state. This suppresses the Jahn-Teller effect. At temperatures below room temperature, short range anti-ferromagnetic correlations between the magnetic moments of manganese ions develop. Cooling down below  $T_f = 25 \text{ K}$  gives a special type of spin-glass in which the spins are partially frozen spin-glass-like and partially free like in a spin-liquid. The spins of the  $\text{Mn}^{4+}$  ions are thought to be frozen, while the spins of the  $\text{Mn}^{3+}$  ions are free. The trend in  $d\sigma/d\Omega$  can more or less be described with a simple model. In this model non-linear chains of Mn ions with anti-ferromagnetic ordering within the chain are supposed.

# Chapter 7

## Two Dimensional NMR

### 7.1 Theory

The theory of NMR in general has been discussed in chapter 5, therefore, the parts of NMR used specifically in two dimensional MAS-NMR will be explained now.

For a more fundamental and precise description of the two-dimensional rotor synchronized MAS-NMR technique we refer to the literature [48, 49, 50, 51].

#### 7.1.1 Pulse sequence

The sequence of pulses used in the two-dimensional MAS-NMR technique is considerably more complex than the pulse sequence used in the one-dimensional MAS-NMR. In figure 7.1 this pulse sequence is shown.

We will now explain the results of the different parts of the pulse sequence by looking at a single spin. The first  $90_y^\circ$  pulse turns the  $^7\text{Li}$  spin perpendicular to the external magnetic field, exactly like the  $90_y^\circ$  pulse in an one dimensional MAS-NMR experiment. After this pulse the spin will precess around the magnetic field. After a time  $t_1$  a  $-90_y^\circ$  pulse is applied. This will turn the spin up again, but since the spin rotated during  $t_1$  the spin will not be parallel to the magnetic field, the component perpendicular to the magnetic field will still show precession, but the component parallel to the magnetic field will not. It is this latter component which maintains its magnetisation (apart from  $T_1$  relaxation). After a time  $t_{\text{mix}}$ , called the mixing time, again a  $90_y^\circ$  pulse is given turning the spin component parallel to the magnetic field down again. Subsequently a  $180_y^\circ$  pulse is given after a time  $t_{\text{echo}}$ . This will result in a kind of turning back the clock for the spins.

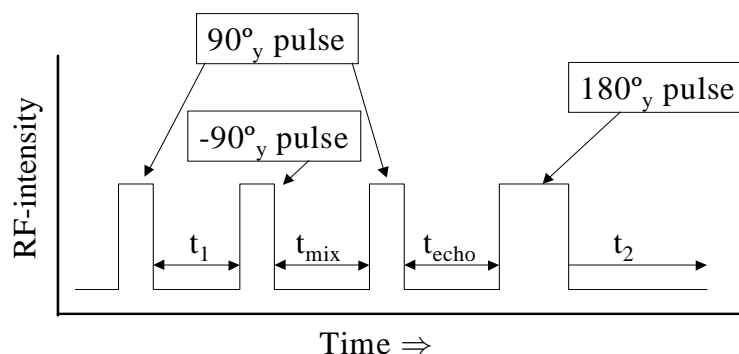


Figure 7.1: The sequence of pulses used in the two-dimensional MAS-NMR technique.

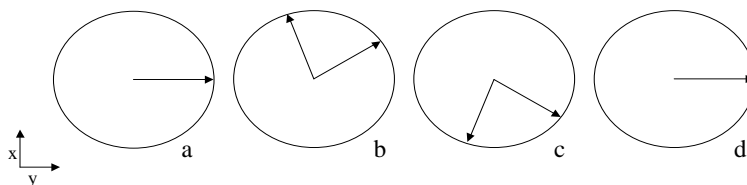


Figure 7.2: The principle of a spin-echo. (a) The spins are all perpendicular to the magnetic field. (b) The spins start to precess with different frequencies since they experience different magnetic fields, leading to a depolarization of the spins. (c) After a 180<sub>y</sub> pulse the spins keep precessing with the same frequency as they had before the 180<sub>y</sub> resulting in an echo of the spin polarization at  $t=0$  (d).

After  $t_{\text{echo}}$ , after the 180<sub>y</sub> pulse, the spins will be in exactly the same position as they were at the end of the second 90<sub>y</sub> pulse, which is called a spin echo. The principle of the echo is schematically shown in figure 7.2. The acquisition of signals start after the 180<sub>y</sub> pulse. The first dimension is called the  $t_1$  dimension in which for values of  $t_1$ , starting at  $t_1 = 0$  and increasing with constant step size the <sup>7</sup>Li MAS-NMR spectrum is measured. The second dimension is the  $t_2$  dimension in which the free induction decay (FID) is measured for  $t_2 \approx 0$  to  $t_2 \geq 2t_{\text{echo}}$ .

To understand the meaning of the  $t_1$  variation the following is noted. As we increase  $t_1$  the spin will rotate over a larger angle resulting in a different phase of the spin at the time the  $t_{\text{mix}}$  starts. The component of the spin parallel to the magnetic field is of a different size as a function of  $t_1$ , therefore the phase of the spin changes as a function of  $t_1$ . Performing a Fourier



transform in the  $t_2$  direction results in a delta function at the precession frequency, since the Fourier transform of  $\cos(\omega_0 t)$  is given by

$$\cos(\omega_0 t) \xrightarrow{\mathcal{F}} \pi[\delta(\omega - \omega_0) + \delta(\omega + \omega_0)] \quad (7.1)$$

The phase of the spin (and thus the measured spectrum) changes as a function of  $t_1$ , therefore, the amplitude of the delta-functions changes as a function of  $t_1$  as well, since the Fourier transform of  $\cos(\omega_0 t - t_0)$  is given by

$$\cos(\omega_0 t - \omega_0 t_1) \xrightarrow{\mathcal{F}} e^{-i\omega_0 t_1} \pi[\delta(\omega - \omega_0) + \delta(\omega + \omega_0)] \quad (7.2)$$

From equation (7.2) it is clear that the amplitude of the delta function oscillates with frequency  $\omega_0$  as a function of  $t_1$ . Thus a fourier transform in the  $t_1$  direction results also in a delta-function at frequency  $\omega_0$ .

The two-dimensional Fourier transformation results in a graph with on both axis a precession frequency, which can be regarded as the precession frequency before and after the mixing time respectively. When the atom does not jump to an other site during the mixing time the precession frequency before and after the mixing time will be exactly the same and thus only a signal on the diagonal of the graph is found, as is the case in the example described above.

In the case that the atom does not jump to another site during the mixing time a double Fourier transform results in a delta-function at the same frequency for both the Fourier transformed axis (only signal on the diagonal of the graph). We will now consider the case where the atom jumps to a different site during the mixing time.

When an atom jumps to a another site it will feel a different magnetic field resulting in a different precession frequency. If the atom jumps to another site during the mixing time this will first result in a different precession frequency of the spin after the second  $+90^\circ$  pulse. A two-dimensional Fourier transform will now result in a delta-function where the frequencies on both the axis are not the same, since the precession frequencies before and after the mixing time are not the same. This will result in a signal which is off diagonal, a so called crosspeak.

Until now we have discussed only a single spin. A whole spin system can be regarded as a summation of single spins. Therefore, we will not see only one peak on the diagonal in the case the spin is fixed to its site, but a complete spectrum, since the spins can be located at different sites. When spins jump to a different site this will result in off-diagonal signals (crosspeaks). The crosspeaks will be located at the intersection of a horizontal line through the position of the site where the atom was located before the mixing time and

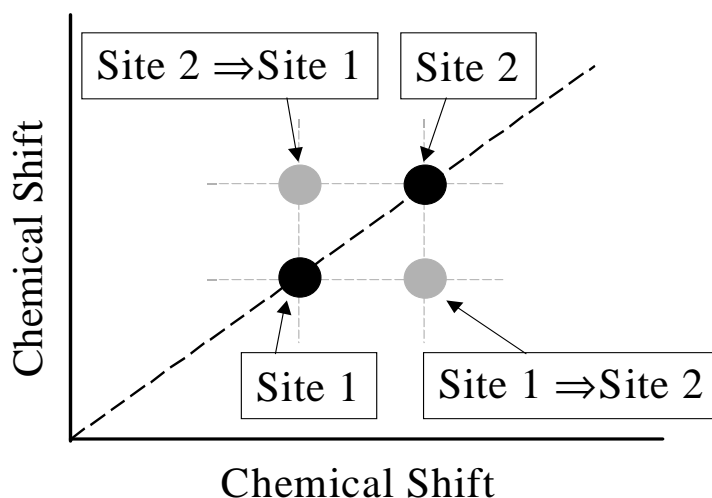


Figure 7.3: Example of a two-dimensional NMR spectrum. If the atoms are fixed to their site only a signal on the diagonal (indicated by the dashed line) will be observed in the figure indicated by the black dots. When the atoms jump to another site during the mixing time off-diagonal signals will appear, so called crosspeaks, in the figure indicated by the grey dots. One crosspeak is caused by atoms jumping from site 1 to site 2 and the other is caused by atoms jumping in the other direction.

a vertical line through the position of the site where it is located after the mixing time, as indicated in figure 7.3.

### Rotor synchronized MAS-NMR

As has been discussed in chapter 5 the magic-angle spinning technique is very useful for suppressing the dipole-dipole interactions and first order quadrupole interactions. Furthermore it can average chemical shift anisotropies. Spinning with a frequency smaller than the chemical shift anisotropy and the dipole-dipole interaction (expressed in Hz) will result in a repetition of the NMR-spectrum (so called spinning side bands), where the repetition distance between the spinning side bands is the spinning frequency and the envelope of their intensities reflects the shape of the static spectrum. Applying the MAS-NMR technique to the two-dimensional NMR will result in a repetition of the spectrum along the two axis, as indicated in figure 7.4a.

If we now synchronize the beginning and end of the mixing time with the rotation of the rotor, containing the sample, and use the whole echo technique described in paragraph 7.1.1 and in [49] the off-diagonal crosspeaks

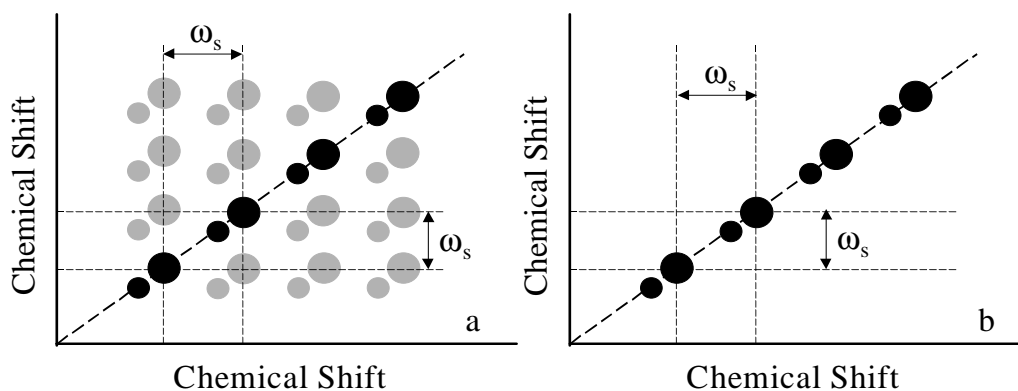


Figure 7.4: Example of a two-dimensional MAS-NMR spectrum without rotor synchronization (a) and with rotor synchronization, the crosspeaks between spinning side bands are indicated in grey (b). Distance between the spinning side bands is the spinning frequency  $\omega_s$ .

between spinning side bands can be suppressed (figure 7.4b). This leads to an improved signal to noise ratio for the spectrum on the diagonal, since it gains the intensity which was first in the spinning side bands. Furthermore the occurrence of crosspeaks between spinning side bands now indicates that an atom has moved to a position with another position in the chemical shift anisotropy profile, i.e. to a site that is crystallographically identical but that has another orientation with respect to the applied field  $B_0$ .

## 7.2 Experiments

The two-dimensional experiments were, just like the one-dimensional experiments discussed in chapter 5, recorded using a Bruker DMX-300 spectrometer operated at a frequency of 116 MHz. A 2.5 mm MAS probe with a rotor spinning at 28 kHz was employed. The temperature was controlled by putting the sample in a temperature controlled heated or cooled nitrogen gas flow and was stabilized within 0.5 K.

The  $90^\circ$  and  $180^\circ$  pulses were determined to be  $1.7 \mu\text{s}$  and  $3.3 \mu\text{s}$  respectively. The used band width for recording the spectra was 500 kHz. Determination of the relaxation time  $T_1$  resulted in a value of 10 ms. As a reference point the resonance of  $^7\text{Li}$  in an aqueous solution of LiCl has been used.

### 7.2.1 Data analysis

The data analysis for the two-dimensional NMR spectra is some what more complicated than the analysis for the one-dimensional spectra. First the data set will be Fourier transformed in the  $t_2$  direction. To suppress unwanted Fourier wiggles we apodized the data in the  $t_2$  direction using a Gaussian line shape with a line broadening of 1200 Hz. The data size was doubled by zero filling, resulting in a smoother spectrum after Fourier transforming. Subsequently the data set was Fourier transformed in the  $t_2$  direction, after which the data were phased. In the  $t_1$  direction the data were apodized using a  $\cos^2$  function. Like in the  $t_2$  direction the data size in the  $t_1$  direction was doubled by zero filling. Finally the data set was Fourier transformed in the  $t_1$  direction using a complex Fourier transform. In figure 7.5 several two-dimensional NMR spectra for various temperatures are shown.

### 7.2.2 Temperature calibration

The temperature of the sample is controlled by a nitrogen flow around the sample as was the case for the one-dimensional MAS-NMR measurements. As a result of friction when spinning the sample, caused by the high spinning frequencies the temperature of the sample will be considerably higher than the temperature of the nitrogen gas flow. Therefore, we performed a temperature calibration, using the resonance of  $^{207}\text{Pb}$  in  $\text{Pb}(\text{NO}_3)_2$  [25]. First the position of the  $^{207}\text{Pb}$  resonance at room temperature was determined without spinning the sample. Subsequently the  $^{207}\text{Pb}$  resonance was determined spinning the sample at a frequency of 28 kHz at room temperature, 345 K, 355 K, 380 K, and 400 K. The shift of the  $^{207}\text{Pb}$  resonance as function of temperature is shown in figure 7.6.

According to Bielecki et al. [25] the temperature dependence of the  $^{207}\text{Pb}$  resonance is given by

$$\Delta T = \frac{0.753}{\Delta} + 300 \quad (7.3)$$

where  $\Delta$  is the shift of the  $^{207}\text{Pb}$  resonance and  $\Delta T$  is the difference in temperature with respect to 300 K.

Since the shift of the  $^{207}\text{Pb}$  resonance with respect to the position of the  $^{207}\text{Pb}$  resonance at 300 K without spinning is known, we can now calculate the temperature of the  $\text{Pb}(\text{NO}_3)_2$  at the experimental temperatures and the used spinning frequency. The results of the temperature calibration are given in table 7.1. It may be noted that  $\text{Li}[\text{Mn}_{1.96}\text{Li}_{0.04}]\text{O}_4$  has another independent means of temperature calibration, its Curie-Weiss behaviour of the chemical

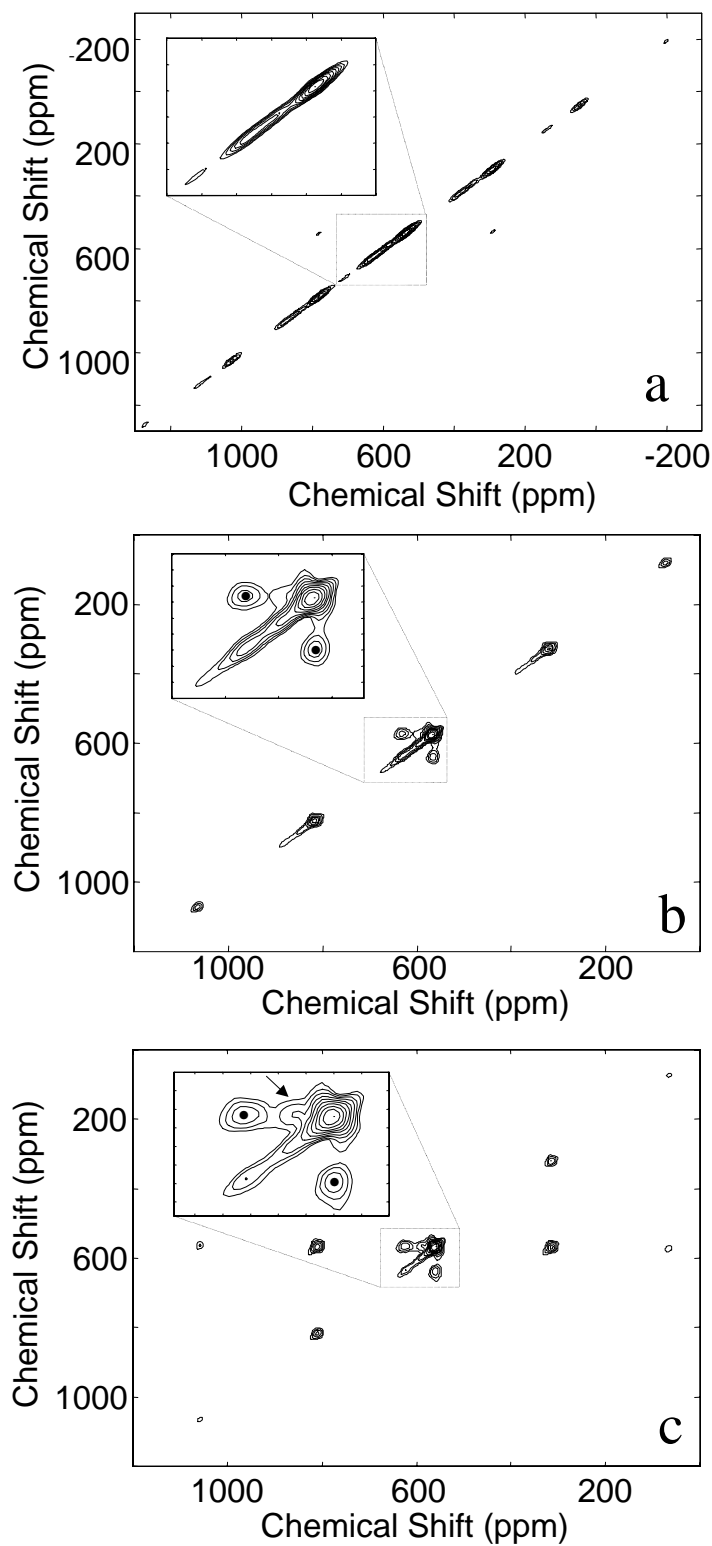


Figure 7.5: 2D MAS NMR spectra of  $\text{Li}[\text{Mn}_{1.96}\text{Li}_{0.04}]\text{O}_4$  a) at 285 K with  $t_{\text{mix}} = 5$  ms, b) at 380 K with  $t_{\text{mix}} = 5$  ms and c)  $t_{\text{mix}} = 10$  ms. The spinning speed equals 28 kHz (241 ppm). The arrow marks the 8a-16d crosspeak. Plots were produced by MATNMR.

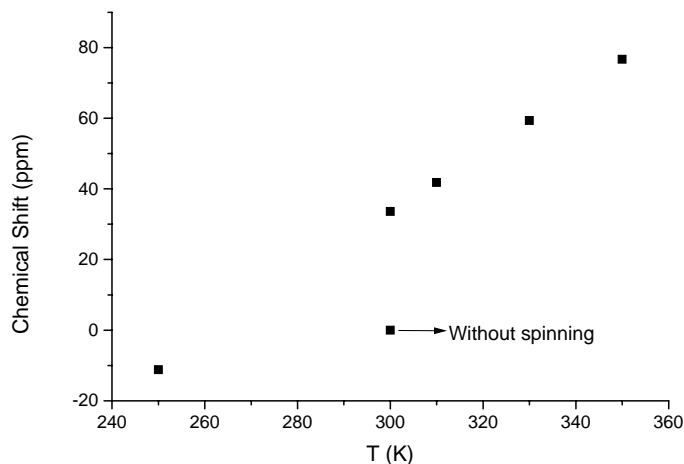


Figure 7.6: The position of the  $^{207}\text{Pb}$  resonance in  $\text{Pb}(\text{NO}_3)_2$  at a spinning frequency of 28 kHz as a function of the set-point temperature.

shift.

Table 7.1: The calibrated temperatures ( $T_{\text{cal}}$ ) for various nitrogen gas flow temperatures ( $T_N$ ) at a spinning frequency of 28 kHz.

$T_N$ [K]	250	300	310	330	350
$T_{\text{cal}}$ [K]	285	345	355	380	400

From now on we will use the calibrated temperatures instead of the set point temperatures of the temperature controller.

## 7.3 Results and Discussion

The results of the two dimensional rotor synchronized MAS-NMR experiments will be presented and discussed.

### 7.3.1 Crosspeaks

Figure 7.5a, in which the 2D spectrum of  $\text{Li}[\text{Mn}_{1.96}\text{Li}_{0.04}]\text{O}_4$  at a temperature of 285 K is plotted, shows the absence of exchange between different sites for a mixing time of  $t_{\text{mix}} = 5$  ms. It also demonstrates the good performance

of the rotor-synchronized-pulse sequence which causes strong signals to be found on the diagonal and crosspeaks between side bands of the same site to be suppressed. Furthermore, it indicates that spin diffusion is completely absent due to the fast MAS used in these experiments. As the temperature is increased, the 2D plot (figure 7.5b) shows the onset of crosspeaks for the same  $t_m$ . A gradual conversion of the diagonal peaks towards a more circular shape corresponds to Li ions remaining at the same site, but experiencing a slight change in the environment, which is caused by other nearby Li ions changing position. Note that intense crosspeaks are observed between Li signals from Li on the 8a and 16c sites. This means that large fractions of the Li hop from highly occupied 8a sites to the lower occupied interstitial 16c sites. The signal is assigned to the 16c site rather than to the 16d site, since the shortest diffusion path from 8a to 8a sites leads from 8a to 16c to 8a in an almost straight line. The results directly indicate that Li occupies the interstitial 16c site for a finite amount of time. Increasing the mixing time results in increased crosspeak intensities as can be seen in figure 7.7. Here the crosspeak intensity relative to the intensity of the largest peak as a function of the mixing time has been plotted. The intensity of the peaks has been determined by adding up all the data points which lie within a rectangle around the center of the peak. The dimensions of the rectangle match the width of the peak. Full saturation of the crosspeaks has not been achieved at this temperature as this would require a mixing time which is longer than the  $T_1$  relaxation time ( $T_1 = 10$  ms).

As can be seen in figure 7.5c new crosspeaks appear in the spectra at 380 K for a mixing time of  $t_{\text{mix}} = 10$  ms. The occurrence of these new peaks indicates that secondary hopping processes are becoming prominent, i.e. there is sufficient mobility to make more than one jump during  $t_m$ . This directly results in crosspeaks between 8a spinning side bands following  $8a \Rightarrow 16c \Rightarrow 8a$  hopping, since different 8a sites have a different orientation of the anisotropy tensor with respect to the applied field. The crosspeak indicated by an arrow in figure 7.5c shows that hopping between the 8a and the 16d site also becomes an important process.

After this quite qualitative treatment of the behaviour of the crosspeaks we will give a more quantitative treatment in the following section.

### 7.3.2 Jump model

In general the intensity of a NMR peak is proportional to the number of atoms located at the site to which the peak is assigned. For a crosspeak this means that its intensity is proportional to the number of atoms jumping between 2 sites. The relative intensity of the crosspeak will, therefore, be

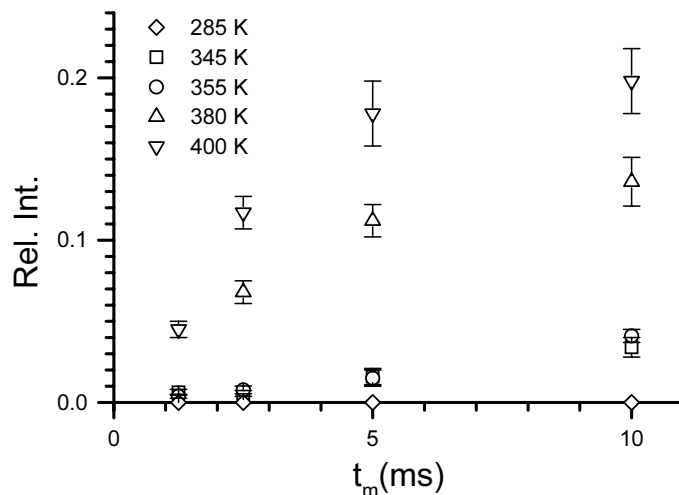


Figure 7.7: The relative 8a  $\rightarrow$  16c crosspeak intensity as a function of mixing time and temperature.



Figure 7.8: Representation of the jump model

equal to the chance that an atom jumps from one site to the other. This chance can be calculated using a so called jump model. The model will be described below.

As has been shown in the previous paragraph, there is mainly hopping between 2 sites. Therefore we consider only two sites. Only for the high temperatures and long mixing times jumping between more than 2 sites occurs. However, since our  $t_m$  could not be extended to sufficiently long times, it will not be possible to accurately determine the three-site model parameters. Therefore, we only consider the 8a site and the 16c site, with  $N_1$  and  $N_2$  atoms respectively. The chances for jumping from the 8a site to the 16c site and vice versa are denoted as  $\frac{1}{\tau_1}$  and  $\frac{1}{\tau_2}$  respectively (see figure 7.8), where  $\tau_1$  is the time spend on the 8a site and  $\tau_2$  is the time spend on the 16c site.



We will now define  $P_j(t)$  as the probability to be at site  $j = 1, 2$  at time  $t$ . This immediately implies that  $P_1(t) + P_2(t) = 1$  for all  $t$ . The time dependence of  $P_1(t)$  and  $P_2(t)$  can be written as

$$\frac{\partial}{\partial t} \begin{pmatrix} P_1(t) \\ P_2(t) \end{pmatrix} = \begin{pmatrix} -\frac{1}{\tau_1} & \frac{1}{\tau_2} \\ \frac{1}{\tau_1} & -\frac{1}{\tau_2} \end{pmatrix} \begin{pmatrix} P_1(t) \\ P_2(t) \end{pmatrix} \quad (7.4)$$

which can be written as

$$\frac{\partial}{\partial t} \begin{pmatrix} P_1(t) \\ P_2(t) \end{pmatrix} = -\widetilde{W} \begin{pmatrix} P_1(t) \\ P_2(t) \end{pmatrix} \quad (7.5)$$

where

$$\widetilde{W} = - \begin{pmatrix} -\frac{1}{\tau_1} & \frac{1}{\tau_2} \\ \frac{1}{\tau_1} & -\frac{1}{\tau_2} \end{pmatrix} \equiv \frac{1}{\tau} \begin{pmatrix} 1 + \epsilon & -1 + \epsilon \\ -1 - \epsilon & 1 - \epsilon \end{pmatrix} \quad (7.6)$$

with

$$\tau = \frac{2\tau_1\tau_2}{\tau_1 + \tau_2} \quad (7.7)$$

and

$$\epsilon = \frac{\tau_2 - \tau_1}{\tau_1 + \tau_2} \quad (7.8)$$

The eigenvalues  $\Psi^{(i)}$  and eigenvalues  $\lambda_j$ , defined by

$$\widetilde{W}\Psi^{(j)} = \lambda_j\Psi^{(j)} \quad j = 1, 2 \quad (7.9)$$

are given by

$$\begin{aligned} \lambda_1 &= 0 ; \quad \Psi^{(1)} = \frac{1}{\sqrt{2}} \begin{pmatrix} 1 - \epsilon \\ 1 + \epsilon \end{pmatrix} \\ \lambda_2 &= \frac{2}{\tau} ; \quad \Psi^{(2)} = \frac{1}{\sqrt{2}} \begin{pmatrix} 1 \\ -1 \end{pmatrix} \end{aligned} \quad (7.10)$$

We now represent  $\widetilde{W}$  diagonally

$$\widetilde{W} = \sum_{j=1,2} |\Psi^{(j)}\rangle \lambda_j \langle \Phi^{(j)}| \quad (7.11)$$

The "left-eigenvectors"  $\Phi^{(i)}$  satisfy

$$\langle \Phi^{(j)} | \Psi^{(l)} \rangle = \delta_{jl} \quad (j, l = 1, 2) \quad (7.12)$$

so that

$$\begin{aligned} \Phi^{(1)} &= \frac{1}{\sqrt{2}} \begin{pmatrix} 1 \\ -1 \end{pmatrix} \\ \Phi^{(2)} &= \frac{1}{\sqrt{2}} \begin{pmatrix} 1 + \epsilon \\ -1 + \epsilon \end{pmatrix} \end{aligned} \quad (7.13)$$

We are now able to solve the time evolution equation

$$\begin{pmatrix} P_1(t) \\ P_2(t) \end{pmatrix} = e^{-\tilde{W}t} \begin{pmatrix} P_1(0) \\ P_2(0) \end{pmatrix} \quad (7.14)$$

$$= \sum_{j=1,2} |\Psi^{(j)}\rangle e^{-\lambda_j t} \langle \Phi^{(j)} | \begin{pmatrix} P_1(0) \\ P_2(0) \end{pmatrix} \quad (7.15)$$

$$= \Psi^{(1)} \Phi^{(1)} \cdot \begin{pmatrix} P_1(0) \\ P_2(0) \end{pmatrix} e^{-\lambda_1 t} \\ + \Psi^{(2)} \Phi^{(2)} \cdot \begin{pmatrix} P_1(0) \\ P_2(0) \end{pmatrix} e^{-\lambda_2 t} \quad (7.16)$$

Using (7.10) and (7.13) equation (7.16) can be written as

$$\begin{pmatrix} P_1(t) \\ P_2(t) \end{pmatrix} = \frac{1}{2}(P_1(0) + P_2(0)) \begin{pmatrix} 1 - \epsilon \\ 1 + \epsilon \end{pmatrix} \\ + \frac{1}{2}[\epsilon(P_1(0) + P_2(0)) + P_1(0) - P_2(0)]e^{-\frac{2t}{\tau}} \begin{pmatrix} 1 \\ -1 \end{pmatrix} \quad (7.17)$$

Using that  $P_1(0) + P_2(0) = P_1(t) + P_2(t) = 1$  must apply for all  $t$ , results in

$$P_1(t) = \frac{1}{2}(1 - \epsilon) + \frac{1}{2}[\epsilon + P_1(0) - P_2(0)]e^{-\frac{2t}{\tau}} \quad (7.18)$$

$$P_2(t) = \frac{1}{2}(1 + \epsilon) - \frac{1}{2}[\epsilon + P_1(0) - P_2(0)]e^{-\frac{2t}{\tau}} \quad (7.19)$$

Since  $P_1(t) = 1 - P_2(t)$  we can now write the general solution as

$$P_2(t) = \frac{1}{2}(1 + \epsilon) - \left[ \frac{1}{2}(1 + \epsilon) - P_2(0) \right] e^{-\frac{2t}{\tau}} \quad (7.20)$$

Using (7.7) and (7.8) equation (7.20) can be written as

$$P_2(t) = \frac{\tau_2}{\tau_1 + \tau_2} - \left[ \frac{\tau_2}{\tau_1 + \tau_2} - P_2(0) \right] e^{-\frac{\tau_1 + \tau_2}{\tau_1 \tau_2} t} \quad (7.21)$$

With the initial condition  $P_1(0) = 1$  and  $P_2(0) = 0$  this becomes

$$P_2(t) = \frac{\tau_2}{\tau_1 + \tau_2} - \frac{\tau_2}{\tau_1 + \tau_2} e^{-\frac{\tau_1 + \tau_2}{\tau_1 \tau_2} t} \quad (7.22)$$

Equation (7.22) describes the chance that an atom, located at site 1 at  $t=0$ , is at site 2 after a time  $t$ . Since the crosspeak intensity is proportional to

this chance, equation (7.22) should also describe the behaviour of the relative crosspeak intensity as a function of time.

Without any extra information about  $\tau_1$  and  $\tau_2$ , we will be able to extract  $\tau_1$  and  $\tau_2$  from the fit of equation (7.22) to the mixing time dependent crosspeak intensities. However a higher accuracy can be reached by making use of the equilibrium condition.

In equilibrium ( $t \rightarrow \infty$ ) equation (7.22) becomes

$$P_2(\infty) = \frac{\tau_2}{\tau_1 + \tau_2} \quad (7.23)$$

and for  $P_1(t)$  this implies

$$P_1(\infty) = 1 - \frac{\tau_2}{\tau_1 + \tau_2} = \frac{\tau_1}{\tau_1 + \tau_2} \quad (7.24)$$

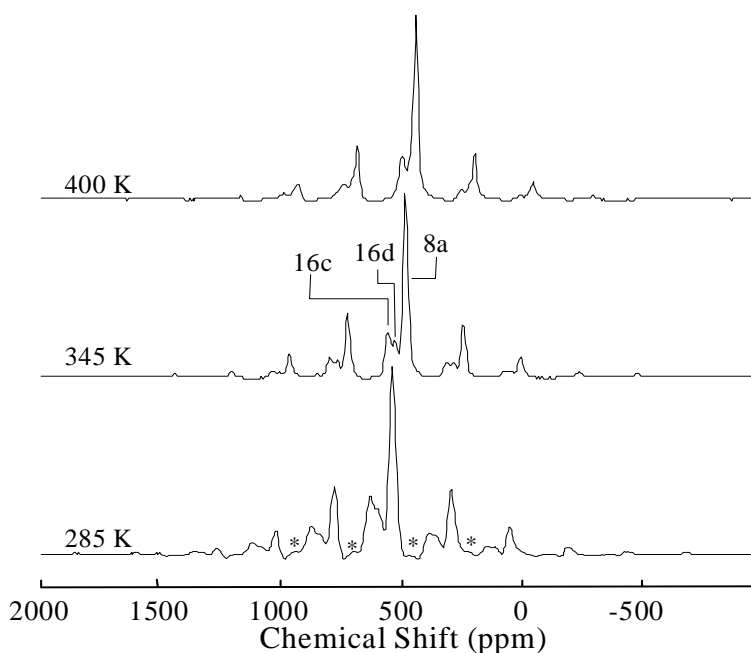


Figure 7.9:  ${}^7\text{Li}$ -MAS-NMR spectra of  $\text{Li}[\text{Mn}_{1.96}\text{Li}_{0.04}]\text{O}_4$  as a function of temperature (K). The spinning speed was  $28000 \pm 3\text{Hz}$  (241 ppm) and a  $90^\circ$  pulse length of  $1.7 \mu\text{s}$  was used. New peaks at 285 K are denoted by an asterisk.

These values of  $P_1(\infty)$  and  $P_2(\infty)$  are the relative intensities of the cross-peaks in equilibrium, which is the same as the relative intensities of the

peaks belonging to the considered sites in an one-dimensional NMR spectrum. Therefore, we also recorded the one dimensional MAS-NMR spectra of the sample at the same temperatures as where the two-dimensional experiments were performed. In figure 7.9 the  ${}^7\text{Li}$  MAS NMR spectra of  $\text{Li}[\text{Mn}_{1.96}\text{Li}_{0.04}]\text{O}_4$  are shown as a function of temperature. The strongest MAS NMR spinning side band manifold in the spectrum is, as described in chapter 5, assigned to lithium on 8a sites, which is the lithium site with the highest occupancy as was observed in neutron diffraction [26]. Since the peak widths are smaller than the ones reported in chapter 5, we can now clearly distinguish two smaller peaks belonging to lithium located at the 16d sites and the interstitial 16c sites [26]. Again all subspectra shift to smaller ppm values i.e. smaller hyperfine fields as the temperature increases, analyzed in refs. [30] and [31] as the effect of the paramagnetic susceptibility changing proportional to  $\frac{1}{T}$ . The large width of the spectrum is caused by the anisotropic polarization of the paramagnetic manganese magnetic moments [52]. The width expressed in ppm was checked to be field independent, which indicates negligible quadrupole interaction. Therefore, the spectrum has the shape of a central transition (no satellite transitions).

At high temperatures, i.e. 475 K, the lines start to coalesce due to motional averaging, indicating the onset of Li exchange between the different sites at a rate comparable to the distance in Hz between the different resonances. This is in agreement with the result reported by Lee et al. [31] indicating the same rapid exchange effect. At low temperatures, i.e. 285 K, line broadening (+ 35%) of all resonances becomes clearly visible in the 1D spectrum and additionally a fourth peak appears (fig. 7.9). This line broadening and the new peak may be caused by charge ordering of  $\text{Mn}^{3+}$  and  $\text{Mn}^{4+}$  as has been reported by Rodríguez-Carvajal [19]. Such a charge ordering leads to Li surroundings with different  $\text{Mn}^{3+}$  and  $\text{Mn}^{4+}$  coordinations instead of Mn-ions with all the same time-averaged +3.55 valence. As shown in figure 7.7 there is no lithium hopping at 285 K. Since the effects possibly caused by the charge ordering occurs at the same temperature as the onset of the lithium hopping, the two might be correlated.

In table 7.2 the ratios  $\frac{\tau_1}{\tau_1+\tau_2}$  and  $\frac{\tau_2}{\tau_1+\tau_2}$  derived from the peak intensities of the one-dimensional spectra are given. Knowing the ratio between  $\tau_1$  and  $\tau_2$ , the crosspeak intensities can be fitted and values for  $\tau_1$  and  $\tau_2$  can be derived. In figure 7.10 the fits of mixing time and temperature dependent crosspeak intensities are given. The values for  $\tau_1$  and  $\tau_2$  obtained from these fits are given in table 7.2.

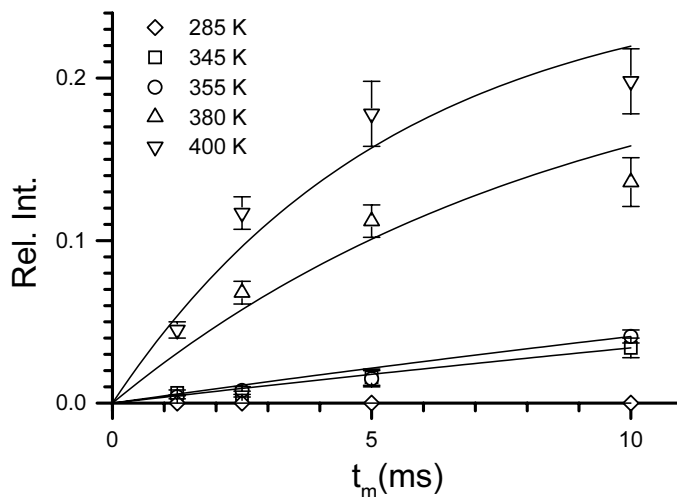


Figure 7.10: The intensity of 8a-16c crosspeaks as a function of mixing time ( $t_m$ ) for the temperatures (K) indicated in the figure.

### 7.3.3 Activation energy

Since in equilibrium the 8a sites and 16c sites are not equally occupied there will be a difference in energy level and also in activation energy for jumping from 8a to 16c and vice versa. In figure 7.11 a schematical plot of the activation energy and energy difference between the 8a and 16c sites is given.

The energy difference between the 8a and 16c sites can be determined by using the Boltzmann distribution, given by

$$N_x = N_0 e^{-\frac{E_x}{k_B T}} \quad (7.25)$$

where  $N_x$  is the number of atoms at site  $x$ ,  $N_0$  is a total number of atoms,  $E_x$  is the energy of site  $x$  and  $k_B$  is the Boltzmann constant.

If we now divide the peak intensities belonging to the 8a and 16c sites we obtain

$$\frac{I_{16c}}{I_{8a}} \sim \frac{N_{16c}}{N_{8a}} = e^{-\frac{(E_{16c}-E_{8a})}{k_B T}} = e^{-\frac{E_d}{k_B T}} \quad (7.26)$$

where  $E_d$  is the energy difference between the 8a and 16c sites. Doing so results in  $E_d = 700 \pm 70$  K.

In figure 7.12 the derived jump rates  $\frac{1}{\tau_i}$  have been plotted as a function of  $\frac{1}{T}$  on a semi-log scale. The data points in this Arrhenius plot have been fitted

Table 7.2: The ratio  $\frac{\tau_1}{\tau_2}$ , determined using the 1D NMR spectral intensities and jump rates derived by fitting curves of figure 7.10.

T (K)	$\frac{\tau_1}{\tau_2}$	$\frac{1}{\tau_1}$ (s <sup>-1</sup> )	$\frac{1}{\tau_2}$ (s <sup>-1</sup> )
285	—	—	—
345	3.7 ± 0.1	1.9 ± 0.4	6.8 ± 1.3
355	3.5 ± 0.1	2.3 ± 0.4	7.9 ± 1.6
380	3.3 ± 0.1	13 ± 1	43 ± 4
400	2.8 ± 0.1	24 ± 2	68 ± 6

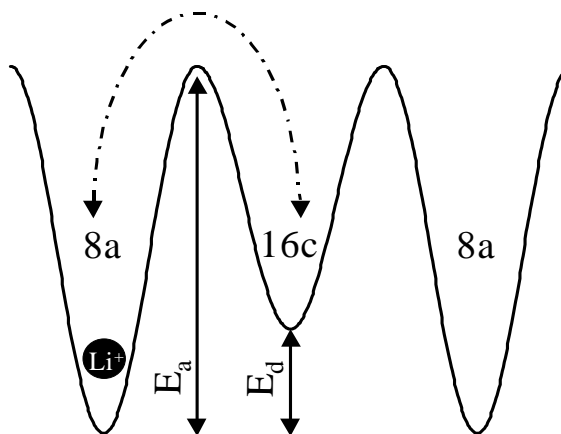


Figure 7.11: Schematic plot of the activation energy ( $E_a$ ) and energy difference ( $E_d$ ) between the 8a and 16c site.

to two exponential functions, where the difference between the exponents is the previously derived value for  $E_d$ , i.e. 700 K, and the result is also displayed in figure 7.12. The exponents give the activation energies for jumping from 8a to 16c and vice versa. The values derived here are  $E_{a(8a \rightarrow 16c)} = 6800\text{K}$  and  $E_{a(16c \rightarrow 8a)} = 6100\text{K}$ , which corresponds in both cases, within the error bars, to an activation energy of  $0.5 \pm 0.1\text{eV}$ . Using conductivity measurements Massarotti et al. [53] found a value of 0.4 eV for the activation energy of the Li-ion conduction process, which is in good agreement with the value found in this study using a microscopic method. It can, therefore, be concluded that this microscopically determined activation energy is the main barrier for the macroscopic Li-ion transport, i.e. that the hopping along the  $8a \Rightarrow 16c$  diffusion path observed here corresponds to the main lithium-ion conduction process.

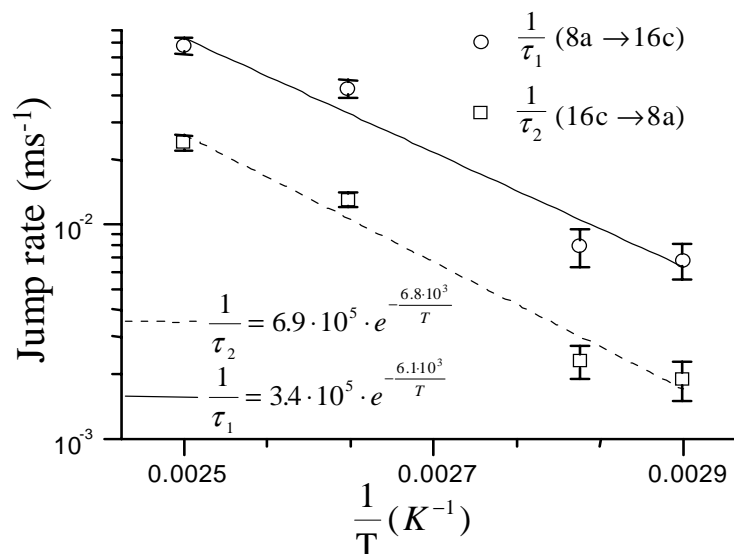


Figure 7.12: Semi-log plot of the derived jump rates versus  $\frac{1}{T}$ . Using  $\frac{1}{\tau}(T) = \frac{1}{\tau}(\infty) \exp(-\frac{E}{k_B T})$  the activation energies  $E$  are calculated to be  $E=0.5 \pm 0.1$  eV.

### 7.3.4 Self diffusion coefficient

Assuming a random walk, we can derive a self-diffusion coefficient from the obtained jump rate. The self-diffusion coefficient  $D_s$  is given by

$$D_s = \frac{1}{4} \frac{l^2}{\tau} \quad (7.27)$$

where  $l$  is the distance over which the Li-ions jump and  $\frac{1}{\tau}$  is the jump rate. From crystallographic data the distance between a 8a and a 16c site is obtained to be 1.78 Å. Therefore, we take for  $l$  this value. Since we have two different jump rates, one for jumping from 8a to 16c and one for the other way around, an average jump rate  $\frac{1}{\tau}$  is defined, i.e.,

$$\frac{1}{\tau} = \frac{\tau_1 + \tau_2}{2\tau_1\tau_2} \quad (7.28)$$

The self-diffusion coefficients derived in this way are given in table 7.3. The obtained values for the self-diffusion coefficients are rather small compared to the expected macroscopic ones. Therefore, it is important to note that these self-diffusion coefficients are derived by studying the movement of a single ion in an equilibrium distribution of lithium-ions in the crystals. As

is explained by e.g. Crank [54], differences between self-diffusion coefficients and macroscopic (chemical) diffusion coefficients, can create large (local) gradients in the lithium concentration, which are not present when measuring self-diffusion coefficients. Resulting in possibly large differences between self-diffusion coefficients and macroscopic diffusion coefficients.

Table 7.3: The self-diffusion coefficients obtained from the derived jump rates.

T (K)	$D_s$ ( $10^{-16}\text{cm}^2\text{s}^{-1}$ )
285	—
345	$3.4 \pm 0.7$
355	$4.0 \pm 0.8$
380	$22 \pm 2$
400	$36 \pm 4$

## 7.4 Comparison with electron diffraction and QENS

Now we fully analyzed the 2D data in terms of the lithium hopping mechanism and its activation energy, we have the parameters available to discuss the following. In principle the 2D-NMR technique measures exchanges between different sites. But what if lithium would not move, but the electron on a  $\text{Mn}^{3+}$  site would hop to a  $\text{Mn}^{4+}$  site. Could this result in the same type of 1D, 2D NMR data and activation energies? Several results show that the answer is no. First of all the charge ordering / localisation reported by [19] and in the thesis (chapter 6) takes place below room temperature and is observable using very fast time scale techniques (electron diffraction and neutron scattering). Localized  $\text{Mn}^{3+}$  and  $\text{Mn}^{4+}$  cannot be observed anymore above room temperature indicating that electron hopping frequencies are well above  $10^{12}$  Hz, i.e. completely out of the time scale range of NMR. Furthermore, the activation energy for electron hopping may be of the order of the charge ordering temperature, i.e. room temperature  $\approx 28$  meV. This is much smaller than the activation energy found in the 2D NMR experiments, which equals  $0.5 \pm 0.1$  eV. At low temperatures the electron hopping rate will slow down and eventually the NMR experiments can pick up the charge localization. This was observed in figure 7.9 via additional peaks and heterogeneous line broadening. This indicates that one observes a distribution



of Li sites, which is in agreement with the more or less random distribution of  $\text{Mn}^{3+}$  and  $\text{Mn}^{4+}$  over the Mn sites, giving many different local surroundings for a Li-ion. Above the charge localization temperature only one time averaged type of Mn is present:  $\text{Mn}^{3.5+}$ , reducing the number of different Li surroundings to the number of crystallographic sites. The occupations of the 3 sites are also in agreement with what one expects from neutron diffraction and chemical analysis.

Y.J. Lee et al. [31] attributed the different Li surroundings in the NMR spectra to different localized  $\text{Mn}^{3+}$  and  $\text{Mn}^{4+}$  surroundings even at temperatures above the charge localization temperature. This could be done since the 2D data were not available then, showing directly the motion of lithium between sites.

## 7.5 Conclusions

To our knowledge, this is the first time that the microscopic mobility of Li-ions has been observed directly in  $\text{Li}[\text{Mn}_{1.96}\text{Li}_{0.04}]\text{O}_4$  using a powerful 2D NMR technique. Temperature dependent experiments indicate an onset of lithium exchange on a ms time scale between two sites at 285 K and between more than two sites at 380 K. Line broadening and a fourth spinning-sideband manifold, which are probably caused by charge ordering of  $\text{Mn}^{3+}$  and  $\text{Mn}^{4+}$ , disappears at the same temperature as the lithium exchange starts, indicating that the charge ordering and lithium-ion dynamics are correlated. Enhanced screening of the ions in the crystal may lower the barriers for Li mobility, which is subject of further research. The equilibrium occupation of the 8a and 16c sites and the exponential time dependence of the crosspeaks yields the  $8a \Rightarrow 16c$  and  $16c \Rightarrow 8a$  activation energies. These activation energies of  $0.5 \pm 0.1$  eV are in good agreement with values found in literature [53] from macroscopic methods. This indicates that the diffusion path found here represents the primary Li-ion conduction mechanism.



# Chapter 8

## General Conclusions

In this thesis two materials have been studied which are being used in all solid-state Li-ion batteries. The fundamentals of these materials were investigated using different experimental techniques, providing a wealth of new information.

The neutron diffraction experiments on pure and Li-doped  $\text{BPO}_4$  revealed that the interstitial Li-ions and the charge compensating boron vacancies are randomly distributed over the available lattice sites, since there are no major differences between the spectra of pure and Li-doped  $\text{BPO}_4$ .

Temperature dependent neutron scattering experiments on  $\text{Li}[\text{Mn}_{1.96}\text{Li}_{0.04}]\text{O}_4$  showed that by substituting 2 percent of the manganese ions by lithium ions results in a total disappearance of the Jahn-Teller distortion. These experiments revealed furthermore that the manganese spins in  $\text{Li}[\text{Mn}_{1.96}\text{Li}_{0.04}]\text{O}_4$  order only over a short range, whereas the manganese spins in  $\text{Li}_{0.2}[\text{Mn}_{1.96}\text{Li}_{0.04}]\text{O}_4$  order over a long range resulting in a three-dimensional magnetic lattice.

The one-dimensional NMR experiments are in good agreement with the crystallographic data from literature. The 8a and 16c sites are clearly visible, but unfortunately the peaks assigned to the 16d and 8a sites are overlapping making the 16d sites invisible. Extracting 25% of the lithium results in a shift of the spectrum to larger hyperfine fields which can be explained by the increased amount of  $\text{Mn}^{4+}$ , i.e. larger Mn magnetic moments. Contrary to the spectrum of  $\text{Li}[\text{Mn}_{2-y}\text{Li}_y]\text{O}_4$  only one resonance is observed, probably caused by an increased lithium mobility and increased line width related to this mobility. Extracting even more lithium results in a spectrum with 2 subspectra and which is twice as broad as the previous ones, caused by the increased amount of  $\text{Mn}^{4+}$ .

The Quasi Elastic Neutron Scattering experiments showed that the  $\text{Mn}^{3+}$  ions in the material  $\text{Li}[\text{Mn}_{1.96}\text{Li}_{0.04}]\text{O}_4$  are in the low spin state, suppressing

the Jahn-Teller effect. At temperatures below room temperature, short range anti-ferromagnetic correlations between the magnetic moments of manganese ions develop consistent with charge localization on the  $\text{Mn}^{3+}$  and  $\text{Mn}^{4+}$  sites. Cooling down below  $T_f = 25$  K gives a special type of spin-glass in which the spins are partially frozen spin-glass-like and partially free like in a spin-liquid. The spins of the  $\text{Mn}^{4+}$  ions are thought to be frozen, while the spins of the  $\text{Mn}^{3+}$  ions are free to rotate. The trend in  $d\sigma/d\Omega$  can adequately be described with a simple model. In this model non-linear chains of Mn ions with anti-ferromagnetic ordering within the chain are supposed to be present.

To our knowledge the two-dimensional NMR experiments showed for the first time directly a microscopic mobility of Li-ions in  $\text{Li}[\text{Mn}_{1.96}\text{Li}_{0.04}]\text{O}_4$ . Temperature-dependent experiments indicate an onset of lithium exchange on a ms time scale between two sites at 285 K and between more than two sites at 380 K. Line broadening and a fourth spinning-side-band manifold, which are probably caused by charge ordering of  $\text{Mn}^{3+}$  and  $\text{Mn}^{4+}$ , disappears at the same temperature as the lithium exchange starts, indicating that the charge ordering and lithium-ion dynamics are correlated. Enhanced screening of the ions in the crystal may lower the barriers for Li mobility, which is subject of further research. The equilibrium occupation of the 8a and 16c sites and the exponential time dependence of the crosspeaks yields the  $8a \Rightarrow 16c$  and  $16c \Rightarrow 8a$  activation energies. These activation energies of  $0.5 \pm 0.1$  eV are in good agreement with literature values from macroscopic methods. This indicates that the diffusion path found here represents the primary Li conduction mechanism.

# Bibliography

- [1] Linden, D. *Handbook of Batteries, 2<sup>nd</sup> edition*. McGraw-Hill, Inc., (1995).
- [2] The International Energy Agency. *Assesment of Electric Vehicle Impacts on Energy, Environment and Transportation Systems*. (1999).
- [3] The International Energy Agency. *Implementation Agreement for Electric Vehicle Technologies and Programmes*. (annual report 1995).
- [4] Shu, Z. X., McMillan, R. S., and Murray, J. J. *J. Electrochem. Soc.* **140**, L101 (1993).
- [5] Jiang, Z., Alamgir, M., and Abraham, K. M. *J. Electrochem. Soc.* **142**, 333 (1995).
- [6] Alamgir, M. and Abraham, K. M. *in Lithium Batteries (Industrial Chemistry Library, volume 5)*, G. Pistoia, Editor, Elsevier Science, Amsterdam , 94 (1994).
- [7] Jak, M. J. G. *Dynamic compaction of Li-ion battery components and batteries*. PhD thesis, TU-Delft, (1999).
- [8] Freund, A. *Nucl. Instr. Meth.* **213**, 495 (1983).
- [9] Schiff, L. I. *Quantum Mechanics, Third Ed.* McGraw-Hill, (1968).
- [10] Lovesey, S. W. *Theory of Neutron Scattering from Condensed Matter, Vol. 2*. Clarendon Press, (1984).
- [11] Schulze, G. E. R. *Z. Physik. Chemie B* **25**, 215 (1934). in German.
- [12] *JCPDS data file 34-132*. (1992).
- [13] Kelder, E. M., Jak, M. J. G., de Lange, F., and Schoonman, J. *Solid State Ionics* **85**, 285–291 (1996).

- 
- [14] Jak, M. J. G., Kelder, E. M., and Schoonman, J. *J. Solid State Chem.* **141** (1998).
- [15] Jak, M. J. G., Kelder, E. M., van der Pers, N. M., Weisenburger, A., and Schoonman, J. *J. Electroceramics* **2**, 127 (1998).
- [16] Sears, V. F. *Adv. Phys.* **24**, 1 (1975).
- [17] Larson, A. C. and Dreele, R. B. V. Technical Report NM 87545, Los Alamos National Laboratory, (1994).
- [18] Orgel, L. E. *An Introduction to Transition Metal Chemistry*. Methuen/Wiley, (1996). second edition.
- [19] Rodríguez-Carvajal, J., Rouse, G., Masquelier, C., and Hervieu, M. *Phys. Rev. Let.* **81**, 4660 (1998).
- [20] Hunter, J. C. *J. Solid State Chem.* **39**, 142 (1981).
- [21] Hahn, T., editor. *International Tables for Crystallography*, volume B. Kluwer Academic Publishers, (1996). Fourth revised edition.
- [22] Kaiser, C. T., Verhoeven, V. W. J., Gubbens, P. C. M., Mulder, F. M., de Schepper, I. M., Yaouanc, A., de Réotier, P. D., Cottrell, S. P., Kelder, E. M., and Schoonman, J. *Phys. Rev. B* **62**, 9236 (2000).
- [23] Abragam, A. *Principles of Nuclear Magnetism*. Oxford Science Publications, Oxford, (1961).
- [24] Lide, D. R., editor. *Handbook of Chemistry and Physics*. CRC press, London, 79 edition, (1998).
- [25] Bielecki, A. *J. Magn. Reson.* **116**, 215 (1995).
- [26] Berg, H., Kelder, E. M., and Thomas, J. O. *J. Mater. Chem.* **9**, 427 (1999).
- [27] Verhoeven, V. W. J., de Schepper, I. M., Nachtegaal, G., Kentgens, A. P. M., Kelder, E. M., Schoonman, J., and Mulder, F. M. *Phys. Rev. Let.* **86-19**, 4314 (2001).
- [28] Chiang, Y. M., Birnie, D. P., and Kingery, W. D. *Physical ceramics*. Wiley, (1997).
- [29] Schimmel, H. G., Montfrooij, W., Kearley, G. J., Verhoeven, V. W. J., and de Schepper, I. M. *Phys. Rev. B* **63**, 214409 (2001).

- 
- [30] Gee, B., Horne, C. R., Cairns, E. J., and Reimer, A. J. *J. Phys. Chem. B* **102**, 10142 (1998).
- [31] Lee, Y. J., Wang, F., and Crey, C. P. *J. Am. Chem. Soc.* **120**, 12601 (1998).
- [32] Lovesey, S. W. *Theory of neutron scattering from condensed matter; nuclear scattering*, volume 1. Oxford University Press, New York, (1984).
- [33] Squires, G. L. *Introduction to the theory of thermal neutron scattering*. Cambridge University Press, Cambridge/London/New York/Melbourne, (1978).
- [34] Reimers, J. N. *Phys. Rev. B* **46**, 193 (1992).
- [35] Bertaut, E. F. and Burlet, P. *Solid State Commun.* **5**, 279 (1967).
- [36] Eisberg, R. M. and Resnick, R. *Quantum physics of atoms, molecules, solids, nuclei, and particles*. John Wiley & Sons, (1985). second edition.
- [37] Jang, Y., Huang, B., Chou, F., Sadoway, D. R., and Chiang, Y. *J. Appl. Phys.* **87**, 7382 (2000).
- [38] Anderson, P. W. *Phys. Rev.* **102**, 1008 (1956).
- [39] Chen, Y., Honda, Z., Zheludev, A., Broholm, C., Katsumata, K., and Shapiro, S. M. *Phys. Rev. Lett.* **86**, 4721 (2001).
- [40] Verhoeven, V. W. J., Mulder, F. M., and de Schepper, I. M. *Physica B* **276-278**, 950 (2000).
- [41] Endres, P., Fuchs, B., Kemmler-Sack, S., Brandt, K., Faust-Becker, G., and Praas, H. W. *Solid State Ionics* **89**, 221 (1996).
- [42] Wills, A. S., Raju, N. P., and Greedan, J. E. *Chem. Mater.* **11**, 1510 (1999).
- [43] Crevecoeur, R. *Analogies in the microscopic behaviour of superfluid and classical helium studied by neutron scattering*. PhD thesis, Interfaculty Reactor Institute, TU-Delft, (1996).
- [44] Oohara, Y., Sugiyama, J., and Kontani, M. *J. Phys. Soc. Jpn.* **68**, 242 (1999).
- [45] Brown, P. J., editor. *International Tables for Crystallography*, volume c. Kluwer Academic Publishers, (1996). Fourth revised edition.

- [46] Ashcroft, N. W. and Mermin, N. D. *Solid State Physics*. Holt-Saunders Japan, Tokyo, International edition, (1981).
- [47] de Schepper, I. M. lecture notes: "stralingsfysica", (2000).
- [48] Jong, A. F., Kentgens, A. P. M., and Veeman, W. S. *Chem. Phys. Lett.* **109**, 337 (1984).
- [49] Ernst, M., Kentgens, A. P. M., and Meier, B. H. *J. Magn. Reson.* **138**, 66 (1999).
- [50] Kentgens, A. P. M., de Boer, E., and Veeman, W. S. *J. Chem. Phys.* **87**, 6859 (1987).
- [51] Schmidt-Rohr, K. and Spiess, H. W. *Multidimensional Solid State NMR and Polymers*. Academic Press, (1994).
- [52] Mustarelli, P., Massarotti, V., Bini, M., and Capsoni, D. *Phys. Rev. B* **55**, 12018 (1997).
- [53] Massarotti, V., Capsoni, D., Bini, M., Ghiodelli, G., Azzoni, C. B., Mozzati, M. C., and Paleari, A. *J. Solid State Chem.* **131**, 94 (1997).
- [54] Crank, J. *The Mathematics of Diffusion*. Oxford Science Publications, (1975). second edition.



# A fundamental study on materials for Li-ion batteries

by Vincent W.J. Verhoeven

## Summary

In this thesis an experimental study of the fundamental properties of pure and Li-doped  $\text{BPO}_4$  is described.  $\text{BPO}_4 + z\% \text{Li}_2\text{O}$  can be used as a solid electrolyte in solid-state Li-ion batteries. In addition  $\text{LiMn}_2\text{O}_4$ -based cathode materials have been studied.

The structure of pure  $\text{BPO}_4$  and Li-doped  $\text{BPO}_4$  has been studied by neutron scattering. Rietveld refinement of the neutron spectra of the doped material did not show additional phases or a lithium superstructure. It appears that the interstitial  $\text{Li}^+$ -ions as well as the charge compensating boron vacancies and substitutionally incorporated  $\text{Li}^+$ -ions on boron sites are randomly distributed over the lattice resulting in only a slight change in peak intensities.

The structure of  $\text{Li}_x[\text{Mn}_{1.96}\text{Li}_{0.04}]\text{O}_4$  with  $x=1$  and  $0.2$  has been studied as a function of temperature using neutron diffraction. For  $x=1$  and  $x=0.2$  the structure does not change between 4K and room temperature, showing that the reported Jahn-Teller distortion to be not present in presented materials. In the case for  $x=1$  a very broad peak is observed at small angles and at low temperatures, indicating a disordered magnetic structure. This is not the case for  $x=0.2$  where at 4K magnetic Bragg-peaks are observed, indicating a three dimensional ordering of manganese spins.

Studying  $\text{Li}_x\text{Mn}_2\text{O}_4$  with  $x=1, 0.75$  and  $0.2$  at various temperatures, using magic-angle-spinning nuclear magnetic resonance (MAS-NMR), show for

x=1 three Li resonances which have been assigned to different crystallographic sites for all temperatures. Decreasing the amount of lithium results in a broadening and disappearance of peaks, as well as an increase of the anisotropy.

Using quasi-elastic neutron scattering on  $\text{Li}_x[\text{Mn}_{1.96}\text{Li}_{0.04}]\text{O}_4$  at temperatures between 4 K and room temperature, it is found that this compound is a charge-disordered material in which both  $\text{Mn}^{3+}$ - $\text{Mn}^{3+}$  and  $\text{Mn}^{4+}$ - $\text{Mn}^{4+}$  non-linear chains are formed once the electrons have become localized. There is no correlation between the  $\text{Mn}^{3+}$  and  $\text{Mn}^{4+}$  chains. Unlike the case for the parent material  $\text{Li}_x\text{Mn}_2\text{O}_4$ , it is found that the Jahn-Teller active  $\text{Mn}^{3+}$ -ions are in the low-spin state. We observe critical slowing down of the  $\text{Mn}^{4+}$ - $\text{Mn}^{4+}$  spin fluctuations at  $T \sim 25$  K at which point the fluctuations freeze out, while  $\text{Mn}^{3+}$ - $\text{Mn}^{3+}$  spin-fluctuations persist at least down to 4 K.

To study the dynamics of lithium ions directly on a millisecond time scale we performed two-dimensional rotor-synchronized magic-angle-spinning nuclear-magnetic-resonance experiments. A millisecond time scale exchange of lithium between two crystallographic sites, the 8a and 16c sites, starts around 285 K. At 380 K lithium even starts to hop between more than two sites. The Li diffusion pathway involving the 8a and 16c sites, the equilibrium Li site occupancies in relation to activation energies, and the Li jump rates are derived directly from the NMR mixing time and temperature-dependent measurements. The microscopic activation energies are in agreement with those determined macroscopically.

# Fundamenteel onderzoek aan materialen voor Li-ion batterijen

door Vincent W.J. Verhoeven

## Samenvatting

Dit proefschrift beschrijft een experimentele studie naar de fundamentele eigenschappen van materialen die gebruikt kunnen worden in een "all solid-state" Li-ion batterij. Hierbij is gekeken naar twee materialen, het electrolyte materiaal  $\text{BPO}_4 + z\% \text{Li}_2\text{O}$  and het cathode materiaal  $\text{LiMn}_2\text{O}_4$ .

De structuur van puur  $\text{BPO}_4$  en Li-doped  $\text{BPO}_4$  is onderzocht met behulp van neutronen diffractie. Rietveld refinement aan de neutronen spectra van het Li-doped materiaal laat zien dat het materiaal enkel fasig is en er geen lithium superstructuren aanwezig zijn. Het blijkt dat het interstitiele lithium zowel als de lading compenserende boron gaten en het substitutionele lithium random verdeelt zijn over het rooster, wat resulteert in kleine veranderingen in intensiteit verschillen in de neutronen spectra.

De structuur van  $\text{Li}_x[\text{Mn}_{1.96}\text{Li}_{0.04}]\text{O}_4$  met  $x=1$  en  $0.2$  is bestudeerd met neutronen diffractie als een functie van de temperatuur. Voor beide waarden van  $x$  veranderd de structuur niet tussen kamertemperatuur en 4K. Dit betekent dat de in de literatuur vermelde Jahn-Teller overgang niet optreedt in deze materialen. Bij het sample met  $x=1$  zien we bij lage temperaturen een brede hobbels, die duidt op een wanordelijke magnetische structuur. Voor het sample met  $x=2$  zien we echter bij 4K magnetische Bragg pieken die duiden

op een drie dimensionale ordening van mangaan spins.

Bestuderen we  $\text{Li}_x[\text{Mn}_{1.96}\text{Li}_{0.04}]\text{O}_4$  ( $x=1, 0.75$  en  $0.2$ ) temperatuur afhankelijk met magic-angle-spinning nuclear magnetic resonance (MAS-NMR), dan zien we voor  $x=1$  drie lithium resonansies die zijn toegeschreven aan de verschillende kristallografische plaatsen van het lithium. Vermindering van de hoeveelheid lithium resulteert in een verbreding en verdwijning van de pieken. Tevens neemt de anisotropie toe.

Temperatuur afhankelijke quasi-elastische neutronen verstrooiing (QENS) aan  $\text{Li}[\text{Mn}_{1.96}\text{Li}_{0.04}]\text{O}_4$  heeft laten zien dat de ladingen van het mangaan wanordelijk verdeeld zijn en dat  $\text{Mn}^{3+}\text{-Mn}^{3+}$  en  $\text{Mn}^{4+}\text{-Mn}^{4+}$  niet lineaire, onafhankelijke ketens vormen als de ladingen van het mangaan eenmaal gelokaliseerd zijn. In tegenstelling tot het moeder materiaal  $\text{LiMn}_2\text{O}_4$  zijn de Jahn-Teller actieve  $\text{Mn}^{3+}$ -ionen in de low-spin staat. Bij 25K zien we dat de  $\text{Mn}^{4+}\text{-Mn}^{4+}$  spin fluctuaties invriezen. De  $\text{Mn}^{3+}\text{-Mn}^{3+}$  spin fluctuaties waren bij de laagste temperatuur (4K) nog steeds aanwezig.

Om de dynamica van de lithium ionen op een milliseconde schaal direct te bestuderen hebben we twee dimensionale magic-angle-spinning nuclear-magnetic-resonance experimenten uitgevoerd. Het op een milli seconde tijdschaal hoppen van lithium van een kristallografische site naar een andere, de 8a en 16c site, begint rond de 285K. Bij 380K begint het lithium zelfs te hoppen tussen meer dan 2 sites. De twee dimensionale NMR experimenten geven ons direct het lithium diffusie pad, de evenwichtsbezetting van de lithium plaatsen in het kristal, de activenergie en de lithium hop snelheid. De verkregen activenergie komt goed overeen met de in de literatuur vermelde macroscopische gemeten activenergie.

# Dankwoord

Aan het eind van dit proefschrift wil ik nog een aantal mensen bedanken die bijgedragen hebben tot de totstandkoming ervan.

Allereerst mijn dagelijkse begeleider en later ook promotor Ignatz de Schepper. Ignatz bedankt voor je vertrouwen, je enthousiaste begeleiding en de zeer prettige werksfeer. Mijn 2e promotor Joop Schoonman voor de nuttige discussies tijdens de werkbesprekingen en het kritisch lezen van artikelen en proefschriftteksten.

Bij de dagelijkse begeleiding was Fokko Mulder ook nauw betrokken. Fokko hartelijk dank voor de vele goede ideeën, het corrigeren van manuscripten en de prettige werksfeer.

Gijs Schimmel bedankt voor de mooie metingen die je als student voor mijn project hebt uitgevoerd en voor de vele aangename discussies over van alles en nog wat. Wouter Montfrooij bedankt voor het helpen van Gijs, het uitwerken van de QENS metingen en de hulp bij het uitvoeren van de diffractie metingen op POLARIS.

Erik Kelder en Michiel Jak bedankt voor de waardevolle discussies, het leveren van de samples en de hulp bij praktisch "chemisch" werk.

Veel van de experimenten beschreven in dit proefschrift zijn uitgevoerd buiten de TU Delft, waarbij ik veel hulp van de mensen van het betreffende instituut heb gekregen. Aad Bontenbal bedankt voor alle hulp bij de vele neutronen diffractie metingen. Gerda Nachtegaal, Arno Kentgens, Jan van Os en Hans Janssen van de afdeling "solid-state NMR" van de katholieke universiteit Nijmegen hartelijk bedankt voor jullie gastvrijheid en onmisbare hulp bij de toch wel gecompliceerde NMR metingen, die niet altijd even makkelijk gingen.

Al mijn collega's, in het bijzonder mijn (ex)kamergenoten Barry, Suzanne, Naveed, Octay en (ex)overburen Alexander, Ewout, Lambert, Rita, Mascha, Jeroen, Gijs, Marnix en Kuni bedankt voor de onmisbare fijne werksfeer.

Papa en mama, Ingeborg, Hans en Arend hartelijk bedankt voor de fantastische thuisbasis die jullie mij geven. En tot slot, Marjolein, bedankt voor alles wat je voor me betekent.



# Curriculum Vitae

I was born the 5<sup>th</sup> of March 1974 in Breda. From 1986-1992 I attended "Nassau Scholengemeenschap" (VWO) in Breda. After graduating from the VWO in 1992 I started to study applied physics at the Delft University of Technology. On May 27<sup>th</sup> 1997 I obtained the masters degree. The graduation project was: "Liquid sodium-thallium alloys" in the Department of neutronscattering and mössbauerspectroscopy. Subsequently, I started a Ph.D. project in July 1997 at the Interfaculty Reactor Institute of the Delft University of Technology. Here, I have investigated the structure and Li-dynamics of Li-doped  $BPO_4$  and  $LiMn_2O_4$ . This study is described in this thesis, and was supervised by prof. dr. I.M. de Schepper and prof. dr. J. Schoonman.





# List of publications

1. *Structure of liquid caesium-bismuth alloys studied by neutron diffraction*  
S.A. van der Aart, V.W.J. Verhoeven, P. Verkerk, W. van der Lugt, J. Chem. Phys. 112 (2000) 857
2. *Large clusters in liquid potassium-thallium alloys*  
S.A. van der Aart, P. Verkerk, L.A. de Graaf, W. van der Lugt, Y.S. Badyal, V.W.J. Verhoeven Physica B 234-236 (1997) 362
3. *Neutron and X-ray scattering on Li-doped BPO<sub>4</sub>*  
M.J.G. Jak, V.W.J. Verhoeven, I.M. de Schepper, F.M. Mulder, E.M. Kelder, J. Schoonman, Physica B 266 (1999) 108
4. *Influence of Mn by Li substitution on the Jahn-Teller distortion in LiMn<sub>2</sub>O<sub>4</sub>*  
V.W.J. Verhoeven, F.M. Mulder, I.M. de Schepper, Physica B 276 (2000) 950
5. *Li mobility in the battery cathode material Li<sub>x</sub>[Mn<sub>1.96</sub>Li<sub>0.04</sub>]<sub>4</sub> studied by muon-spin relaxation*  
C.T. Kaiser, V.W.J. Verhoeven, P.C.M. Gubbens, F.M. Mulder, I.M. de Schepper, A. Yaouanc, P. Dalmas de Réotier, S.P. Cotrell, E.M. Kelder, J. Schoonman, Phys. Rev. B 62 (2000) R9236
6. *Properties of Li-doped BPO<sub>4</sub> [Li-ion battery ceramic electrolyte]*  
M.J.G. Jak, Z.A. Kaszkur, J. Pielaszek, V.W.J. Verhoeven, J. Schoonman, Elec. Chem. Proc. 98-15 (1999) 692
7. *Neutron scattering investigation of the spin dynamics in Li[Mn<sub>1.94</sub>Li<sub>0.04</sub>]O<sub>3.94</sub>*  
H.G. Schimmel, W. Montfrooij, G.J. Kearley, V.W.J. Verhoeven, I.M. de Schepper, Phys. Rev. B, in press

8. *Lithium dynamics in  $\text{LiMn}_2\text{O}_4$  probed directly by two-dimensional  $^7\text{Li}$  NMR*  
V.W.J. Verhoeven, I.M. de Schepper, G. Nachtegaal, A.P.M. Kentgens, E.M. Kelder, J. Schoonman, F.M. Mulder, Phys. Rev. Lett., 86-19 (2001) 4314
9. *Magnetic signature of charge ordering in  $\text{Li}[\text{Mn}_{1.94}\text{Li}_{0.04}]\text{O}_{3.94}$  and  $\text{Li}_{0.2}[\text{Mn}_{1.94}\text{Li}_{0.04}]\text{O}_{3.94}$*   
V.W.J. Verhoeven, I.M. de Schepper, F.M. Mulder, accepted for publication in App. Phys. A
10. *Frequency shifts in deep inelastic scattering*  
H.G. Schimmel, W. Montfrooij, V.W.J. Verhoeven, I.M. de Schepper, submitted to Euro Phys. Let.